**Influence of Blade Gap Thickness and Recoater Velocity on Powder Layer Quality in Additive Manufacturing**

by

Kristin Elizabeth Fucito

A thesis submitted to the Graduate Faculty of
Auburn University
in partial fulfillment of the
requirements for the Degree of
Master of Science

Auburn, Alabama
May 2, 2020

Key Words: Additive Manufacturing, Powder Bed Fusion, Recoating Process, Surface
Roughness, Packing Density

Approved by

Barton C. Prorok, Professor of Materials Engineering
Richard Williams, Senior Lecturer of Mechanical Engineering
Xiaoyuan Lou, Associate Professor Mechanical Engineering

Abstract

The mechanical properties of components produced by additive manufacturing processes are the result of the powder layer quality. In powder bed fusion, a more uniform powder layer is necessary for the laser to penetrate the material evenly, building a mechanically stronger part that contains less defects. Research has shown that the powder bed parameters directly influence the powder layer quality. Ideal powder layer quality is defined as having maximum packing density and minimum surface roughness. This study focuses on how the recoating system process impacts the layer quality by varying recoater velocity and blade gap thickness. Inconel 625 powder, with an average particle size of 31.3313μm, is used to study the powder bed parameters. Generally, surface roughness decreased with increasing blade gap thickness, and increased with increasing recoater velocity. Additionally, packing density increased with increasing layer thickness, and decreased with increasing recoater velocity. Linear regression analyses were used to identify exactly what input parameters produce the best layer quality. In conclusion, the most optimum powder layers occur at $V_r = 10$mm/s and $t_{bg} = 256$μm.

Table of Contents

# List of Tables

List of Figures

**Introduction**

Additive manufacturing is the method of joining materials layer-by-layer to produce parts from a three-dimensional, solid model. Compared to conventional subtractive manufacturing processes (i.e. CNC machining, laser cutting, etc.), additive manufacturing allows for more design freedom. This method produces a wide variety of complex, near-net geometries, encouraging more efficient designs and reducing material waste [1]. Additive manufacturing encompasses a collection of processes that are primarily differentiated based on material and energy source. Additive manufacturing processes that use metal powders, such as powder bed fusion, are becoming more popular due to the quality of the components they produce.

**Powder Bed Fusion**

In the powder bed fusion process, sequential layers of metal powder are deposited onto a build surface. The layers are exposed to a high-power laser beam that melts and fuses the powder together. This process takes place in an enclosure with a controlled atmosphere typically filled with argon or nitrogen to prevent undesirable impacts on the microstructure [2].

The powder bed fusion process includes the laser, the supply plate, the build plate, the overflow chamber, and the recoater (Figure 1). When the process begins, the supply plate travels a predetermined vertical distance up, exposing the supply powder beyond the surface of the machine. This vertical distance is selected to ensure that the new powder layer completely covers the previous layer. The recoater then moves across the supply plate, collecting the exposed powder to spread evenly across the build plate. The excess powder is carried into the overflow chamber. Once the recoater clears the build plate, a laser beam selectively melts the powder layer. The laser beam path is predetermined from a 3D CAD file rendering that slices the component into layers.

After exposure, the build plate and the supply plate both move down, avoiding the recoater as it returns to its initial position. These steps are repeated until the final layer of the part is completed. Once the process is finished, the build plate is removed, and the part is separated.
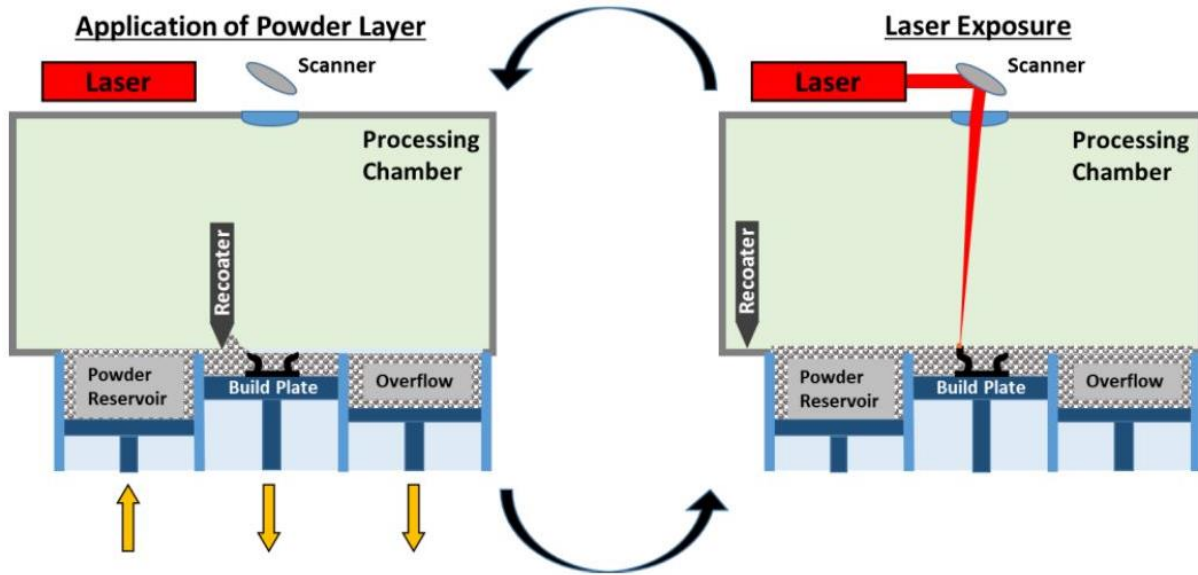


**Figure 1**. Schematic of the powder bed fusion process [2].

Research has shown that the powder bed parameters directly influence the mechanical properties of additively manufactured parts. Powder layer inhomogeneity affects the melt pool behavior and the shape of the solidifying material. A uniform powder layer is necessary for the laser to penetrate the material consistently. Ideal layer quality is defined as having maximum packing density and minimum surface roughness. This study will focus on how the powder bed fusion recoating process impacts the layer quality by varying blade gap thickness and recoater velocity.

**Powder Characterization**

Powder particles are characterized by morphology and size distribution, which affect the overall powder behavior during the recoating process. It is important to understand the relationship

between the powder characteristics and the recoating process parameters in order to select the most appropriate powder.

**Powder Morphology**

Morphology describes the size, shape, and roughness of particles. Spherical particles are often desired in powder bed fusion because their shape correlates to higher packing density (Figure 2) [3, 4].
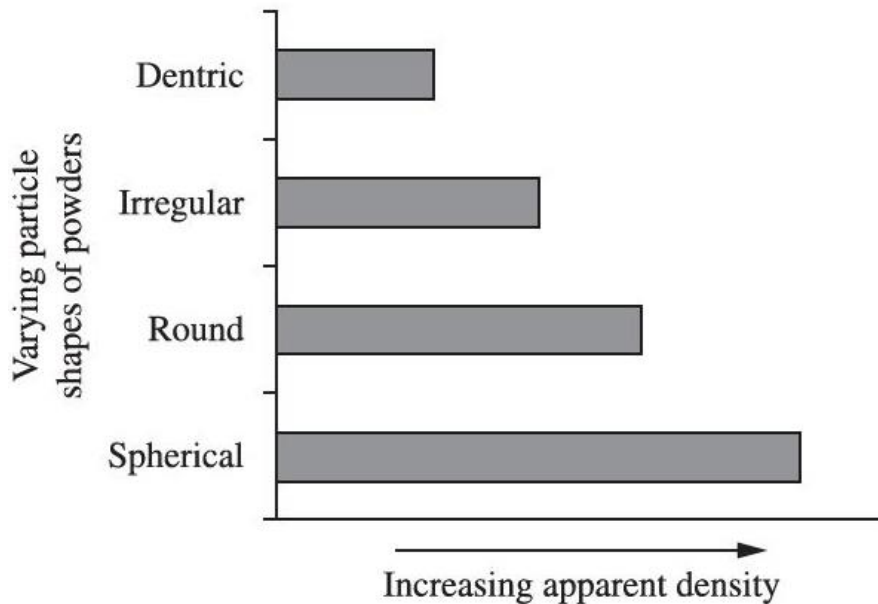


**Figure 2**. Effect of particle shape on apparent density [5].

Smooth particles have higher flowability because interparticular friction and mechanical interlocking both increase as the particle shape becomes more irregular [6]. Irregular shapes generally have a higher surface roughness, and they are more sensitive to layer thickness, which decreases layer quality (Figure 3) [4].
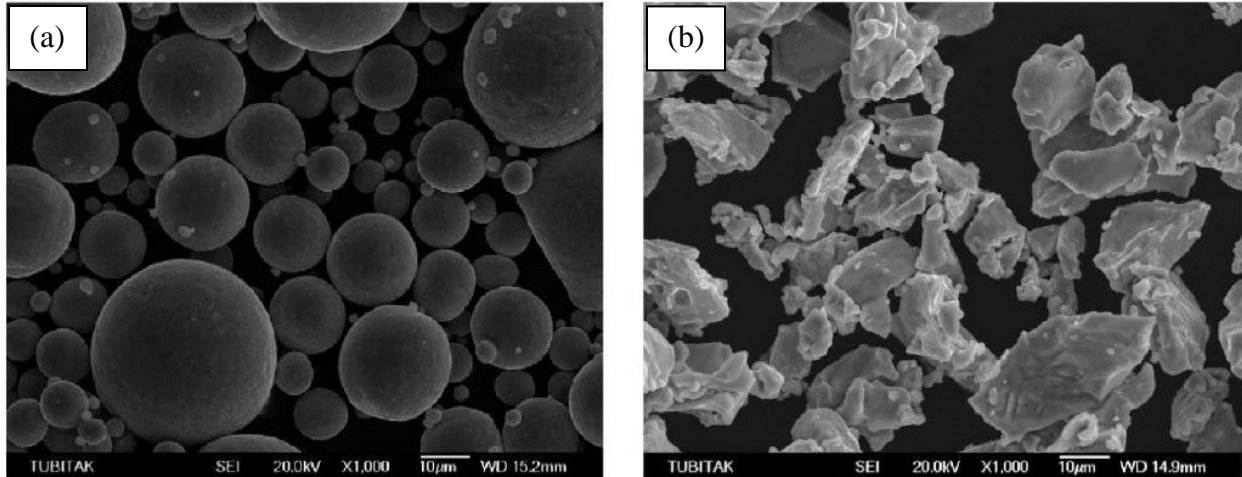
**Figure 3**. SEM images of Ti64 powder morphology (a) spherical and (b) irregular in shape [7].

**Powder Production**

Powder manufacturing methods largely determine the individual particle properties. Higher quality powder is often defined as having a more consistent particle morphology (i.e. fewer irregular particles). Plasma atomization is a process that produces highly spherical particles. Feedstock is fed into the atomization chamber where plasma torches and gas jets simultaneously melt and break it apart into small droplets (Figure 4) [8]. The surface energy of the liquid pulls the molten droplet into spheres as it falls, solidifying the particles before they reach the bottom of the atomization chamber [9]. This process minimizes potential impurities since the material does not come into any contact with other surfaces during the solidification process [8].
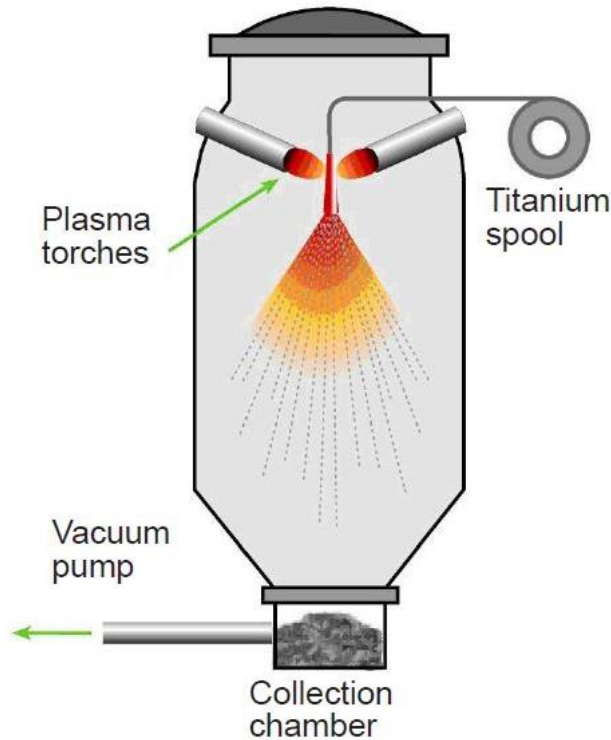
**Figure 4.** Schematic of the plasma atomization process [8].

**Particle Size Distribution**

The particle size distribution is a representation that indicates the size and proportions of particles that are present in a powder. Generally, larger size distributions lead to higher packing densities. However, it is important to note that they are more difficult to spread due to the introduction of cohesive forces between the smaller particles [9, 3, 10]. In DEM simulations that compared different size distributions, it was found that with decreasing particle size and increasing recoater velocity, the number of particle voids increase, leading to higher surface roughness (Figure 5) [11]. Therefore, the ideal grain size distribution for powders is narrow with an emphasis on larger particles.
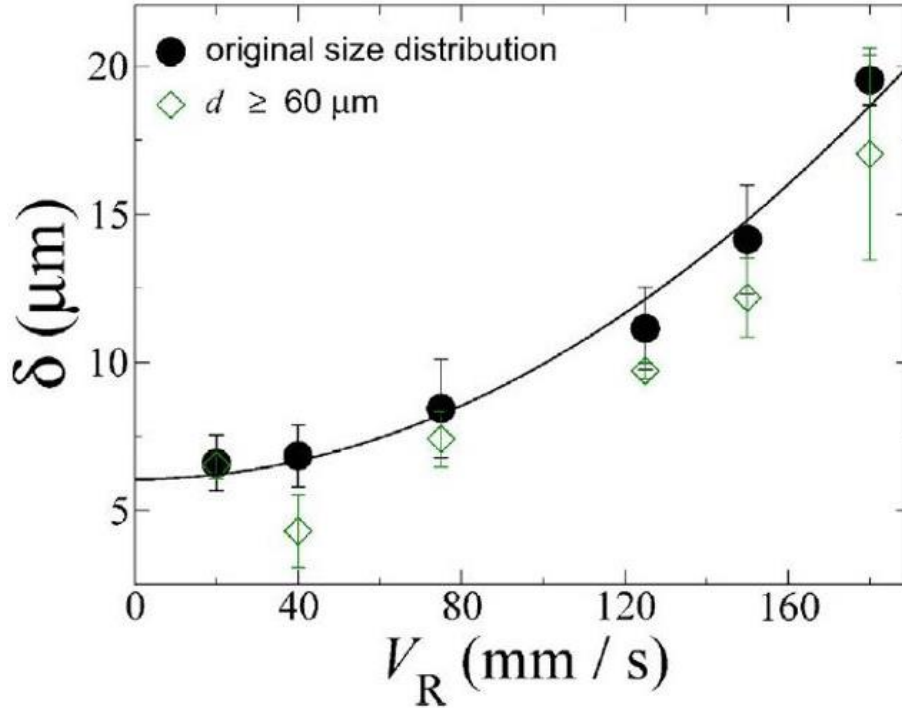
**Figure 5.** Comparison of the original and modified size distribution [11].

**Interparticle Forces and Flowability**

Cohesion is the tendency of particles to stick together due to interparticle forces. Cohesive forces (i.e. capillary, electrostatic, van der Waal) between particles become increasingly important as particle size decreases [12]. Powders with particle sizes below a range of 100μm are considered to be cohesive [9].

Capillary forces are introduced as the granular material becomes saturated. Saturation occurs in a natural environment due to humidity present in the ambient air. Only in a vacuum can capillary forces be avoided. In the presence of humidity, a film surrounds individual particles. A liquid bridge forms across two particles as they get closer together. The surface tension from the liquid introduces an attractive force between the two particles [9].

There are four degrees of saturation depending on the amount of liquid present (Figure 6). The forces between the particles in the pendular formation are larger compared to the other three formations. As the humidity in the system increases, the formation changes from pendular to droplet [12].



(a)   (b)

(c)   (d)
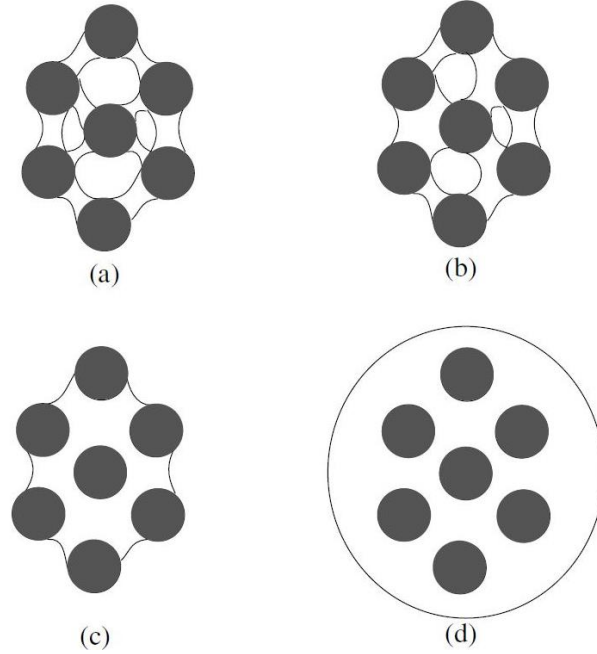
**Figure 6.** Degrees of liquid saturation: (a) pendular, (b) funicular, (c) capillary, (d) droplet [12].

The totally capillary force is represented by a pendular schematic (Figure 7) in the following equation:

$$F_c = 2\pi R\gamma sin^2\beta \left[1 + \frac{R\Delta P}{2\gamma}\right],$$   (1)

where $R$ is the particle radius, $\gamma$ is the fluid's surface tension, $\beta$ is the half-filling angle, and $\Delta P$ is the pressure difference [12].
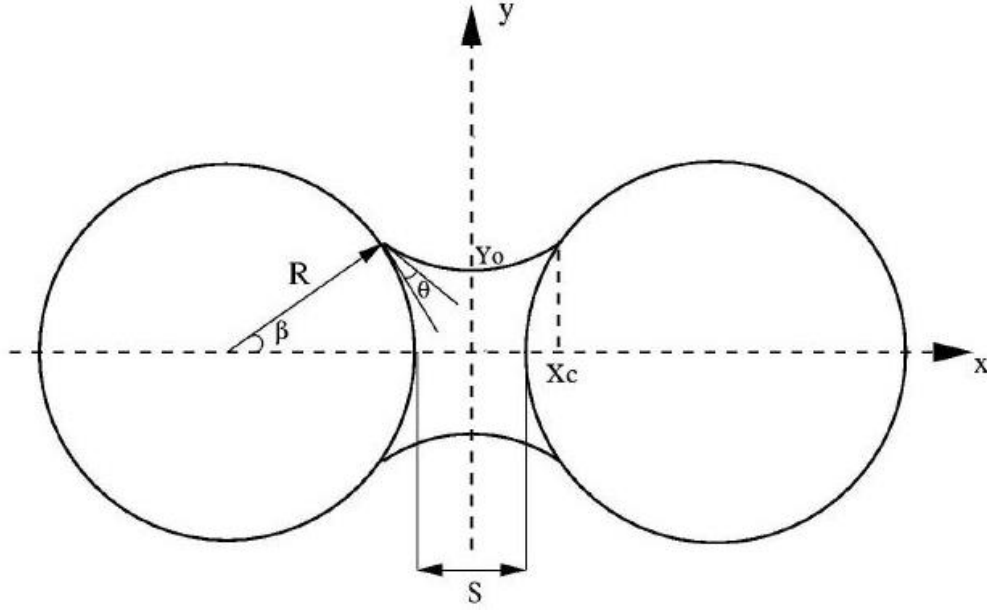
**Figure 7**. Schematic of a symmetric liquid bridge [12].

Electrostatical forces (i.e. Coulomb force, image force, electrostatical potential difference) are introduced through friction when there is a difference in charge potential between particles [9, 12]. Electrostatic force is represented by the following equation:

$$F_e = \frac{q_1 q_2}{4\pi\varepsilon_0 r^2} ,$$

(2)

where $q_1$ and $q_2$ are the charge of each particle, $r$ is the distance between particles, and $\varepsilon_0$ is the relative permittivity of the medium [9].

van der Waal forces are introduced through particle dipoles, and they are a function of the interparticle spacing (Figure 8) [12]. More attraction occurs as the spacing increases. More repulsion occurs as the spacing decreases. The difference in the potential is represented by the equation below:

$$w(r) = -\frac{c}{r^6} ,$$

(3)

where $c$ is the interaction constant, and $r$ is the distance between particles [9, 12]. The Hamaker theory assumes the interaction energy between an isolated particle and the particles of a large body

is additive. The net interaction energy is represented by the particle interaction integrated over the entire particle body. This results in a force relationship represented in the equation below that covers distances that are larger compared to when the distance between two particles is considered:

$$F(s) = \frac{AR}{12s^2},$$  (4)

where $A$ is the Hamaker constant, $R$ is the radius of the sphere, and $s$ is the distance between the sphere and the surface [12].
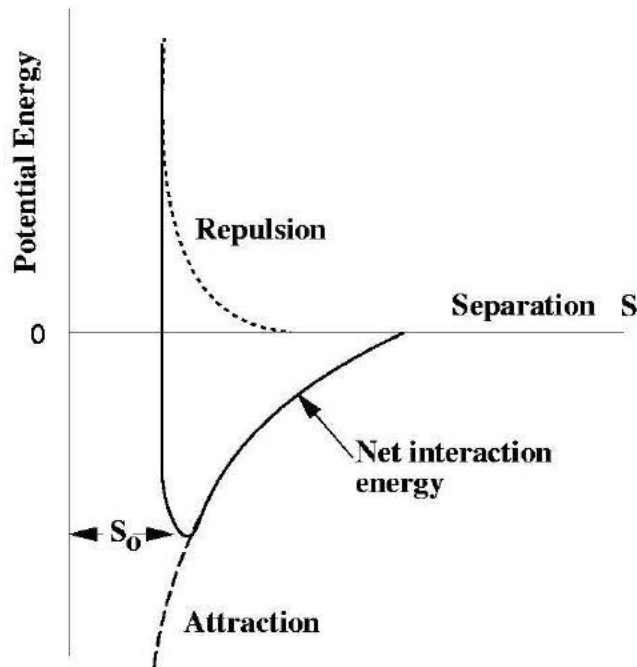


**Figure 8.** Potential energy diagram [12].

Lower flowability is not desired as it may lead to irregular packing density. Flowability reduces significantly with decreasing particle size due to the introduction of cohesive forces [13]. In experiments comparing different particle sizes, larger particles (200μm) are found to have higher flowability than smaller particles (63μm) [3]. The amount of surface oxide present on the particle's surface also influences flowability. Increasing the amount of surface oxide present decreases flowability for irregular shaped particles [14].

**Packing Density**

Packing density (or packing fraction as it is referred to in some cases) is defined as the ratio between the mass and the empty space occupied in a given volume. The packing density of mono-sized spheres (i.e. face-centered cubic or hexagonal) is 74%. This can be increased by adding secondary, smaller spheres to fill in the voids (Figure 9). In a bimodal distribution, the packing density increases to 93% if the secondary spheres are assumed to have regular close packing between the primary spheres [15].
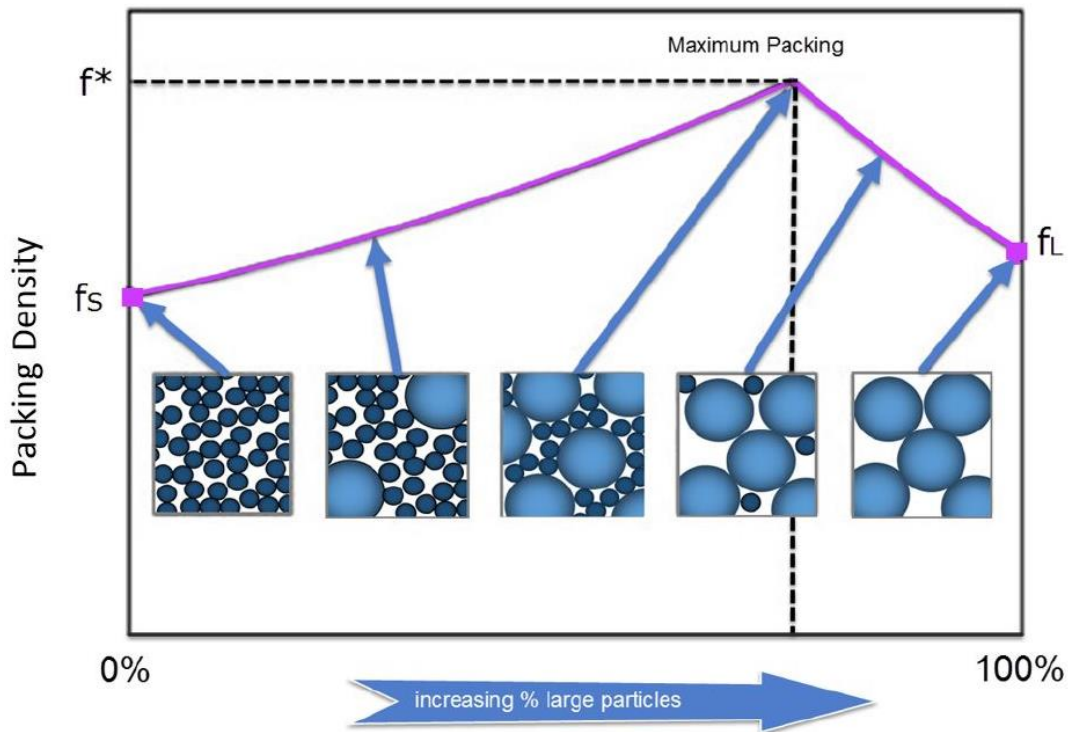


**Figure 9**. Packing density reaches a maximum when including both fine and coarse particles [6].

Generally, the packing density of a powder bed is between 30%-60%, which depends on powder morphology, powder size distribution, and the powder bed parameters. Higher packing densities lead to more uniform powder beds. As blade gap thickness and recoater velocity increase, layer packing density increases and decreases, respectively [1, 16]. In DEM simulations that considered powder with a Gaussian distribution and a blade gap thickness of 350μm, the packing density equaled 58.44% [16]. Cohesive powders also affect the packing density and typically correlate to lower values (Figure 10). When considering maximum cohesive powder, the packing density resulted in 54%. Non-cohesive powder resulted in a packing density of 62% [15].



(a) Intermediate configuration: $\gamma=0$.      (b) Intermediate configuration: $\gamma=\gamma_0$.

(c) Final configuration: $\gamma=0$.      (d) Final configuration: $\gamma=\gamma_0$.
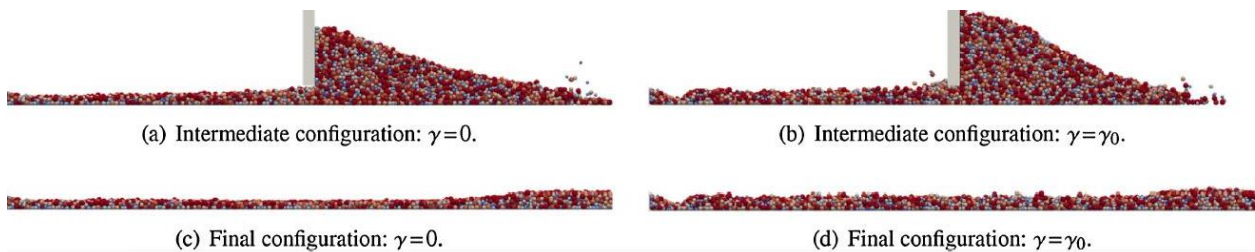
**Figure 10.** Recoating configurations for no cohesion (a) (c), and equivalent cohesion (b) (d) [15].

**Surface Roughness**

Surface roughness is defined as the variation of particle height in the powder bed [9]. Surface roughness and packing density are the two defining factors of a quality powder bed. These two properties are independent of each other (Figure 11) [15].



(a) Low SR, High PF.      (b) Low SR, Low PF.      (c) High SR, High PF.      (d) High SR, Low PF.
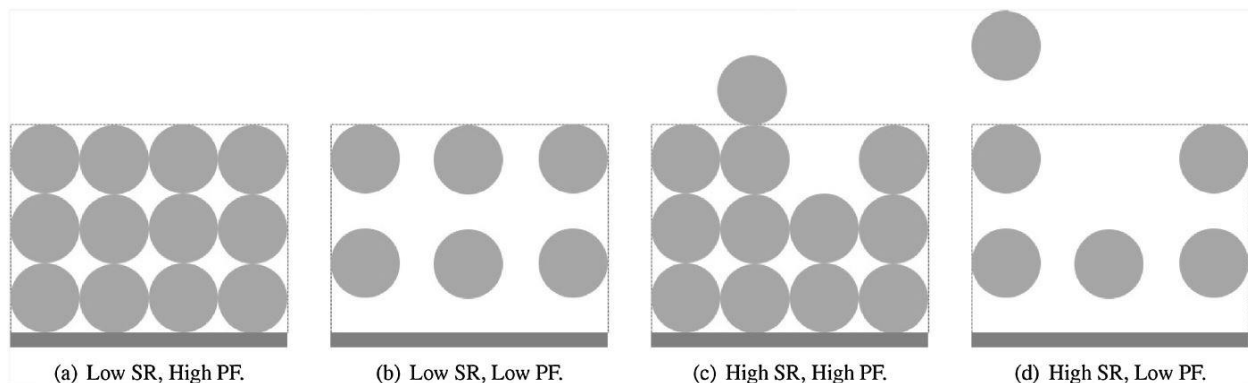
**Figure 11.** Powder particle configurations varying surface roughness and packing fraction [15].

Lower surface roughness improves the mechanical and structural properties of printed parts. The variation in layer thickness can build up over time, leading to areas that are too thick for laser penetration [17]. Generally, surface roughness decreases with decreasing layer thickness. Surface roughness is commonly caused by the formation of powder agglomerates in finer powders. Agglomerates form when surface forces and cohesive forces are larger than the gravitational force [9, 18]. However, increasing blade gap and decreasing recoater velocity can help avoid the impact of agglomerates. Narrower size distributions have also been found to help decrease surface roughness because the number of particle voids decrease when spreading [11].

**Powder Bed Parameters**

It is important to optimize the powder bed parameters for the powder that has been selected. Powder particles behave differently depending on the recoater geometry, recoater velocity, and the blade gap thickness. Some options are more cost-saving and time efficient, but not without compromising the quality of the finished part. Understanding how the powder bed parameters control powder behavior during the recoating process is essential.

**Recoater Geometry**

The most common recoaters are rollers and blades, with blades coming in a variety of different shapes. When comparing flat, round, and sharp blade geometries, it is found that the flat blade geometry produces the lowest surface roughness (Figure 12). This is because the horizontal contact zone between the blade and the powder bed is larger than the other two geometries. A more consistent compression is produced, and therefore, a more uniform and dense powder bed [3]. The sharp blade geometry is more susceptible to particle dragging because the blade only interacts with the powder at one point, which increases surface roughness [19].

12
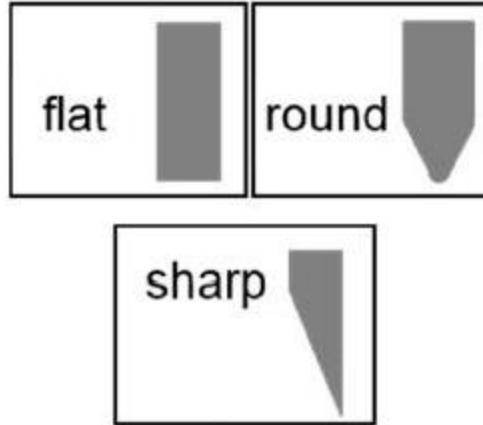
**Figure 12.** Different blade geometries [3].

A roller significantly outperforms a blade because its geometry allows for gradual particle rearrangement, and because a roller has a larger contact area with the powder [20]. Particle volume fraction decreases, and surface roughness increases in the case in which a blade is used (Figure 13) [20]. This results in a decrease in powder bed quality.



(a) Volume Fraction

(b) Bed Roughness
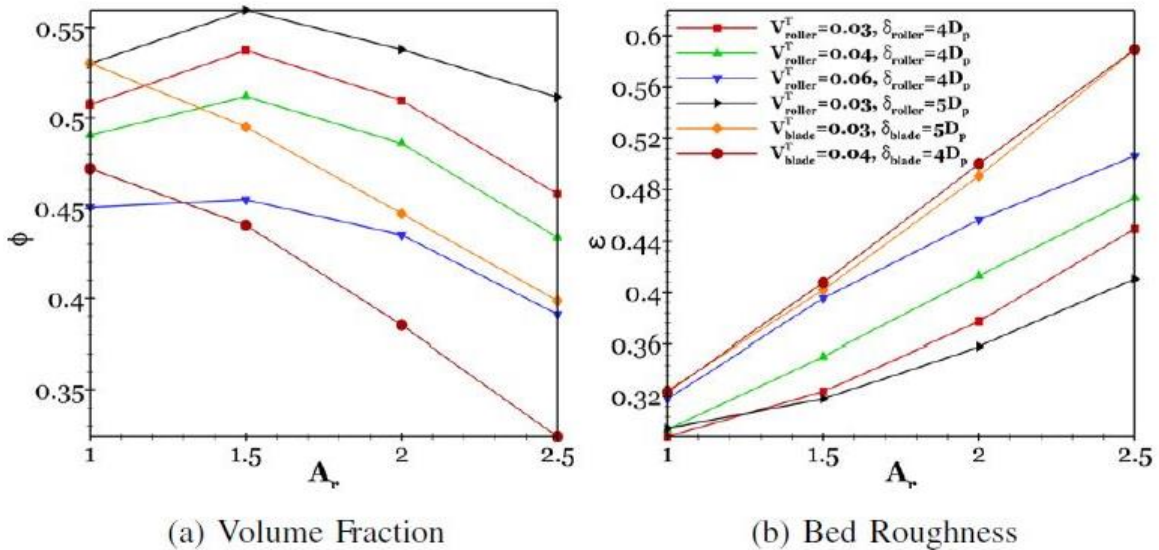
**Figure 13.** The effects of particle shape and the spreader type on the bed quality [20].

In a 48 DEM simulation study, blade shape ($n_s$), width ($a_s$), and height ($b_s$) were varied to identify an optimum blade shape that produces layers with maximum volume fraction. Generally, blade profiles with smaller heights and larger widths generated higher volume fractions. The optimum

blade profile was identified with values of $n_s=5$, $a_s=100D_{sph}$, and $b_s=10D_{sph}$, where $D_{sph}$ is the sphere diameter for rods [21] (Figure 14).
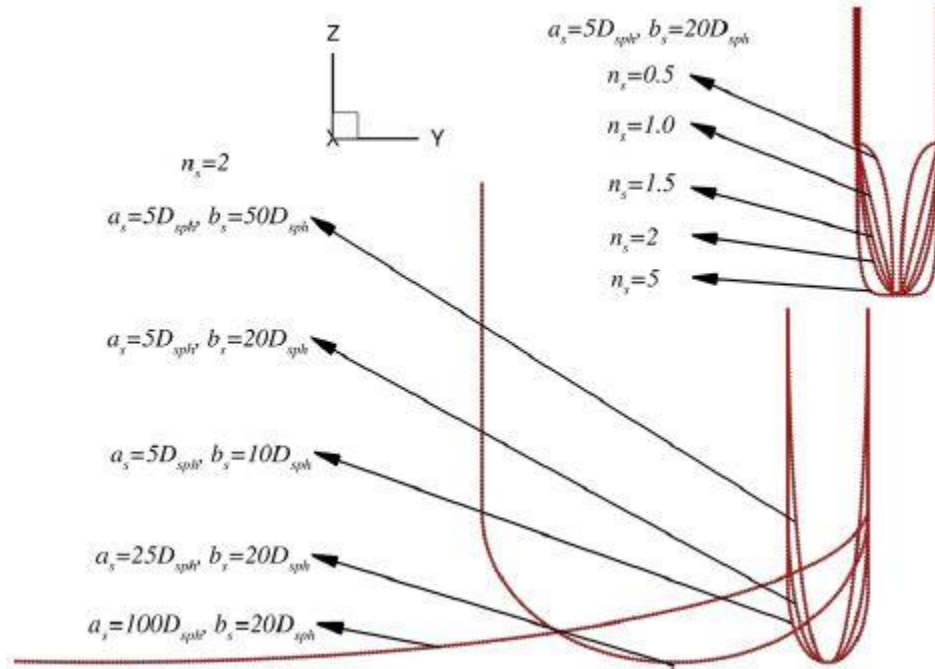


**Figure 14.** Different spreader profiles used for the optimization [21].

At varying velocities, the optimum blade produced lower surface roughnesses than the roller. The optimum blade also produced similar, but lower, volume fractions than the roller (Figure 15). The optimum blade is much less sensitive to increasing velocity than the roller, which is significant. The volume fraction is slightly greater at higher velocities, meaning the impact of quality is limited.
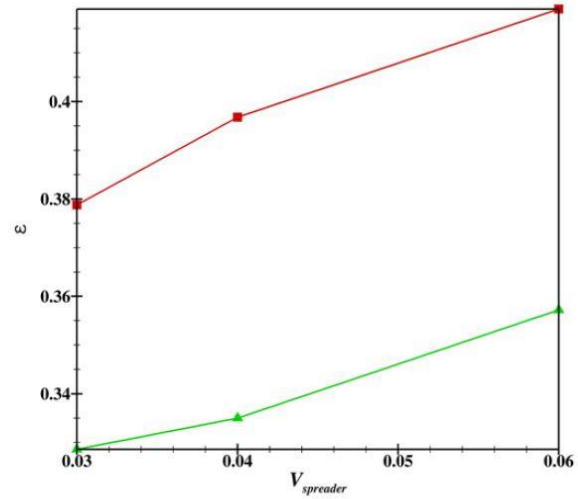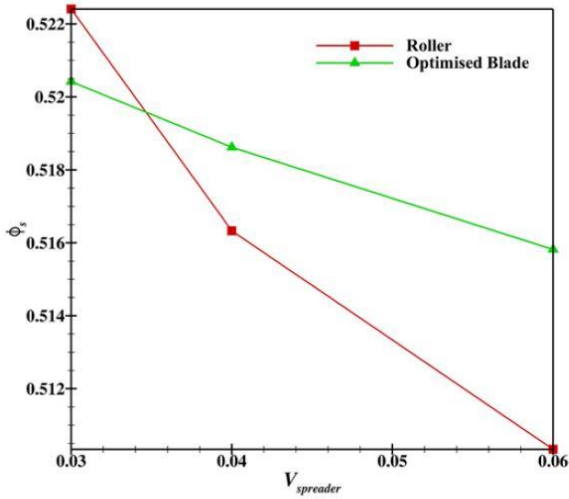
(a) Volume Fraction        (b) Surface Roughness

**Figure 15**. Comparison between a roller and the optimized blade type spreader [21].

**Recoater Velocity**

The recoater velocity translates to the productivity of the machine. It is desirable to increase recoater velocity in order to produce parts at a faster rate. However, packing density decreases and surface roughness increases at higher velocities. This is because it becomes more difficult for the particles to fill in the voids that appear, decreasing the powder bed quality (Figure 16) [11].
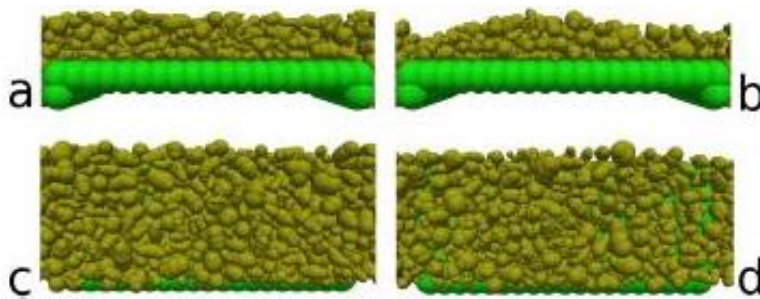


**Figure 16**. Side (a)(b) and top views (c)(d) of powder layer spread at 20mm/s (c) and 180 mm/s (d) [11].

However, with more adhesive powders, layer quality is less impacted at higher velocities (100mm/s and above). In DEM simulations that studied the effects of increasing friction at high velocities, the flowability of the powder reduced, which slightly increased the layer thickness

(Figure 17). Nonetheless, the powder layer quality will still decrease with increasing adhesion at high velocities [15].



(a) Mean value of packing fraction field $\Phi_t(x,y)$.

(b) Mean value of surface profile field $z_{int}(x,y)$.

(c) Standard deviation of packing fraction field $\Phi_t(x,y)$.

(d) Standard deviation of surface profile field $z_{int}(x,y)$.
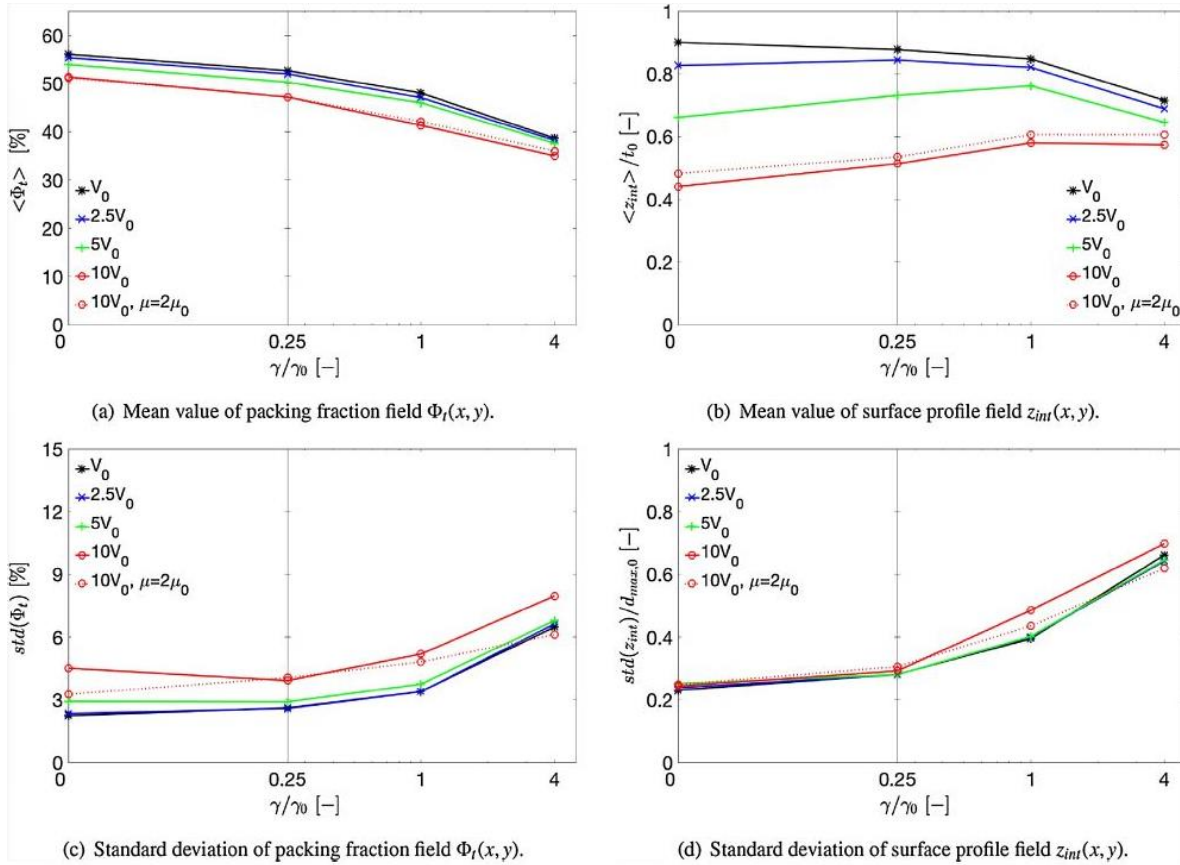
**Figure 17.** Surface roughness and mean layer height at different blade velocities [15].

**Layer Thickness**

Layer thickness is defined as the minimum distance the heat source must travel through the powder to reach the previous layer [17]. Layer thickness is selected based on the particle size distribution of the powder. Typically, thinner layers are desired since deformities have less of an impact on surface roughness, and they may average out over the course of the build [9]. However, thinner layers are equivalent to longer builds, which decreases the powder bed productivity. Layers that are equal to or smaller than the maximum particle size lead to discontinuities in the powder (Figure 18) [15].

(a) $t_0 = d_{max,0}$, $\gamma = 0$.

(b) $t_0 = d_{max,0}$, $\gamma = \gamma_0/4$.

(c) $t_0 = d_{max,0}$, $\gamma = \gamma_0$.

(d) $t_0 = d_{max,0}$, $\gamma = 4\gamma_0$.

(e) $t_0 = 2d_{max,0}$, $\gamma = 0$.

(f) $t_0 = 2d_{max,0}$, $\gamma = \gamma_0/4$.

(g) $t_0 = 2d_{max,0}$, $\gamma = \gamma_0$.

(h) $t_0 = 2d_{max,0}$, $\gamma = 4\gamma_0$.

(i) $t_0 = 3d_{max,0}$, $\gamma = 0$.

(j) $t_0 = 3d_{max,0}$, $\gamma = \gamma_0/4$.

(k) $t_0 = 3d_{max,0}$, $\gamma = \gamma_0$.

(l) $t_0 = 3d_{max,0}$, $\gamma = 4\gamma_0$.

(m) $t_0 = 4d_{max,0}$, $\gamma = 0$.

(n) $t_0 = 4d_{max,0}$, $\gamma = \gamma_0/4$.

(o) $t_0 = 4d_{max,0}$, $\gamma = \gamma_0$.

(p) $t_0 = 4d_{max,0}$, $\gamma = 4\gamma_0$.
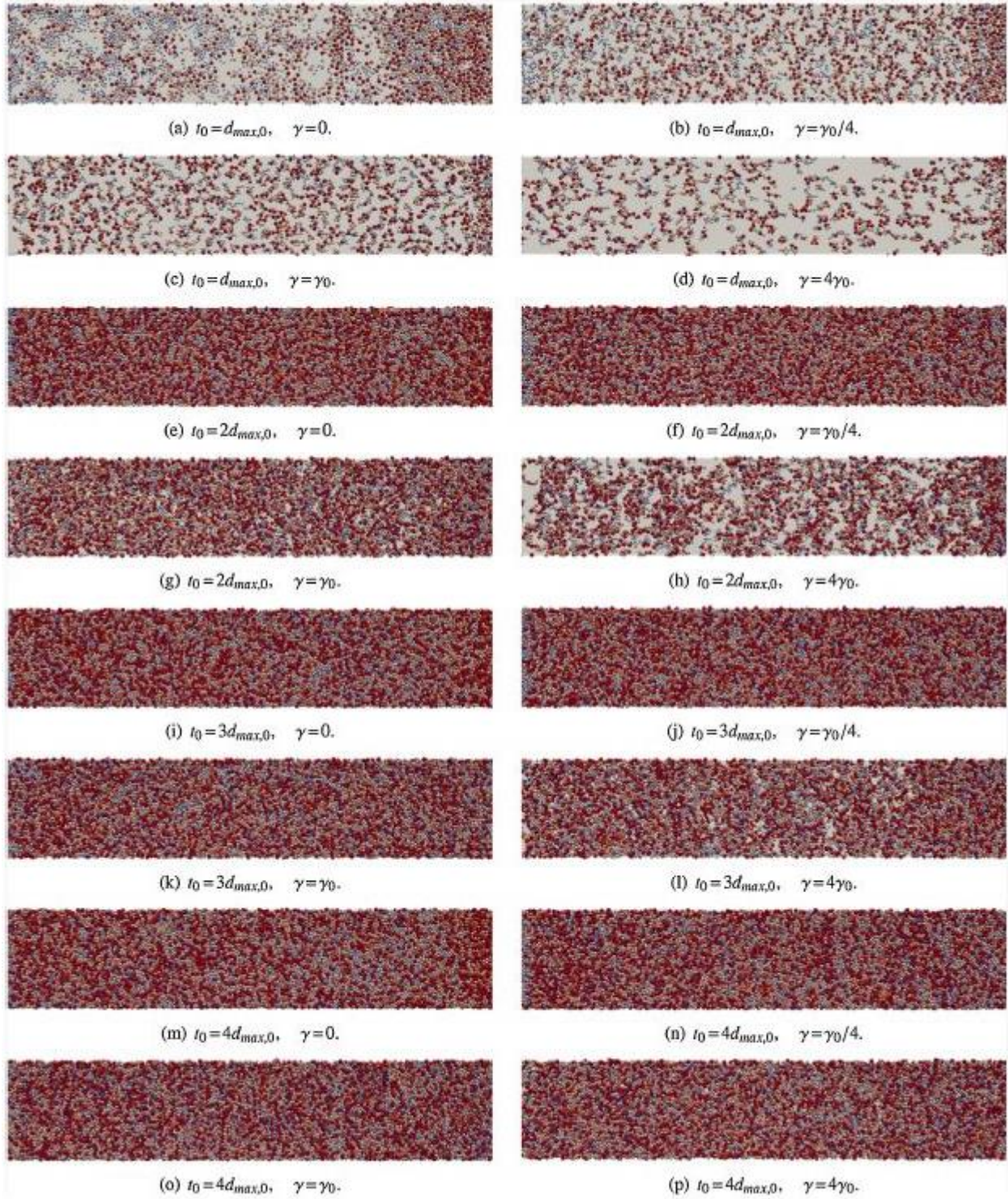
**Figure 18.** Top view of powder layers for different layer thicknesses and surface energies [15].

With more cohesive powders, smaller blade gaps lead to less dense and more irregular powder layers (Figure 19). Particle agglomerates within cohesive powders are subject to stronger resistance forces when passing underneath the recoater [15]. At larger layer thicknesses, the particles have more room to arrange into a denser pattern, and agglomerates are able to fit underneath the recoater. Optimum powder layer quality is usually reached at two to three times the maximum particle diameter for cohesive powders, and three to four times the maximum particle diameter for non-cohesive powders [15].



(a) Mean value of packing fraction field $\Phi_t(x, y)$.

(b) Mean value of surface profile field $z_{int}(x, y)$.
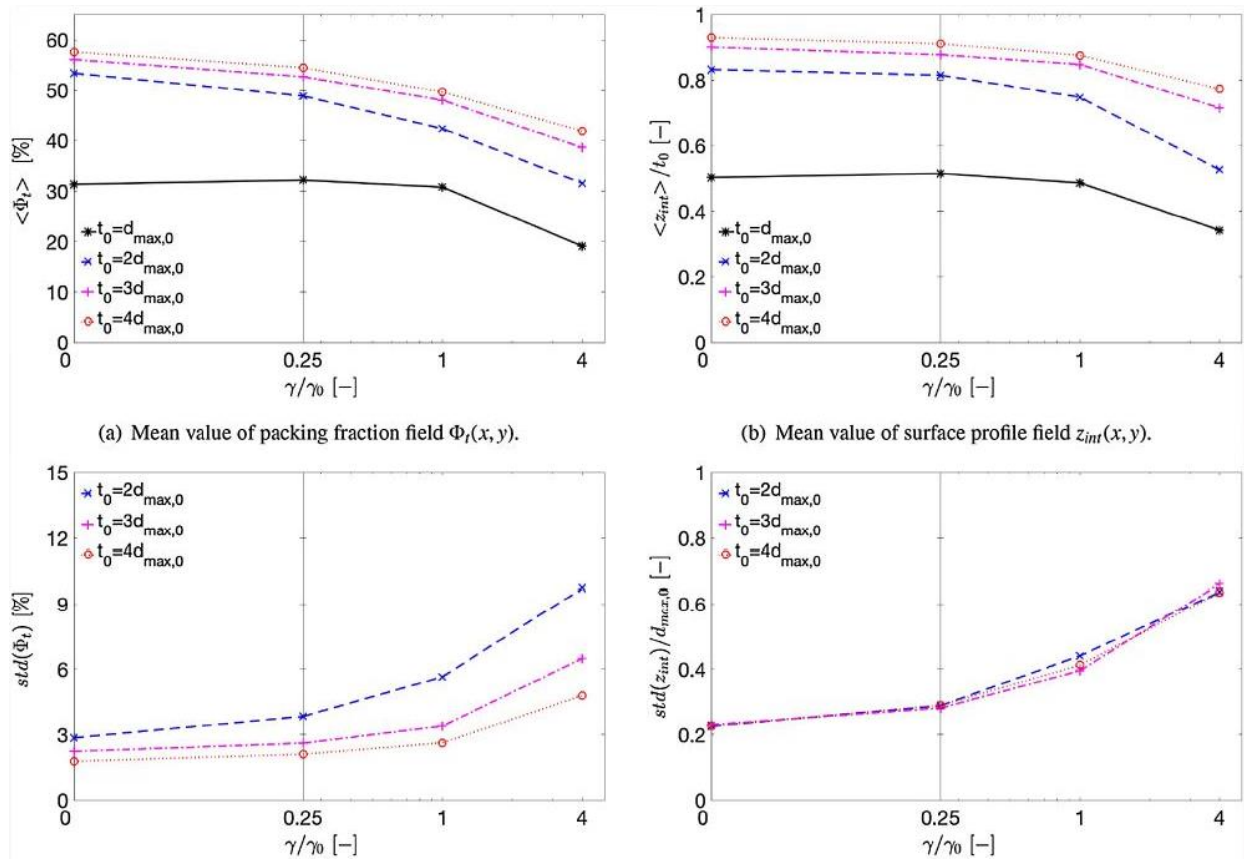
Fig. 19. Surface roughness and mean layer height at different layer thicknesses [15].

**Materials and Methods**

The materials and methods used in this study help quantify the quality of the powder layers over the build plate. The blade gap and recoater velocity are varied to study how these input parameters impact the surface roughness and packing density of the powder layers.

**Powder Bed Machine**

The powder bed machine built by Auburn University's Department of Mechanical Engineering is used to study the recoating process (Figure 20). The recoating system is enclosed within the powder bed machine and controlled using an Arduino Graphical User Interface (GUI) system.
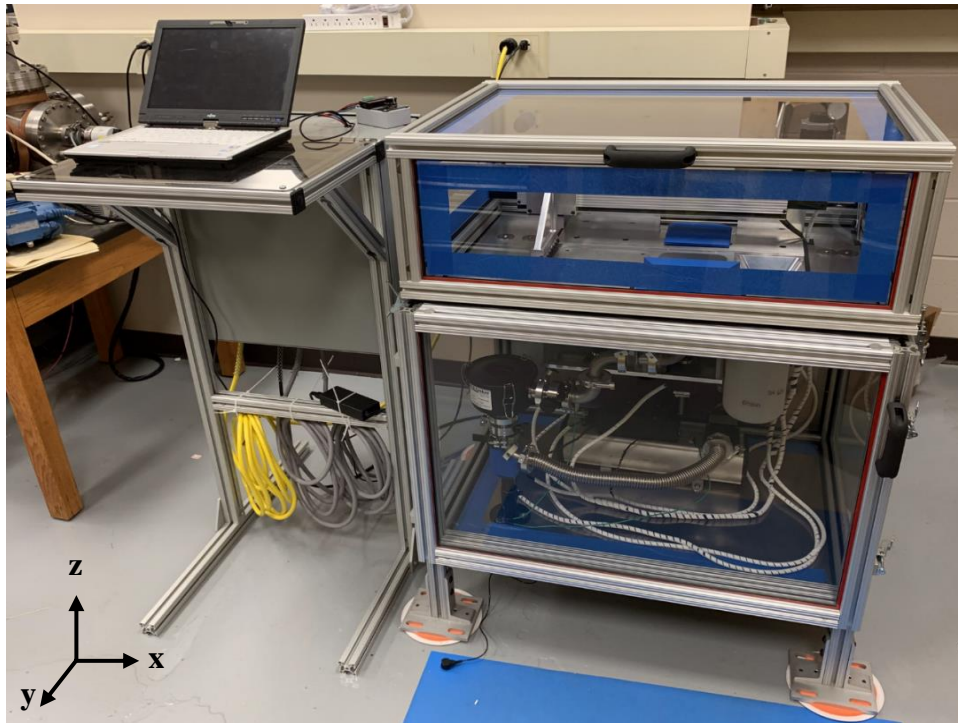


**Figure 20**. Powder bed machine.

**Recoating Process**

The recoating process is similar to many conventional additive manufacturing machines. The supply plate (a) moves up, which exposes powder in the supply beyond the surface of the machine. Moving from left to right, the recoater (d) collects the exposed powder from the supply, and deposits it across the build plate (b) in a thin layer. Excess powder is carried into the overflow bin (c). The recoater locates home, a predetermined location to the right of the build plate set by the GUI, and waits while the supply plate and build plate both move downward. The recoater moves from right to left to return to its initial start position, and the process repeats (Figure 21).
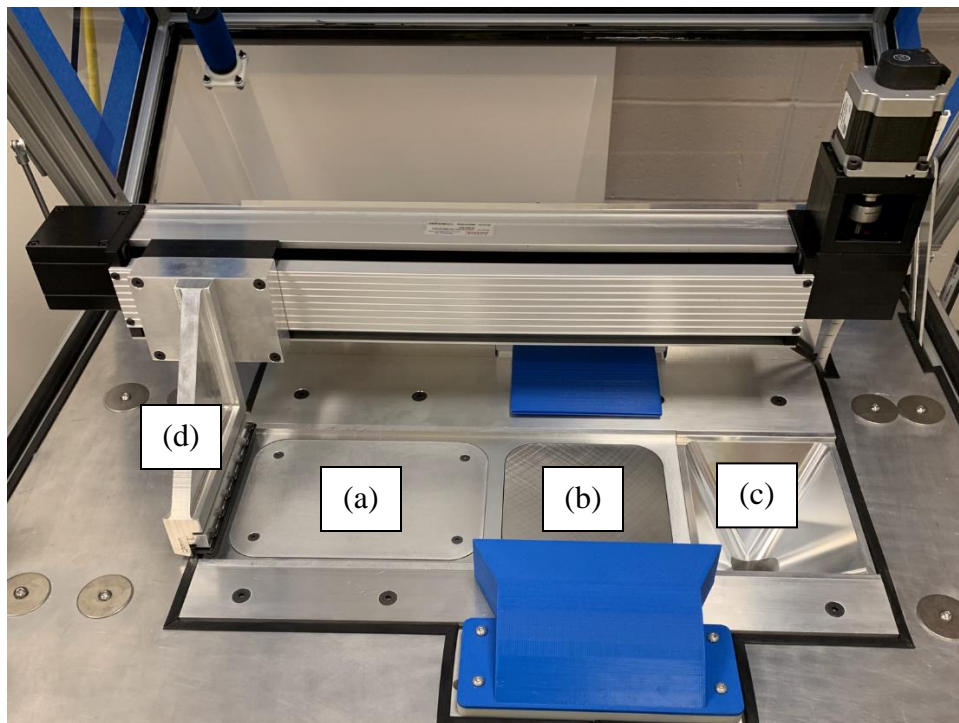


**Figure 21**. Recoating system.

Ball screw linear stepper motors are used to move the supply plate and the build plate in a vertical plane of motion. This vertical displacement correlates to the supply and build travel program inputs.

A motorized belt driven linear actuator is used to move the recoater.  Attached to the stage mount is a cantilever that houses the blade adapter.  The blade adapter is designed to allow rubber blades to be removable and changed frequently.

Geometrically sharp rubber blades provided by EOS are used in this study (Figure 22).  A blade is easier to switch out and easier to implement compared to a roller.  A rubber material was chosen to allow for more error.  Should any incident occur, there would be less impact on the powder bed using a flexible rubber blade, rather than a rigid one.
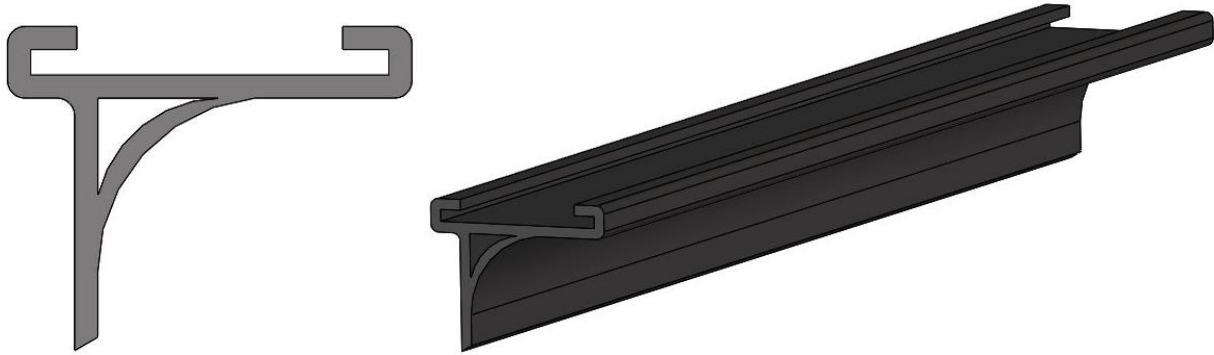


**Figure 22.** CAD design of blade geometry.

**GUI Interface**

The default program inputs serve as a baseline for how the machine operates (Table 1).

**Table 1**. Default GUI program inputs.

| | |
|---|---|
| Repetitions: | 1 |
| Recoat park position (cm): | 37 |
| Supply up travel (μm): | 240 |
| Supply down travel (μm): | 200 |
| Build down travel (μm): | 40 |
| Build speed (μm/s) | 50 |
| Supply speed (μm/s) | 50 |
| Recoat speed (cm/s) | 5 |
| Delay source: | Time |
| Delay between move(s): | 0.2 |

The supply down travel default input is set at 200μm to account for backlash. Further study of this recoating process is needed to minimize the displacement. The build speed and the supply speed are velocities at which the respective plates travel. These speeds are both set at 50μm/s to prevent any additional vibration from potentially affecting powder settling behavior.

**Inconel 625 Characterization**

The means of having concentrated gas (i.e. nitrogen, argon) flowing throughout the powder bed machine is not necessary for this study because no laser interactions occur. For this reason, Inconel 625 is chosen primarily because of its protection against oxidation. Concept Laser provided 5kg of highly spherical, plasma atomized powder in the largest particle size offered. A large particle size is needed to ensure the surface roughness of the powder layers can be determined optically. A JEOL JSM-7000F SEM equipped with Energy Dispersive X-Ray Spectroscopy (EDS) is used to analyze the morphology of the powder. The powder particles are confirmed to be primarily spherical with smooth surfaces (Figure 23).
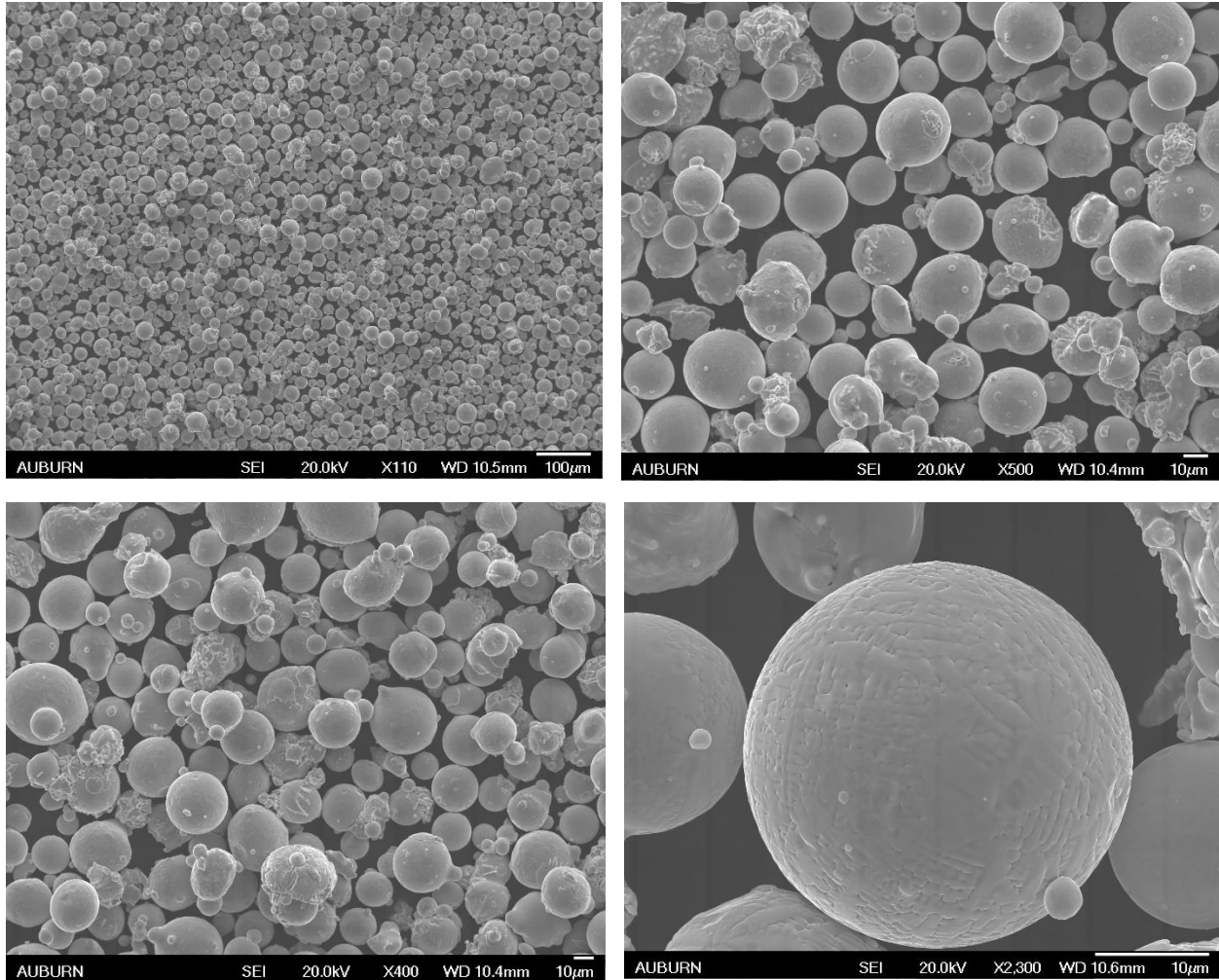
**Figure 23.** SEM images of plasma atomized Inconel 625 powder morphology.

The grain size distribution provided by Concept Laser was determined using laser diffraction and sieve analysis. The particle diameter distribution is specified by 10%, 50%, and 90% percentiles according to $Dv(10) = 20.278\mu m$, $Dv(50) = 31.313\mu m$, and $Dv(90) = 48.397\mu m$ with mean particle diameter $\overline{d} = 31.313\mu m = d_0$ (Table 2). The sample was sieved over 100μm, 80μm, 63μm, 45μm, 32μm, and 20μm sieves (Table 3).

Table 2: Results of the grain size distribution.

| Particle Size Distribution Percentiles | Unit | Result |
|---|---|---|
| Dv(10) | μm | 20.278 |
| Dv(50) | μm | 31.313 |
| Dv(90) | μm | 48.397 |
| Width (90;10) | | 0.898 |

Table 3: Results of the sieve analysis.

| Sample No. | | 17-01746-001 |
|---|---|---|
| Sample Name | | CL 101, Chg.: UK81452 |
| Grain Size | Unit | Result |
| < 100 μm | % | 100.0 |
| <80 μm | % | 100.0 |
| < 63 μm | % | 99.06 |
| < 45 μm | % | 98.91 |
| < 32 μm | % | 76.26 |
| <20 μm | % | 23.70 |

**Input Parameters**

Layer thickness of the spread powder is measurable using DEM simulations; however, it is difficult to calculate with a legitimate machine given the technology available. As it is defined, layer thickness is not accurately represented for the purposes of this study. Therefore, layer thickness is referred to as blade gap thickness ($t_{bg}$) as a more exact description of this measurement. Blade gap thickness is defined as the vertical distance between the tip of the blade and the build surface. It is important to note that blade gap thickness is not an actual measurement, but an input. It is distinguished by the difference between the supply up travel and the supply down travel. This is also equal to the build down travel.

The ratio between the surface area of the supply plate and the surface area of the build plate is 1.5. Therefore, the ratio of the amount of powder spread over the build plate from the supply plate is

also 1.5, which again, is distinguished by the difference between the supply up travel and the supply down travel being equal to the build down travel. Further studies could be done by altering this powder spread ratio. Increasing the amount of supply powder while maintaining the same blade gap thickness could prove to result in better layer quality.

In order to guarantee for a gap between the recoating blade and the largest powder particles, the maximum particle diameter, $d_{max} = 80\mu$m, is chosen according to the results from the sieve analysis (Table 3). Four different blade gap thicknesses ($t_{bg} = d_{max}, 2d_{max}, 3d_{max}$, and $4d_{max}$) and five different recoater velocities ($V_r = V_0, 2.5V_0, 5V_0, 10V_0, 15V_0$, where $V_0 = 10$mm/s) are investigated.

**Experimental Setup**

Trials are conducted for each blade gap by varying recoater velocity. Ten sample layers are recorded for each combination. Both density and surface roughness are calculated using the relative measurements recorded throughout the trials.

The build plate and the supply plate travel vertical distances according to the input controls. To ensure these distances are accurate, both plates must begin flush to the surface of the machine at a start position of 0mm. Since the recoater height remains constant, a paper touch test is used to set the start positions.

**Preparing the Supply Powder**

The supply plate is lowered 30mm. Before the powder is deposited into the supply, it is weighed using a Scientech SM 124D Semi-Micro Balance, and its mass is recorded. The maximum capacity of the scale is 120g, requiring some measurements to be divided into several smaller measurements.

First an empty, clean cup is weighed, and its mass is recorded $(m_{cup})$. Powder is then scooped from the source bucket and deposited into the cup. The cup, now with the powder, is weighed, and its mass is recorded $(m_{cup+powder})$. The powder from the cup is then emptied into the supply. The now empty cup is weighed, and its mass is recorded $(m_{cup})$. This process is repeated until powder fills the supply.

**Leveling the Supply Powder**

Before the trials can begin, both the powder over the supply plate and the powder over the build plate need to be leveled. The recoating process runs until the powder in the supply is visually smooth. The total displacement of the supply plate is recorded. The powder over the build plate and in the surrounding areas is swept into the overflow bin using a bristled brush. The empty cup from before is weighed, and its mass is recorded $(m_{cup})$. Powder from the overflow bin is incrementally poured into the cup. The cup, now containing overflow powder, is weighed, and its mass is recorded $(m_{cup+overflow})$. The overflow powder is then returned to the source bucket. The empty cup is weighed, and its mass is recorded $(m_{cup})$. This process is repeated as needed. After emptying out the remaining overflow powder, the overflow bin is cleaned and returned to the powder bed machine.

**Leveling the Build Powder**

The build plate is reset to start position 0mm using a paper touch test. The recoat process runs until the powder in the build is visually smooth. The total displacement of the supply plate and the build plate is recorded.

The powder in the surrounding areas is swept into the overflow bin using a bristled brush. The empty cup is weighed, and its mass is recorded $(m_{cup})$. Powder from the overflow bin is incrementally poured into the cup. The cup, now with overflow powder, is weighed, and its mass is recorded $(m_{cup+overflow})$. The overflow powder is then returned to the source bucket. The empty cup is weighed, and its mass is recorded $(m_{cup})$. This process is repeated as needed. After emptying out the remaining overflow powder, the overflow bin is cleaned and returned to the powder bed machine. The cup is also cleaned, and its mass is recorded. The cup is set aside for the trials.

This experimental setup process is performed once for the $t_{bg}$ =80μm and $t_{bg}$ =160μm trials. After completing the $t_{bg}$ =160μm trials, there was not enough powder remaining in the supply for the $t_{bg}$ =240μm and $t_{bg}$ =320μm trials. The machine was cleaned and reset using the same experimental setup procedure as above. The packing density of the supply for the $t_{bg}$ =80μm and $t_{bg}$ =160μm trials was calculated to be 59%, and the packing density of the supply for the $t_{bg}$ =240μm and $t_{bg}$ =320μm trials was 58%. While the difference in packing densities was taken into account during calculations, it can be assumed that the slight difference was negligible.

**Trials**

The temperature and humidity in the lab room is recorded using an Extech RH300 Psychrometer before each trial to ensure the capillary forces within the powder remain consistent. No significant change was recorded for temperature or humidity in the lab over the course of the trials.

The GUI program inputs are set starting at $t_{bg}$ =80μm and $V_r = 10$mm/s. The recoating process sequence occurs one time, spreading a layer across the build plate. Once the recoater returns to its start position, the powder bed machine lid is opened. A NextLED 200 Lumen Battery Powered,

Flexible Neck, LED Work Light is placed on top of the flow channel, perpendicular to the recoating direction (Figure 24). The shadows help to highlight the surface defects. The lab lights are turned off, and a Cannon 80D camera with a 100mm macro lens is used to take pictures of the powder in the center of the build plate. Once complete, the flashlight is removed, the lab lights are turned on, and the powder bed machine lid is closed. The bottom of the powder bed machine is opened, and the overflow bin is removed. The overflow powder is emptied from the overflow bin into the empty cup. The cup is weighed, and its mass is recorded. The overflow powder is returned to the source bucket. The empty cup is weighed, and its mass is recorded. The overflow bin is returned to the powder bed machine, and the bottom is closed. This process is repeated for each layer of the trials.
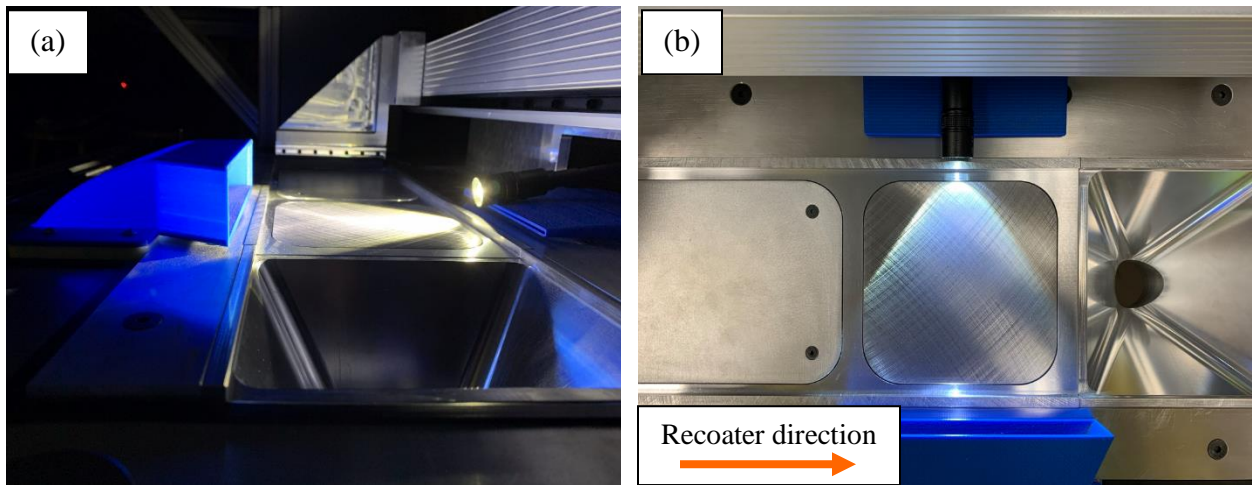


**Figure 24.** Flashlight orientation across build plate.

**Post Processing**

Surface roughness was calculated using ImageJ. Images taken from the trials were first imported into Adobe Lightroom. To ensure the images were processed correctly and in the same way, they were cropped and converted to black and white (Appendix D). From there, the images were individually loaded into ImageJ, and analyzed using a surface roughness plugin. ImageJ is an

image processing software that converts topographical information from the pixel intensities into numerical values representing surface roughness. For reference, black = 0 and white = 255. The value ImageJ provides is Ra, which is the arithmetical mean roughness value calculated from the absolute values of the profile height deviations of the mean line (Appendix E). The final surface roughness value is calculated by dividing the Ra values by 255. Packing density was calculated using the series of equations and mass measurements located in Appendix A, Appendix B, and Appendix C.

**Error**

The measurements in this study are not perfect. There are several instances in which not every powder particle is accounted for. The powder adhered to the recoating blade, the inside of the overflow bin, and the inside of the cup. The powder also wedged inside the small gap between the surface plate and the build plate. Additionally, the powder got caught between the brush bristles when it was swept into the overflow bin. Furthermore, opening and closing the powder bed machine for each sample potentially shifted the powder particles.

To minimize this error, each measurement and subsequent action was replicated to be as identical as humanly possible. For example, each time the overflow powder was emptied into the cup, the overflow bin was held over the cup at 180˚, and tapped in a counterclockwise motion five times, using a similar force. Ideally, the same amount of error occurred in each measurement, making the values comparable.

**Results and Discussion**

In this study, packing density and surface roughness were calculated while varying blade gap thickness and recoater velocity. Ideal layer quality is defined as having maximum packing density and minimum surface roughness.

**Powder Layer Quality**

As expected, surface roughness increased with increasing velocity, and decreased with increasing blade gap thickness (Figure 25 (a) (c)). Comparatively, packing density decreased with increasing velocity, and increased with increasing blade gap thickness (Figure 25 (b) (d)).
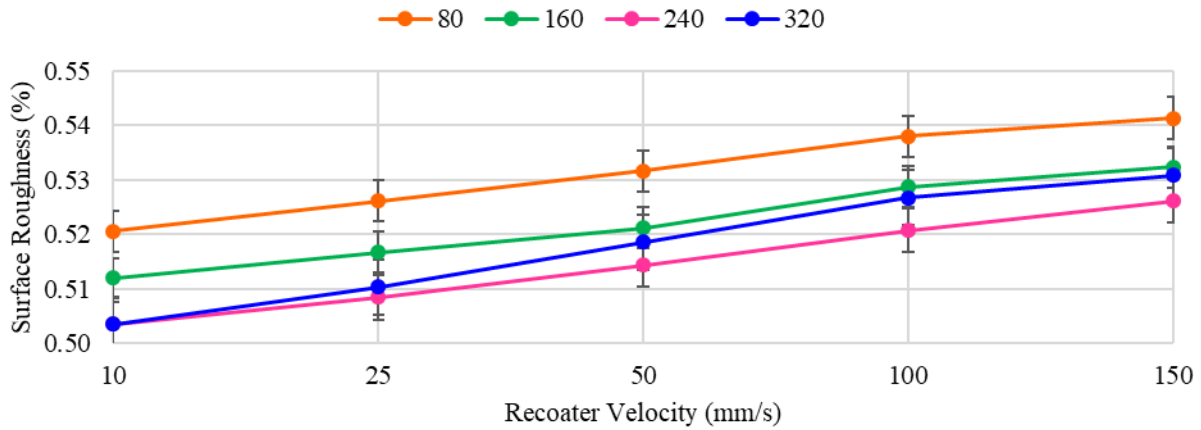


(a) Recoater velocity vs surface roughness for varying blade gap thicknesses.
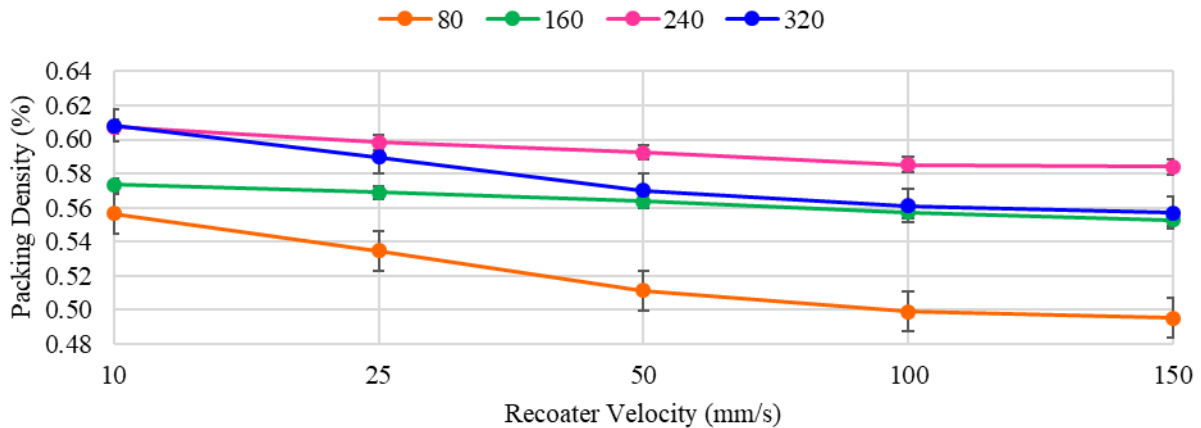


(b) Recoater velocity vs packing density for varying blade gap thicknesses.
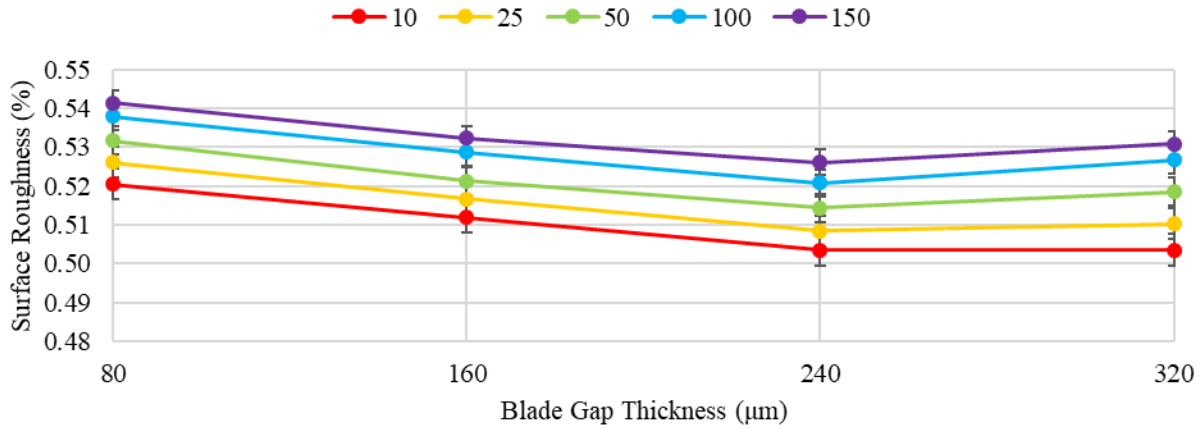
(c) Blade gap thickness vs surface roughness for varying recoater velocities.


(d) Blade gap thickness vs packing density for varying recoater velocities.
**Figure 25.** Surface roughness and packing density trial results.

At higher velocities, the number of particle voids increased, which created a larger variation in the layer height, and a higher porosity within the layer powder. At lower blade gap thicknesses, agglomerates do not pass under the blade as easily, which initiated more resistance forces and decreased the powder flowability.

It was observed that at higher speeds, the recoating arm increasingly vibrated. Generally, controlled vibration integrated into a powder bed machine can be used to produce higher quality powder layers. The added movement encourages settling and causes agglomerates to break down,

increasing powder flowability. In this study, the recoater vibration was unintentional, not quantified, and randomly occurred in all directions of the XYZ-coordinate system. Interestingly, the vibration only impacted the quality of the powder bed at $t_{bg}$= 320μm (Figure 26).



(a) Recoater velocity vs surface roughness for varying blade gap thicknesses
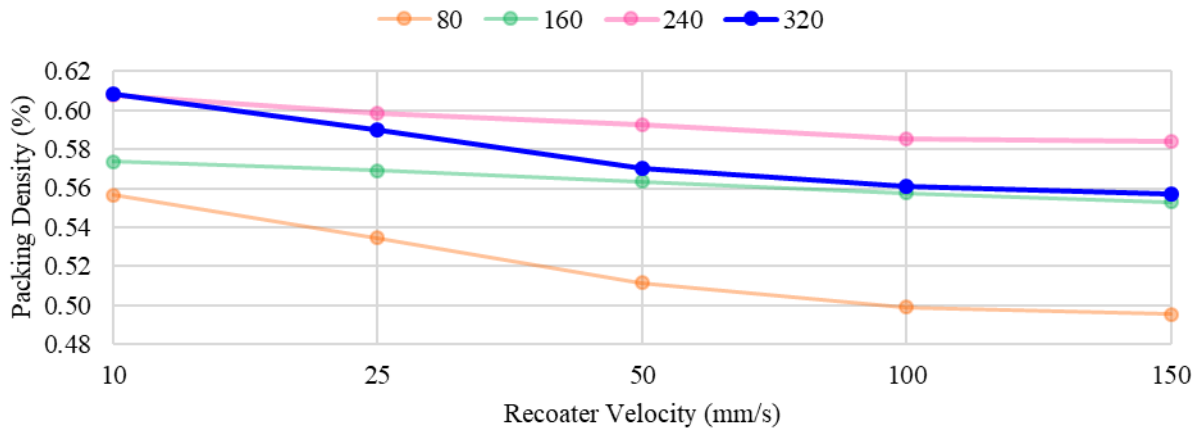


(b) Recoater velocity vs packing density for varying blade gap thicknesses.
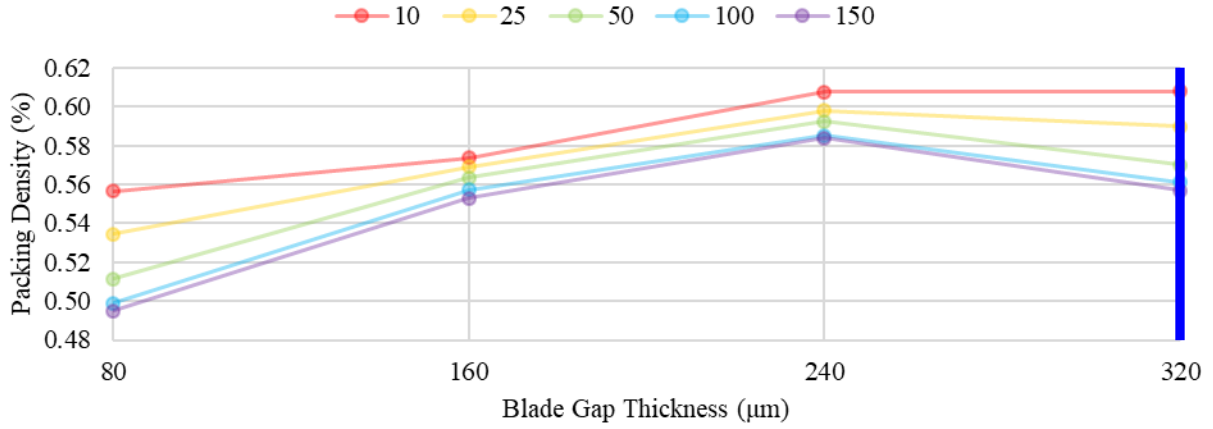
(c) Blade gap thickness vs surface roughness for varying recoater velocities.
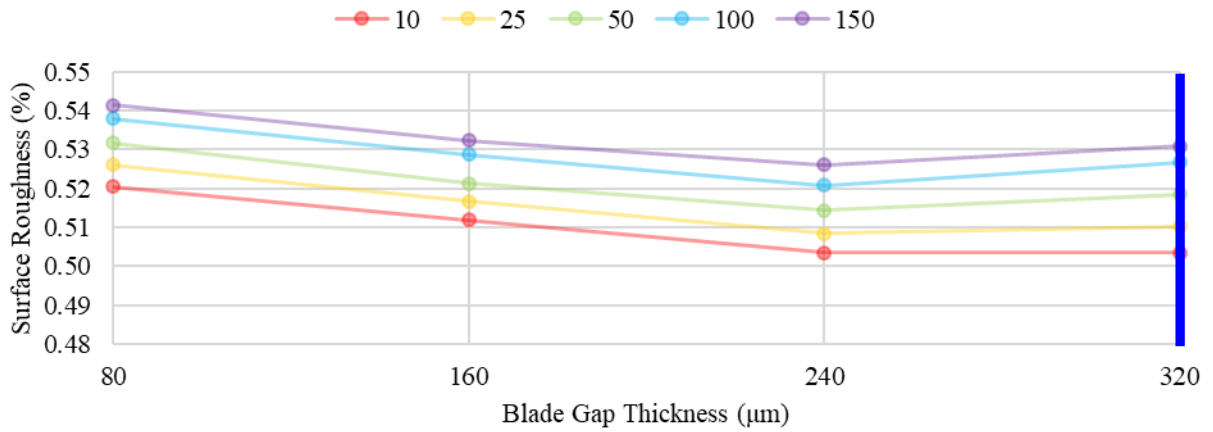


(d) Blade gap thickness vs packing density for varying recoater velocities.
**Figure 26.** Trial results highlighting $t_{bg}$ = 320μm.

As the velocity increased for $t_{bg}$ = 320μm, lines in the surface became more defined (Figure 27).

(a) $t_{bg} = 80\mu m$, $V_r = 10mm/s$

(b) $t_{bg} = 80\mu m$, $V_r = 150mm/s$

Flashlight direction

Recoater direction

(c) $t_{bg} = 240\mu m$, $V_r = 10mm/s$

(d) $t_{bg} = 240\mu m$, $V_r = 150mm/s$

(e) $t_{bg} = 320\mu m$, $V_r = 10mm/s$

(f) $t_{bg} = 320\mu m$, $V_r = 150mm/s$
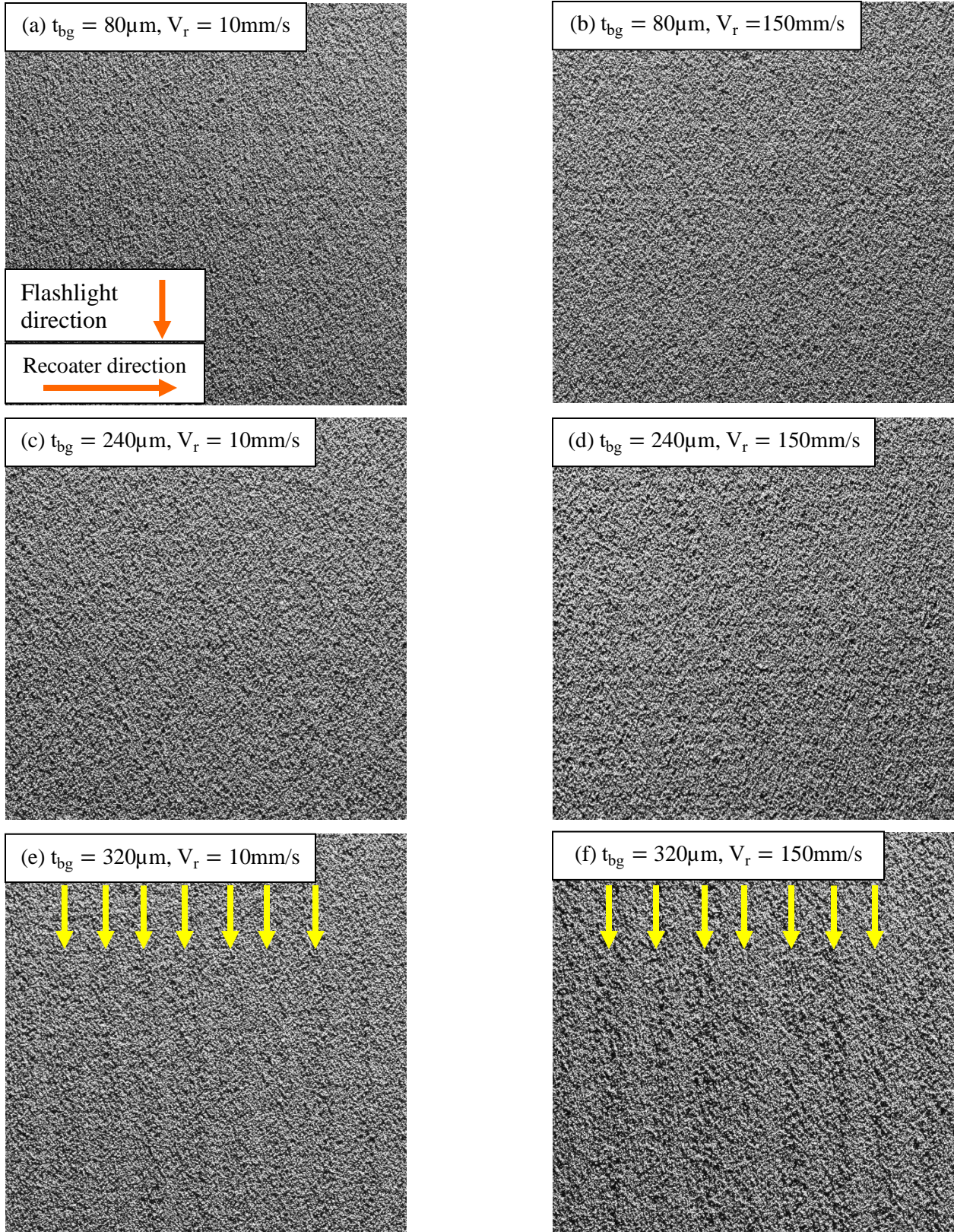
**Figure 27.** Images of sample layers from trials.

This is not because the surface roughness accumulated as more layers were spread. The raw data from $t_{bg} = 320\mu m$ shows that the surface roughness still varied as the trials proceeded though samples with the same blade gap thickness and recoater velocities (Table 4).

**Table 4.** ImageJ values for $t_{bg} = 320\mu m$ trials.

| $V_r$ | 1 | 2 | 3 | 4 | 5 | 6 | 7 | 8 | 9 | 10 | Average |
|---|---|---|---|---|---|---|---|---|---|---|---|
| 10 | 126.37 | 128.76 | 129.25 | 127.24 | 131.06 | 127.02 | 126.14 | 128.62 | 131.15 | 128.37 | 128.40 |
| 25 | 128.14 | 127.70 | 127.72 | 128.76 | 131.91 | 132.67 | 133.56 | 128.73 | 126.27 | 131.04 | 129.65 |
| 50 | 127.77 | 132.32 | 132.95 | 131.04 | 133.36 | 135.59 | 132.56 | 126.77 | 127.11 | 132.25 | 131.17 |
| 100 | 132.21 | 133.38 | 130.61 | 134.32 | 132.58 | 135.45 | 131.39 | 129.15 | 134.23 | 134.58 | 132.79 |
| 150 | 131.84 | 133.32 | 135.44 | 132.64 | 134.92 | 131.60 | 136.35 | 135.88 | 136.28 | 133.38 | 134.16 |

The cause of this effect is unknown. As far as the author is aware, there are no instances in literature in which vibration is not applied to all layers evenly. At $t_{bg} = 320\mu m$, the powder layer quality decreases at similar rates to $t_{bg} = 80\mu m$ (Figure 28).
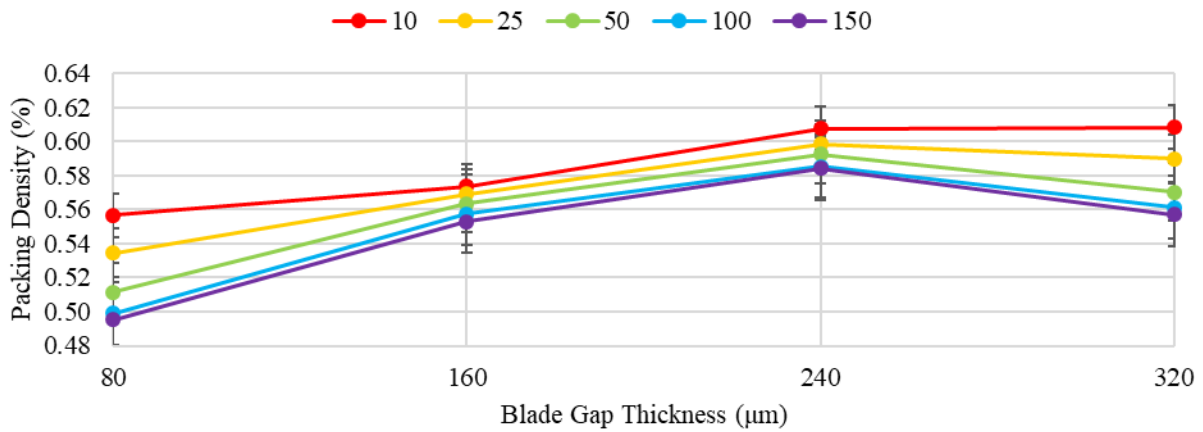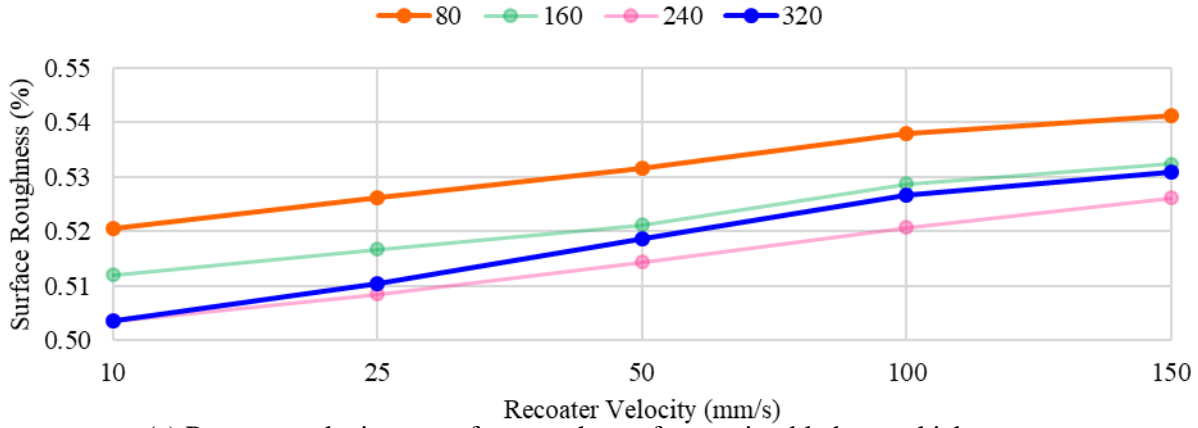


(a) Recoater velocity vs surface roughness for varying blade gap thicknesses
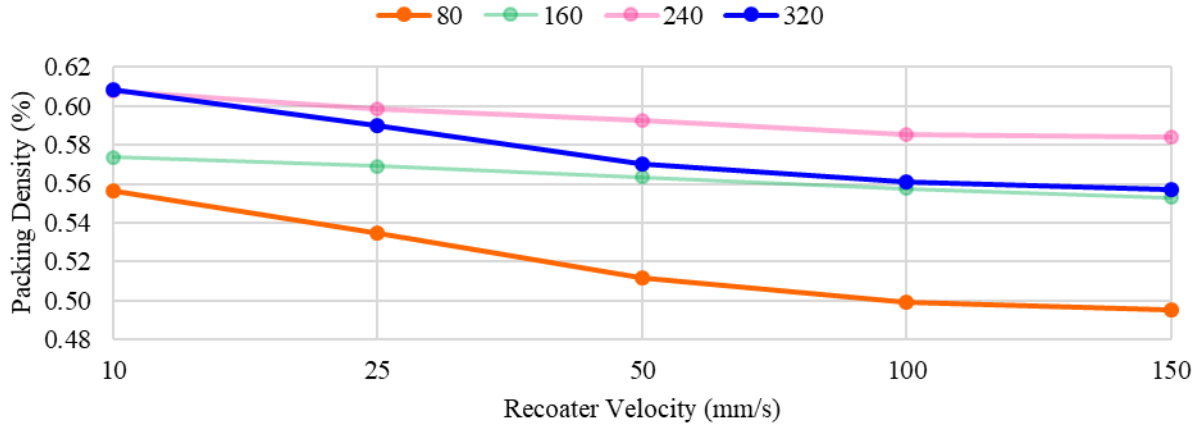
(b) Recoater velocity vs packing density for varying blade gap thicknesses.
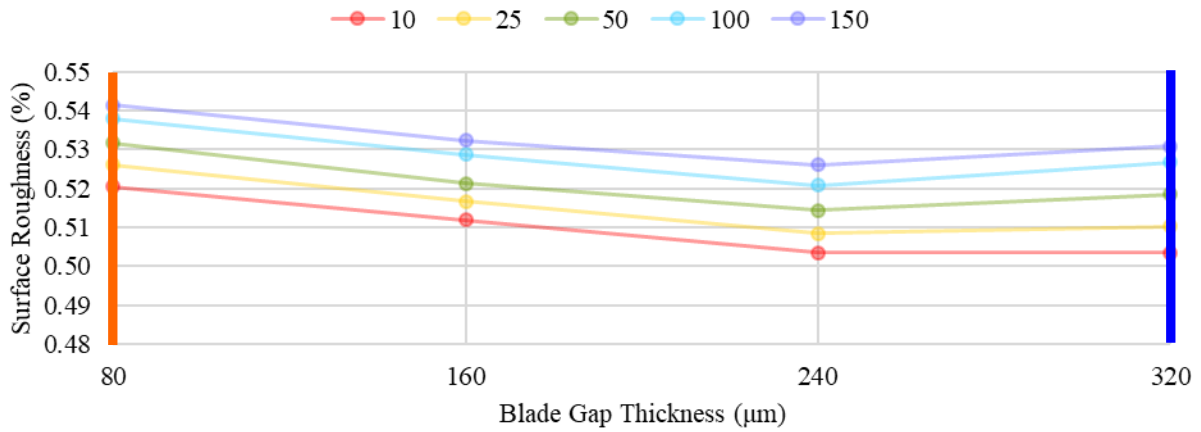


(c) Blade gap thickness vs surface roughness for varying recoater velocities.



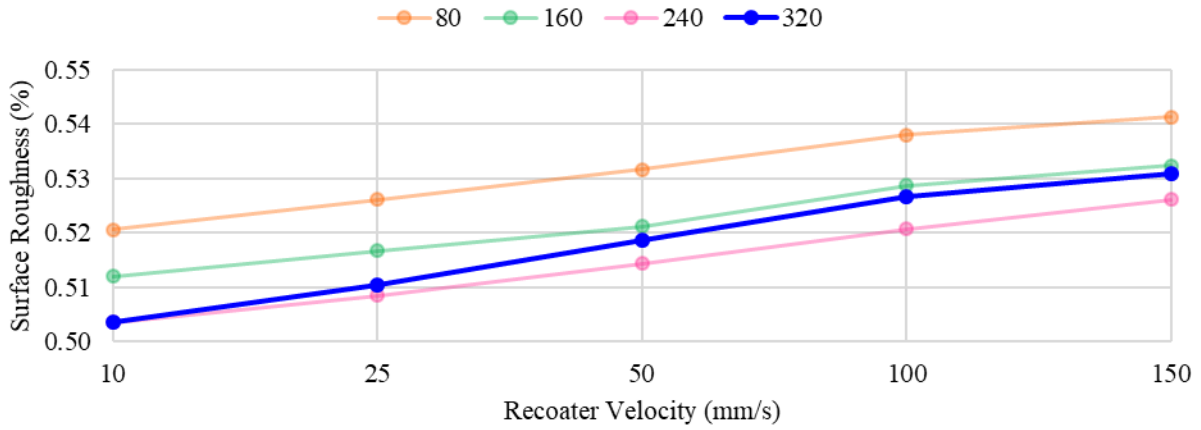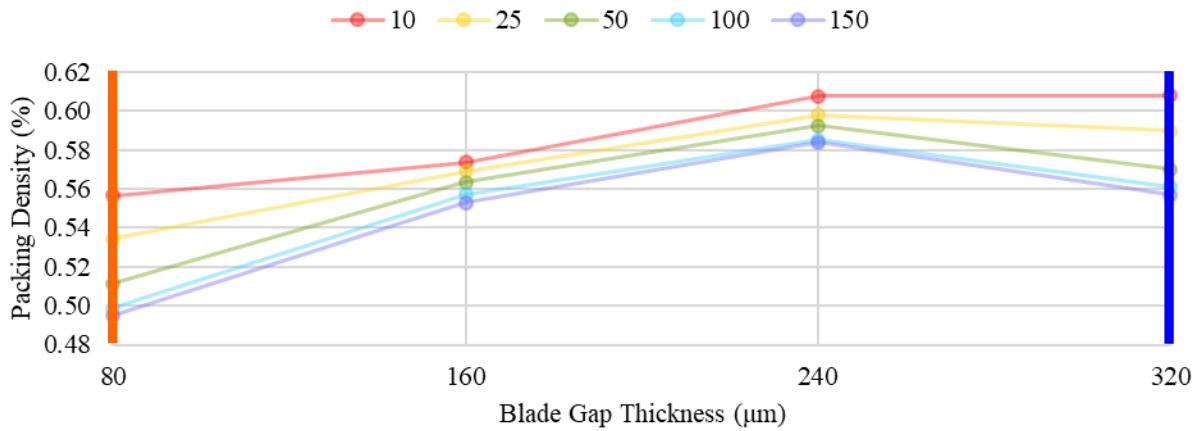(d) Blade gap thickness vs packing density for varying recoater velocities.
**Figure 28.** Trial results highlighting $t_{bg}$ =320μm and $t_{bg}$ =80μm.

The particle-to-blade adhesion is stronger at $t_{bg} = 80\mu$m compared to $t_{bg} = 160\mu$m and $t_{bg} = 240\mu$m because the blade is closer to the powder bed. Cohesive forces could lead to an explanation as to why $t_{bg} = 320\mu$m behaves in a similar manner, however no supporting evidence has been found.

One study noticed that surface roughness surprisingly increased with the addition of roller vibration [22]. Compaction is generally limited to the thin layer that is spread over a solid surface, and corresponds to two to three particles on average. In this study, the vibration impacted layers that were at least four particles in thickness, which may be an explanation for this phenomenon.

**Linear Regression Analysis**

Linear regression analyses were used to quantify exactly how blade gap thickness and recoater velocity affect both surface roughness and packing density (Figure 29). The high $R^2$ values indicate that the models explain much of the variation in packing density and surface roughness data. The surface roughness $R^2$ value is noticeably higher than the packing density $R^2$ value, which would suggest that blade gap thickness and recoater velocity better explain variation in surface roughness than in packing density. The significantly low P-values for all coefficients in both models confirm that the blade gap thickness and recoater velocity are strongly correlated with both packing density and surface roughness.

| Packing Density | Coefficients | Standard Error | t Stat | P-value |
|---|---|---|---|---|
| Intercept | 0.530 | 0.0121 | 43.71 | 6.58E-19 |
| Blade Gap Thickness (μm) | 0.000255 | 4.88E-05 | 5.22 | 6.90E-05 |
| Recoater Velocity (mm/s) | -0.000256 | 8.48E-05 | -3.02 | 0.00768 |

$R^2$ | **0.68**

| Surface Roughness | Coefficients | Standard Error | t Stat | P-value |
|---|---|---|---|---|
| Intercept | 0.523 | 0.0027 | 190.93 | 9.17E-30 |
| Blade Gap Thickness (μm) | -0.000060 | 1.10E-05 | -5.44 | 4.38E-05 |
| Recoater Velocity (mm/s) | 0.000156 | 1.92E-05 | 8.16 | 2.80E-07 |

$R^2$ | **0.85**

**Figure 29.** Linear regression analyses.

Packing density (PD) and surface roughness (SR) are represented as functions of blade gap thickness (BG) and recoater velocity (RV) in the following equations that were developed from the linear regression analyses seen in Figure 29:

$$PD = 0.530 + 0.000255(BG) - 0.000256(RV) \tag{5}$$

$$SR = 0.523 - 0.000060(BG) + 0.000156(RV) \tag{6}$$

Excluding $t_{bg}$ =320μm leads to the observation of even stronger relationships (Figure 30). With 320μm included, the packing density model had an $R^2$ of 0.68. When the data corresponding with a blade gap thickness of 320μm was removed, the $R^2$ improved to 0.92. A similar observation can be made when looking at the surface roughness models, whose $R^2$ jumped from 0.85 to 0.97 when removing the 320μm data.

| Packing Density (excluding 320µm) | Coefficients | Standard Error | t Stat | P-value |
|---|---|---|---|---|
| Intercept | 0.500 | 0.0081 | 61.73 | 2.16E-16 |
| Blade Gap Thickness (µm) | 0.000464 | 4.21E-05 | 11.02 | 1.24E-07 |
| Recoater Velocity (mm/s) | -0.000232 | 5.33E-05 | -4.35 | 0.00095 |

$R^2$ | **0.92**

| Surface Roughness (excluding 320µm) | Coefficients | Standard Error | t Stat | P-value |
|---|---|---|---|---|
| Intercept | 0.530 | 0.0016 | 330.02 | 4.03E-25 |
| Blade Gap Thickness (µm) | -0.000105 | 8.34E-06 | -12.64 | 2.70E-08 |
| Recoater Velocity (mm/s) | 0.000146 | 1.06E-05 | 13.82 | 9.88E-09 |

$R^2$ | **0.97**

**Figure 30.** Linear regression analyses excluding $t_{bg}$ =320µm.

Packing density (PD) and surface roughness (SR) are represented as functions of blade gap thickness (BG) and recoater velocity (RV) in the following equations that were developed from linear regression analyses in Figure 30:

$$PD = 0.500 + 0.000464(BG) - 0.000232(RV) \tag{7}$$

$$SR = 0.530 - 0.000105(BG) + 0.000146(RV) \tag{8}$$

Excluding $t_{bg}$ =320µm suggests that too large of a blade gap can be counterproductive when trying to improve layer quality. This confirms the conclusions found in previous research indicating that the optimum powder layer quality is usually reached at two to three times the maximum particle diameter for cohesive powders [15].

While the previous linear regression analyses were able to establish general trends, it was important to also establish optimum operating parameters for the recoating process. A ratio between the packing density and surface roughness was created to help quantify which combination of input parameters produced the most optimum layer quality. This ratio is represented by the following equation:

$$ratio = \frac{PD}{SR} \tag{9}$$

Based on how this ratio was calculated, it can be surmised that at higher ratios, the layer quality will be better. In order to find the optimum blade gap thickness and recoater velocity that provided the best layer quality, a multiple linear regression analysis was first considered as a possible method. However, a limiting factor of linear regression is the generated equations have no maximum, and therefore, cannot be utilized to find the optimum point. Additionally, trendlines were used to determine which type of relationship had the highest $R^2$ value between the ratio and blade gap thickness. The data was found to be best fit with a quadratic trend line, which is not compatible with linear regression.

To find the optimum blade gap thickness point, the blade gap thickness was graphed against the calculated ratio, and a quadratic trendline was calculated (Figure 31). The equation that corresponded with this trendline was utilized to find the maximum value. This was done by finding the derivative of the trendline equation, setting it equal to zero, and solving for the corresponding blade gap thickness. From this process, it was found that a blade gap thickness of 256μm produces the highest layer quality.
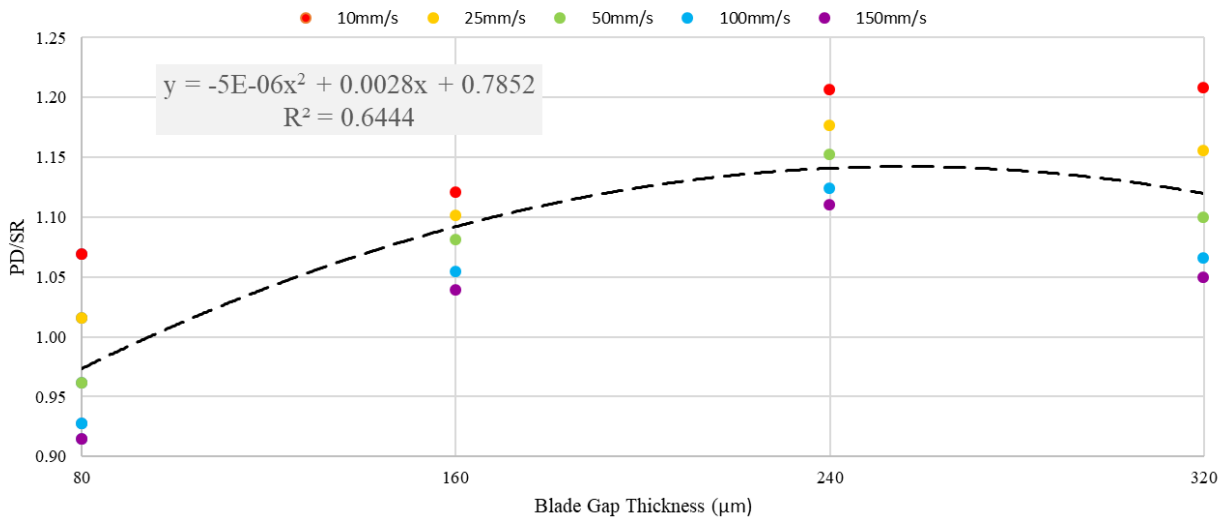


**Figure 31.** Blade gap thickness vs PD/SR ratio.

40

In contrast to blade gap thickness, the relationship between the ratio and recoater velocity was still found to be linear. Based on the data collected from this study, the exact optimum recoater velocity could not be conclusively determined. A general trend, showing that as recoater velocity decreases, layer quality improves, was shown to be statistically significant. However, because the relationship had been found to be linear, no peak was apparent for use in finding an optimum point. It is possible that recoater velocities less than 10mm/s could perform worse, however velocities this slow were not utilized in this study. This was primarily due to the necessity to stay within realistic machine productivity. Therefore, it is concluded that 10mm/s is likely to be the optimum recoater velocity that produces the highest layer quality.

**Conclusion**

This study focused on quantifying the impact recoater velocity and blade gap thickness have on the powder layer quality. Ideal powder layer quality is defined as having maximum packing density and minimum surface roughness. A uniform powder layer is necessary for the laser to penetrate the material evenly, building a mechanically stronger part that contains less defects.

Inconel 625 powder, with an average particle size of 31.3313µm, was used to study the powder bed parameters. In general, the surface roughness decreased with increasing blade gap thickness, and increased with increasing recoater velocity. The packing density increased with increasing blade gap thickness, and decreased with increasing recoater velocity.

Due to unintentional recoater vibration, $t_{bg}$ =320µm resulted in unusual behavior that resembled the behavior of $t_{bg} = 80$µm. The smallest blade gap thickness ($t_{bg}= 80$µm) is more sensitive to recoater velocity than the other thicknesses due to the stronger presence of particle-to-blade

adhesion. It is unknown exactly what caused this to occur, but cohesive forces could lead to an explanation for the phenomenon.

While $V_r = $ 10mm/s and $t_{bg}$ =320μm does result in the highest packing density and lowest surface roughness in this study, the results are unreliable due to the behavior at subsequent input parameters. Linear regression analyses were used to identify exactly what input parameters produce the best layer quality. In conclusion, the most optimum powder layers occur at $V_r = $ 10mm/s and $t_{bg}$ =256μm.

Future studies need to be conducted looking at how exactly vibration and compaction affect layer quality at varying powder characteristics and recoating process parameters. Even though general powder behavior trends have been confirmed by this study and numerous others, further analysis is still needed to better understand the recoating process. Repeating experiments using legitimate machines is difficult considering all of the variability with powder behavior and recoater parameters. However, it is important to quantify exactly how these trends react in order to improve the production and properties of additively manufactured parts.

References

[1]     Fouda, Yahia M., and Andrew E. Bayly. "A DEM study of powder spreading in additive layer manufacturing." *Granular Matter* 22.1 (2020): 10.

[2]     Foster, B., et al. "Optical, layerwise monitoring of powder bed fusion." Solid Freeform Fabrication Symposium, Austin, TX, Aug. 2015.

[3]     Beitz, Steffen, et al. "Influence of Powder Deposition on Powder Bed and Specimen Properties." Materials 12.2 (2019): 297.

[4]     Brika, Salah Eddine, et al. "Influence of particle morphology and size distribution on the powder flowability and laser powder bed fusion manufacturability of Ti-6Al-4V alloy." Additive Manufacturing 31 (2020): 100929.

[5]     Olakanmi, Eyitayo Olatunde. "Effect of mixing time on the bed density, and microstructure of selective laser sintered (sls) aluminium powders." Materials Research 15.2 (2012): 167-176.

[6]     Clayton, Jamie. "Optimising metal powders for additive manufacturing." Metal Powder Report 69.5 (2014): 14-17.

[7]     Gülsoy, H. Özkan, Nagihan Gülsoy, and Rahmi Calışıcı. "Particle morphology influence on mechanical and biocompatibility properties of injection molded Ti alloy powder." Bio-medical materials and engineering 24.5 (2014): 1861-1873.

[8]     Dawes, Jason, et al. "Introduction to the Additive Manufacturing Powder Metallurgy Supply Chain." Johnson Matthey Technology Review, vol. 59, no. 3, 2015, pp. 243–256.

[9]     Weinberg, Johannes. A precision blade mechanism for powder recoating in Selective Laser Melting. Diss. Massachusetts Institute of Technology, 2018.

[10]  Muñiz-Lerma, Jose Alberto, et al. "A Comprehensive Approach to Powder Feedstock Characterization for Powder Bed Fusion Additive Manufacturing: A Case Study on AlSi7Mg." Materials 11.12 (2018): 2386.

[11]  Parteli, Eric JR, and Thorsten Pöschel. "Particle-based simulation of powder application in additive manufacturing." Powder Technology 288 (2016): 96-102.

[12]  Li, Hongming. Impact of cohesion forces on particle mixing and segregation. Diss. University of Pittsburgh, 2006.

[13]  Spath, Sebastian, and Hermann Seitz. "Influence of grain size and grain-size distribution on workability of granules with 3D printing." *The International Journal of Advanced Manufacturing Technology* 70.1-4 (2014): 135-144.

[14]  Olakanmi, Eyitayo Olatunde. "Effect of mixing time on the bed density, and microstructure of selective laser sintered (sls) aluminium powders." Materials Research 15.2 (2012): 167-176.

[15]  Meier, Christoph, et al. "Critical influences of particle size and adhesion on the powder layer uniformity in metal additive manufacturing." Journal of Materials Processing Technology 266 (2019): 484-501.

[16]  Xiang, Zhaowei, et al. "Simulation of forming process of powder bed for additive manufacturing." Journal of Manufacturing Science and Engineering 138.8 (2016).

[17]  Mindt, H. W., et al. "Powder bed layer characteristics: the overseen first-order process input." Metallurgical and Materials Transactions A 47.8 (2016): 3811-3822.

[18]  Escano, Luis I., et al. "Revealing particle-scale powder spreading dynamics in powder-bed-based additive manufacturing process by high-speed x-ray imaging." Scientific reports 8.1 (2018): 1-11.

[19]     Mindt, H-W., et al. "Modeling of powder bed manufacturing defects." Journal of Materials Engineering and Performance 27.1 (2018): 32-43.

[20]     Haeri, S., et al. "Discrete element simulation and experimental study of powder spreading process in additive manufacturing." Powder Technology 306 (2017): 45-54.

[21]     Haeri, Sina. "Optimisation of blade type spreaders for powder bed preparation in Additive Manufacturing using DEM simulations." Powder Technology 321 (2017): 94-104.

[22]     Parteli, Eric JR. "Effect of vibrations applied to the transport roller in the quality of the powder bed during additive manufacturing."

Supply Fill Process

$$m_{enter} = \sum (m_{cup+powder} - m_{cup})$$

Supply Level Process

$$m_{overflow} = \sum (m_{cup+powder} - m_{cup})$$

$$m_{supply} = m_{enter} - m_{overflow}$$

Build Level Process

$$m_{overflow} = \sum (m_{cup+powder} - m_{cup})$$

$$m_{supply} = m_{enter} - m_{overflow}$$

Supply Packing Density

$$\phi_{supply} = \frac{V_{supply,actual}}{V_{supply,ideal}}$$

$$V_{supply,actual} = m_{supply}(\rho_{Inconel\ 625})$$

$$V_{supply,ideal} = SA_{supply\ plate}(\Delta X_{supply\ plate})$$

Supply Density

$$\rho_{supply} = \frac{m_{supply}}{V_{supply,ideal}}$$

Layer Mass

$$m_{layer} = m_{supply\ lost\ per\ layer,actual} - m_{overflow}$$

$$m_{supply\ lost\ per\ layer,actual} = \rho_{supply}(V_{supply\ lost\ per\ layer,ideal})$$

$$V_{supply\ lost\ per\ layer,ideal} = t_{bg}(SA_{supply\ plate})$$

Layer Packing Density

$$\phi_{layer} = \frac{V_{layer,actual}}{V_{build\ added\ per\ layer,ideal}}$$

$$V_{layer,actual} = \frac{m_{layer}}{\rho_{Inconel\ 625}}$$

$$V_{build\ added\ per\ layer,ideal} = t_{bg}(SA_{build\ plate})$$

Appendix B: Experimental Setup Mass Measurements

**Table B1.** Supply fill process for $t_{bg}$ =80μm and $t_{bg}$ =160μm trials.

| $m_{cup}$ (g) | $m_{cup + powder}$ (g) | $m_{cup}$ (g) | $m_{cup + powder}$ (g) |
|---|---|---|---|
| 39.69453 | 90.4339 | 40.6953 | 89.8390 |
| 40.2248 | 74.8909 | 40.6937 | 87.7868 |
| 40.5074 | 90.6831 | 40.6964 | 90.7528 |
| 40.4664 | 102.7125 | 40.5839 | 80.2518 |
| 40.8004 | 95.0427 | 40.6493 | 102.8643 |
| 41.2003 | 86.9138 | 40.7315 | 90.2873 |
| 41.4669 | 85.7079 | 40.8001 | 85.7541 |
| 41.4494 | 83.4103 | 40.7301 | 97.2472 |
| 41.4427 | 93.3141 | 40.5401 | 101.1825 |
| 42.0231 | 91.2803 | 40.5181 | 90.1530 |
| 40.7720 | 86.0648 | 40.6362 | 90.8154 |
| 41.0008 | 72.3203 | 40.5354 | 91.7771 |
| 40.9644 | 78.8206 | 40.6616 | 88.7141 |
| 40.7746 | 92.9538 | 40.6127 | 82.8538 |
| 40.9059 | 95.0767 | 40.6640 | 108.3810 |
| 40.6775 | 87.0762 | 40.6265 | 98.2785 |
| 40.7905 | 94.8439 | 40.5118 | 101.0676 |
| 40.8516 | 91.8209 | 40.5861 | 97.2108 |
| 40.8058 | 85.9680 | 40.6277 | 83.4189 |
| 40.6215 | 103.6727 | 40.5637 | 100.6641 |
| 40.5457 | 104.6838 | 40.4873 | 77.6553 |
| 40.6074 | 98.7818 | 40.5346 | 84.4060 |
| 40.5048 | 99.4717 | 40.4290 | 97.5307 |
| 40.5671 | 104.2089 | 41.3672 | 82.6381 |
| 40.6607 | 101.6501 | 41.2851 | 102.3057 |
| 40.8256 | 106.6649 | 41.9354 | 87.2703 |
| 40.7347 | 107.7127 | 42.4349 | 80.6273 |
| 40.8624 | 103.2638 | 43.3551 | 94.3957 |
| 40.8204 | 94.6574 | 42.7373 | 91.9389 |
|  |  | 43.4447 |  |

**Table B2.** Supply level process for $t_{bg} = 80\mu m$ and $t_{bg} = 160\mu m$ trials.

| $m_{cup}$ (g) | $m_{cup + powder}$ (g) |
|---|---|
| 43.4447 | 71.7776 |
| 40.6574 | 79.3655 |
| 40.5224 | 83.2165 |
| 40.3255 | |

**Table B3.** Build level process for $t_{bg} = 80\mu m$ and $t_{bg} = 160\mu m$ trials.

| $m_{cup}$ (g) | $m_{cup + powder}$ (g) |
|---|---|
| 15.65832 | 29.1069 |

**Table B4.** Supply fill process for $t_{bg}$ =240μm and $t_{bg}$ =320μm trials.

| $m_{cup}$ (g) | $m_{cup + powder}$ (g) |
| --- | --- |
| 15.6997 | 94.1401 |
| 16.2445 | 97.5858 |
| 15.9280 | 99.8869 |
| 16.3715 | 96.5657 |
| 15.9597 | 98.9566 |
| 16.0529 | 55.5028 |
| 16.8217 | 98.4943 |
| 16.0126 | 99.9753 |
| 16.6783 | 86.7904 |
| 16.0279 | 106.0228 |
| 17.4092 | 107.1416 |
| 17.3897 | 91.3212 |
| 16.8529 | 102.3464 |
| 18.1577 | 88.7719 |
| 17.3397 | 76.5701 |
| 17.2581 | 93.3600 |
| 17.3633 | 103.9993 |
| 17.7083 | 102.1569 |
| 17.5222 | 96.2426 |
| 17.7517 | 109.1060 |
| 16.3154 | 92.5480 |
| 16.5903 | 119.9559 |
| 17.7596 | 99.5760 |
| 17.6796 | 99.5609 |
| 17.8622 | 97.0189 |
| 17.9345 | 97.5086 |
| 17.8125 | 109.6052 |
| 16.9701 | 103.4437 |
| 17.7351 | 84.8650 |

| $m_{cup}$ (g) | $m_{cup + powder}$ (g) |
| --- | --- |
| 18.3074 | 95.3519 |
| 18.4833 | 103.0152 |
| 17.6937 | 33.8374 |
| 16.9181 | |

**Table B5.** Supply level process for $t_{bg}$ =240μm and $t_{bg}$ =320μm trials.

| $m_{cup}$ (g) | $m_{cup + powder}$ (g) |
|---|---|
| 16.9181 | 69.4529 |
| 16.2891 | 53.8844 |
| 16.2553 | 79.6521 |
| 16.3160 | |

**Table B6.** Build level process for $t_{bg}$ =240μm and $t_{bg}$ =320μm trials.

| $m_{cup}$ (g) | $m_{cup + powder}$ (g) |
|---|---|
| 15.6920 | 29.4849 |
| 15.9660 | |

# Appendix C: Trials Mass Measurements

**Table C1.** Mass measurements of $t_{bg} = 80\mu m$ trials.

| $V_r = 10mm/s$ | 1 | 2 | 3 | 4 | 5 | 6 | 7 | 8 | 9 | 10 | |
|---|---|---|---|---|---|---|---|---|---|---|---|
| $m_{cup}$ (g) | 16.1726 | 16.2931 | 16.4640 | 16.5174 | 16.4205 | 16.5722 | 16.6046 | 16.6522 | 16.6522 | 16.7751 | 16.6963 |
| $m_{cup + powder}$ (g) | 19.8759 | 19.4242 | 19.4248 | 19.9062 | 19.4594 | 20.3395 | 20.3395 | 20.3465 | 20.7199 | 20.6489 | |

| $V_r = 25mm/s$ | 1 | 2 | 3 | 4 | 5 | 6 | 7 | 8 | 9 | 10 | |
|---|---|---|---|---|---|---|---|---|---|---|---|
| $m_{cup}$ (g) | 16.6963 | 16.7743 | 16.9437 | 16.8017 | 16.7486 | 16.8032 | 16.8179 | 16.8782 | 16.8290 | 16.8965 | 16.8970 |
| $m_{cup + powder}$ (g) | 19.7669 | 20.2894 | 20.4812 | 20.3732 | 20.3915 | 20.9885 | 20.7473 | 20.9123 | 20.8933 | 20.8659 | |

| $V_r = 50mm/s$ | 1 | 2 | 3 | 4 | 5 | 6 | 7 | 8 | 9 | 10 | |
|---|---|---|---|---|---|---|---|---|---|---|---|
| $m_{cup}$ (g) | 16.8970 | 16.8697 | 16.8608 | 16.8572 | 16.8802 | 16.8993 | 16.9093 | 16.9011 | 16.8809 | 16.8752 | 16.8959 |
| $m_{cup + powder}$ (g) | 20.4741 | 20.8505 | 20.8837 | 20.7788 | 20.7142 | 21.2620 | 20.9404 | 20.9598 | 20.9320 | 20.9503 | |

| $V_r = 100mm/s$ | 1 | 2 | 3 | 4 | 5 | 6 | 7 | 8 | 9 | 10 | |
|---|---|---|---|---|---|---|---|---|---|---|---|
| $m_{cup}$ (g) | 16.8959 | 16.8996 | 16.8796 | 16.8825 | 16.8838 | 16.8952 | 16.9162 | 16.9152 | 16.9198 | 16.9208 | 16.8998 |
| $m_{cup + powder}$ (g) | 21.0480 | 20.8725 | 20.9200 | 21.0554 | 20.9522 | 21.3258 | 20.8135 | 21.0563 | 21.1380 | 21.0223 | |

| $V_r = 150mm/s$ | 1 | 2 | 3 | 4 | 5 | 6 | 7 | 8 | 9 | 10 | |
|---|---|---|---|---|---|---|---|---|---|---|---|
| $m_{cup}$ (g) | 16.8998 | 16.8973 | 16.9056 | 16.9082 | 16.9168 | 16.9046 | 16.8976 | 16.9158 | 16.9085 | 16.9153 | 16.9149 |
| $m_{cup + powder}$ (g) | 21.3298 | 21.1531 | 21.2805 | 20.9894 | 20.9337 | 21.2578 | 20.1635 | 21.2626 | 21.0233 | 21.2337 | |

**Table C2.** Mass measurements of $t_{bg} = 160\mu m$ trials.

| $V_r = 10mm/s$ | 1 | 2 | 3 | 4 | 5 | 6 | 7 | 8 | 9 | 10 | |
|---|---|---|---|---|---|---|---|---|---|---|---|
| $m_{cup}$ (g) | 15.6536 | 15.8456 | 15.7786 | 15.7823 | 15.7848 | 15.8637 | 15.8509 | 15.7617 | 15.7800 | 15.8325 | 15.7932 |
| $m_{cup + powder}$ (g) | 22.4842 | 22.4346 | 22.3122 | 22.1608 | 22.3142 | 22.4958 | 22.5541 | 22.6914 | 23.0659 | 22.5174 | |

| $V_r = 25mm/s$ | 1 | 2 | 3 | 4 | 5 | 6 | 7 | 8 | 9 | 10 | |
|---|---|---|---|---|---|---|---|---|---|---|---|
| $m_{cup}$ (g) | 15.7932 | 15.8293 | 15.7927 | 15.8277 | 15.7603 | 15.8304 | 15.7967 | 15.7769 | 15.8776 | 15.9116 | 15.8289 |
| $m_{cup + powder}$ (g) | 21.8198 | 22.4612 | 22.7205 | 22.4430 | 22.5825 | 22.8030 | 22.7956 | 22.6725 | 22.7673 | 23.1162 | |

| $V_r = 50mm/s$ | 1 | 2 | 3 | 4 | 5 | 6 | 7 | 8 | 9 | 10 | |
|---|---|---|---|---|---|---|---|---|---|---|---|
| $m_{cup}$ (g) | 15.8289 | 15.9092 | 15.8498 | 15.8629 | 15.8588 | 15.8832 | 15.8878 | 15.8742 | 15.8612 | 15.8910 | 15.8733 |
| $m_{cup + powder}$ (g) | 22.6307 | 22.2570 | 22.8516 | 22.6151 | 22.9377 | 22.6124 | 23.2434 | 22.7010 | 22.9870 | 23.0082 | |

| $V_r = 100mm/s$ | 1 | 2 | 3 | 4 | 5 | 6 | 7 | 8 | 9 | 10 | |
|---|---|---|---|---|---|---|---|---|---|---|---|
| $m_{cup}$ (g) | 15.8734 | 15.8653 | 15.9129 | 15.9183 | 15.8904 | 15.8905 | 15.8983 | 15.9191 | 15.9481 | 15.9741 | 15.9108 |
| $m_{cup + powder}$ (g) | 23.1692 | 22.8985 | 22.9797 | 22.7089 | 23.2423 | 22.7991 | 23.1286 | 22.5515 | 22.9072 | 23.1409 | |

| $V_r = 150mm/s$ | 1 | 2 | 3 | 4 | 5 | 6 | 7 | 8 | 9 | 10 | |
|---|---|---|---|---|---|---|---|---|---|---|---|
| $m_{cup}$ (g) | 15.9108 | 15.9364 | 15.9300 | 15.9175 | 15.9641 | 15.9861 | 15.9553 | 15.9727 | 15.9853 | 15.9916 | 15.9734 |
| $m_{cup + powder}$ (g) | 23.3661 | 22.8113 | 23.4637 | 22.8156 | 22.6660 | 23.0418 | 22.9961 | 23.1323 | 23.2713 | 23.2693 | |

**Table C3.** Mass measurements of $t_{bg} = 240\mu m$ trials.

| $V_r$ = 10mm/s | 1 | 2 | 3 | 4 | 5 | 6 | 7 | 8 | 9 | 10 | |
|---|---|---|---|---|---|---|---|---|---|---|---|
| $m_{cup}$ (g) | 15.7055 | 15.8706 | 15.8947 | 15.9358 | 15.9495 | 15.9635 | 15.9659 | 15.8788 | 15.8929 | 15.9343 | 15.9448 |
| $m_{cup + powder}$ (g) | 23.1887 | 23.9062 | 24.3192 | 24.4972 | 24.7216 | 24.5989 | 24.1320 | 24.7225 | 24.9867 | 24.7481 | |

| $V_r$ = 25mm/s | 1 | 2 | 3 | 4 | 5 | 6 | 7 | 8 | 9 | 10 | |
|---|---|---|---|---|---|---|---|---|---|---|---|
| $m_{cup}$ (g) | 15.9448 | 15.9445 | 16.9437 | 15.9148 | 15.9600 | 15.9994 | 15.9283 | 15.9552 | 15.9714 | 15.9794 | 15.9498 |
| $m_{cup + powder}$ (g) | 23.8546 | 24.2329 | 25.1794 | 24.9030 | 24.1214 | 25.3981 | 24.6413 | 25.7706 | 24.9933 | 25.1374 | |

| $V_r$ = 50mm/s | 1 | 2 | 3 | 4 | 5 | 6 | 7 | 8 | 9 | 10 | |
|---|---|---|---|---|---|---|---|---|---|---|---|
| $m_{cup}$ (g) | 15.9498 | 16.0199 | 15.9688 | 15.9602 | 15.9767 | 15.9834 | 15.9975 | 15.9818 | 15.9795 | 16.0267 | 16.0035 |
| $m_{cup + powder}$ (g) | 25.2082 | 25.0986 | 24.8541 | 24.2481 | 25.4769 | 24.7537 | 25.3353 | 24.0729 | 25.4632 | 24.7883 | |

| $V_r$ = 100mm/s | 1 | 2 | 3 | 4 | 5 | 6 | 7 | 8 | 9 | 10 | |
|---|---|---|---|---|---|---|---|---|---|---|---|
| $m_{cup}$ (g) | 16.0035 | 15.9908 | 15.9886 | 16.0030 | 16.0330 | 16.0014 | 16.0354 | 16.0062 | 16.0152 | 16.0052 | 16.0024 |
| $m_{cup + powder}$ (g) | 25.0935 | 25.0329 | 25.7151 | 25.2819 | 25.1289 | 25.4892 | 24.9997 | 24.9756 | 24.9313 | 25.0759 | |

| $V_r$ = 150mm/s | 1 | 2 | 3 | 4 | 5 | 6 | 7 | 8 | 9 | 10 | |
|---|---|---|---|---|---|---|---|---|---|---|---|
| $m_{cup}$ (g) | 16.0024 | 15.9907 | 15.9945 | 16.0096 | 15.9937 | 15.9970 | 16.0087 | 16.0123 | 16.0265 | 16.0322 | 16.0344 |
| $m_{cup + powder}$ (g) | 25.8225 | 25.2034 | 25.0880 | 25.0811 | 25.8359 | 24.9255 | 25.5023 | 24.8012 | 24.9328 | 24.8982 | |

**Table C4.** Mass measurements of $t_{bg} = 320\mu m$ trials.

| $V_r$ = 10mm/s | 1 | 2 | 3 | 4 | 5 | 6 | 7 | 8 | 9 | 10 | |
|---|---|---|---|---|---|---|---|---|---|---|---|
| $m_{cup}$ (g) | 15.7191 | 15.8487 | 15.8846 | 15.9086 | 15.9246 | 15.9529 | 15.9793 | 15.9915 | 15.9945 | 16.0177 | 15.9938 |
| $m_{cup + powder}$ (g) | 27.2185 | 27.1780 | 27.2904 | 27.1251 | 27.1866 | 27.3341 | 27.3017 | 27.1587 | 27.2794 | 27.0035 | |

| $V_r$ = 25mm/s | 1 | 2 | 3 | 4 | 5 | 6 | 7 | 8 | 9 | 10 | |
|---|---|---|---|---|---|---|---|---|---|---|---|
| $m_{cup}$ (g) | 15.9938 | 16.0108 | 16.0046 | 16.0212 | 16.0166 | 16.0469 | 16.0339 | 16.0133 | 16.0500 | 16.0159 | 16.0458 |
| $m_{cup + powder}$ (g) | 28.7786 | 27.9743 | 27.5224 | 28.1038 | 27.6049 | 28.7550 | 27.7824 | 28.0874 | 27.9379 | 28.0307 | |

| $V_r$ = 50mm/s | 1 | 2 | 3 | 4 | 5 | 6 | 7 | 8 | 9 | 10 | |
|---|---|---|---|---|---|---|---|---|---|---|---|
| $m_{cup}$ (g) | 16.0458 | 16.0447 | 16.0789 | 16.0335 | 16.0641 | 16.0393 | 16.0649 | 16.0447 | 16.0750 | 16.0704 | 16.0725 |
| $m_{cup + powder}$ (g) | 28.6970 | 28.5713 | 28.4914 | 28.4099 | 28.5419 | 27.6682 | 28.8431 | 29.2023 | 30.2405 | 30.2417 | |

| $V_r$ = 100mm/s | 1 | 2 | 3 | 4 | 5 | 6 | 7 | 8 | 9 | 10 | |
|---|---|---|---|---|---|---|---|---|---|---|---|
| $m_{cup}$ (g) | 16.0725 | 16.0537 | 16.0625 | 16.0544 | 16.0729 | 16.0904 | 16.0494 | 16.0607 | 16.0725 | 16.0714 | 16.1113 |
| $m_{cup + powder}$ (g) | 30.6917 | 28.5576 | 30.3428 | 30.1664 | 28.0013 | 30.0137 | 30.3945 | 25.4911 | 30.5173 | 28.5776 | |

| $V_r$ = 150mm/s | 1 | 2 | 3 | 4 | 5 | 6 | 7 | 8 | 9 | 10 | |
|---|---|---|---|---|---|---|---|---|---|---|---|
| $m_{cup}$ (g) | 16.1113 | 16.0960 | 16.0716 | 16.0765 | 16.1186 | 16.1069 | 16.0690 | 16.0941 | 16.1033 | 16.0995 | 16.0936 |
| $m_{cup + powder}$ (g) | 29.4948 | 29.1640 | 29.4571 | 29.5400 | 29.4160 | 29.1309 | 29.9042 | 29.5638 | 29.9494 | 29.0806 | |

Appendix D: ImageJ Ra Values

**Table D1.** ImageJ Ra Values for $t_{bg} = 80\mu m$ trials.

| $V_r$ | 1 | 2 | 3 | 4 | 5 | 6 | 7 | 8 | 9 | 10 | Average |
|---|---|---|---|---|---|---|---|---|---|---|---|
| 10 | 133.21 | 133.21 | 131.01 | 133.78 | 133.78 | 131.44 | 134.36 | 132.85 | 132.61 | 131.10 | 132.74 |
| 25 | 134.12 | 132.15 | 135.67 | 135.85 | 134.32 | 135.57 | 133.18 | 132.27 | 133.32 | 135.07 | 134.15 |
| 50 | 136.14 | 134.55 | 136.42 | 134.92 | 136.18 | 138.75 | 136.59 | 132.30 | 133.57 | 136.24 | 135.57 |
| 100 | 134.55 | 138.28 | 137.08 | 138.48 | 137.68 | 135.43 | 138.12 | 137.22 | 137.44 | 137.60 | 137.19 |
| 150 | 137.24 | 136.89 | 137.73 | 137.82 | 139.69 | 137.92 | 139.26 | 137.16 | 137.31 | 139.32 | 138.04 |

**Table D2.** ImageJ Ra Values for $t_{bg} = 160\mu m$ trials.

| $V_r$ | 1 | 2 | 3 | 4 | 5 | 6 | 7 | 8 | 9 | 10 | Average |
|---|---|---|---|---|---|---|---|---|---|---|---|
| 10 | 131.13 | 131.24 | 129.60 | 129.18 | 131.35 | 132.44 | 130.61 | 129.23 | 129.31 | 131.35 | 130.54 |
| 25 | 129.73 | 133.99 | 132.65 | 130.65 | 131.96 | 129.49 | 132.61 | 133.58 | 130.71 | 132.29 | 131.77 |
| 50 | 132.79 | 133.56 | 132.95 | 131.75 | 133.28 | 131.98 | 133.88 | 134.37 | 131.56 | 133.00 | 132.91 |
| 100 | 132.59 | 133.95 | 135.09 | 135.86 | 136.71 | 134.39 | 132.52 | 134.45 | 136.87 | 135.76 | 134.82 |
| 150 | 137.39 | 136.74 | 134.93 | 134.70 | 135.00 | 134.04 | 136.69 | 134.98 | 137.88 | 135.05 | 135.74 |

**Table D3.** ImageJ Ra Values for $t_{bg} = 240\mu m$ trials.

| $V_r$ | 1 | 2 | 3 | 4 | 5 | 6 | 7 | 8 | 9 | 10 | Average |
|---|---|---|---|---|---|---|---|---|---|---|---|
| 10 | 126.37 | 128.76 | 129.25 | 127.24 | 131.06 | 127.02 | 127.14 | 128.62 | 131.15 | 128.37 | 128.50 |
| 25 | 128.14 | 127.70 | 127.72 | 128.76 | 131.91 | 132.67 | 133.56 | 128.73 | 126.27 | 131.04 | 129.65 |
| 50 | 127.77 | 132.32 | 132.95 | 131.04 | 133.36 | 135.59 | 132.56 | 126.77 | 127.11 | 132.25 | 131.17 |
| 100 | 132.21 | 133.38 | 130.61 | 134.32 | 132.58 | 135.45 | 131.39 | 129.15 | 134.23 | 134.58 | 132.79 |
| 150 | 131.84 | 133.32 | 135.44 | 132.64 | 134.92 | 131.60 | 136.35 | 135.88 | 136.28 | 133.38 | 134.16 |

**Table D4.** ImageJ Ra Values for $t_{bg} = 320\mu m$ trials.

| $V_r$ | 1 | 2 | 3 | 4 | 5 | 6 | 7 | 8 | 9 | 10 | Average |
|---|---|---|---|---|---|---|---|---|---|---|---|
| 10 | 126.08 | 130.61 | 129.97 | 124.50 | 125.10 | 128.19 | 131.78 | 127.64 | 128.20 | 131.90 | 128.40 |
| 25 | 133.00 | 131.58 | 127.78 | 131.76 | 128.67 | 132.43 | 128.42 | 126.69 | 130.15 | 130.84 | 130.13 |
| 50 | 129.38 | 133.22 | 130.57 | 133.43 | 134.31 | 129.72 | 131.61 | 132.79 | 134.27 | 133.06 | 132.24 |
| 100 | 130.79 | 132.22 | 137.92 | 135.72 | 131.59 | 134.42 | 137.79 | 132.33 | 136.19 | 134.25 | 134.32 |
| 150 | 135.54 | 134.78 | 137.02 | 132.86 | 135.35 | 136.13 | 135.93 | 136.35 | 137.06 | 132.48 | 135.35 |
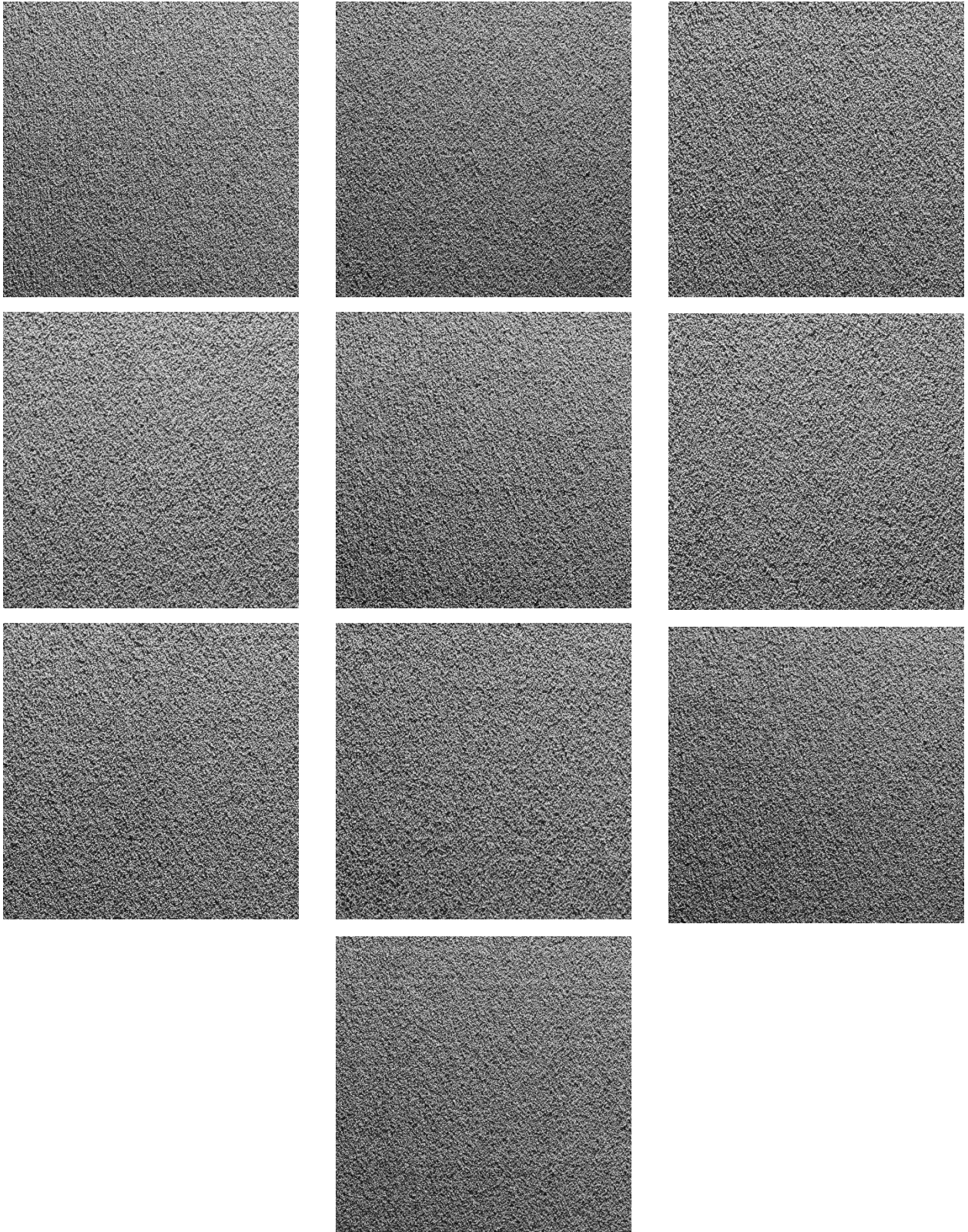
**Figure D1.** Pictures of $t_{bg} = 80\mu\text{m}$ $V_r = 10\text{mm/s}$ trial.
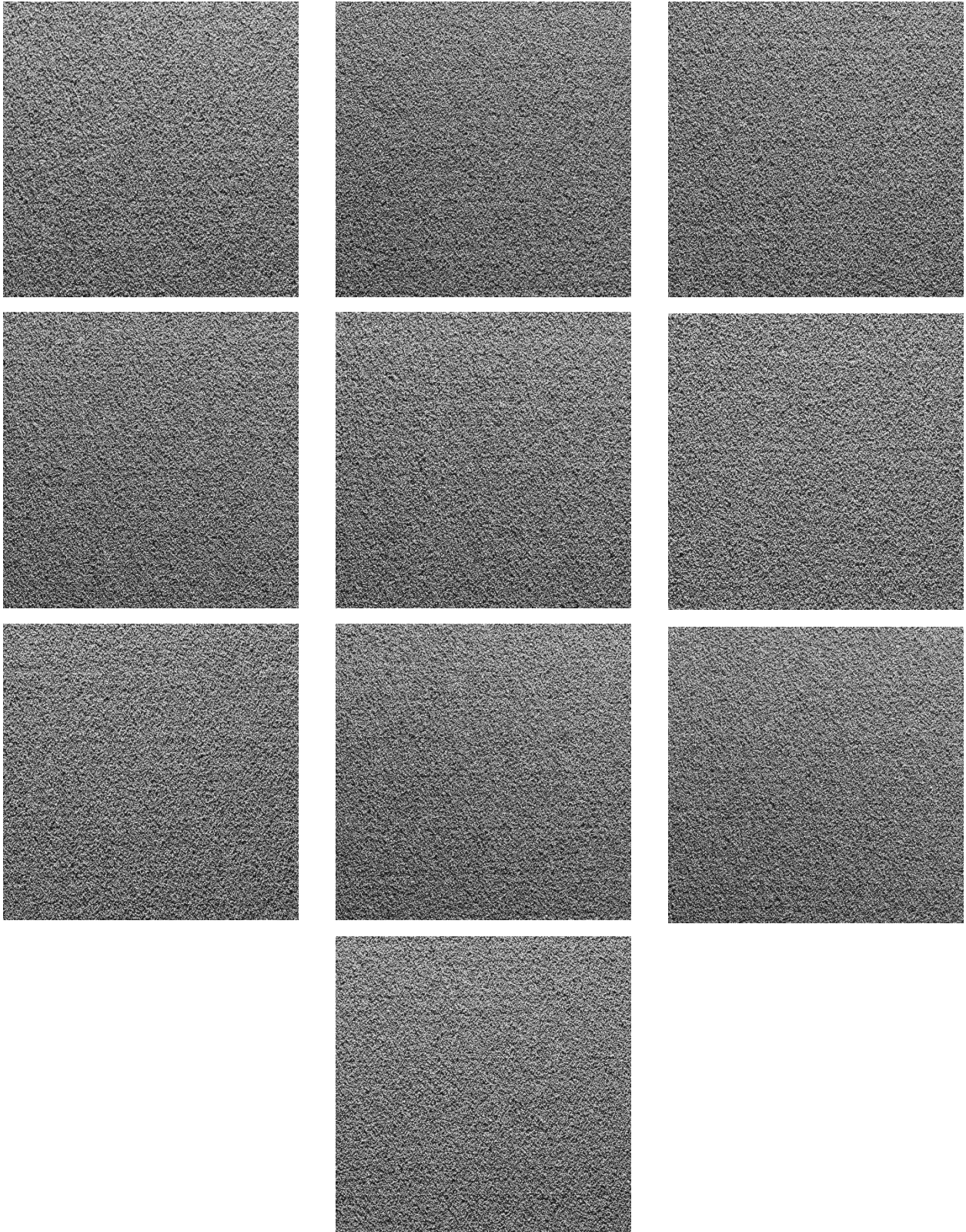
**Figure D2.** Pictures of $t_{bg} = 80\mu m$ $V_r = 25mm/s$ trial.

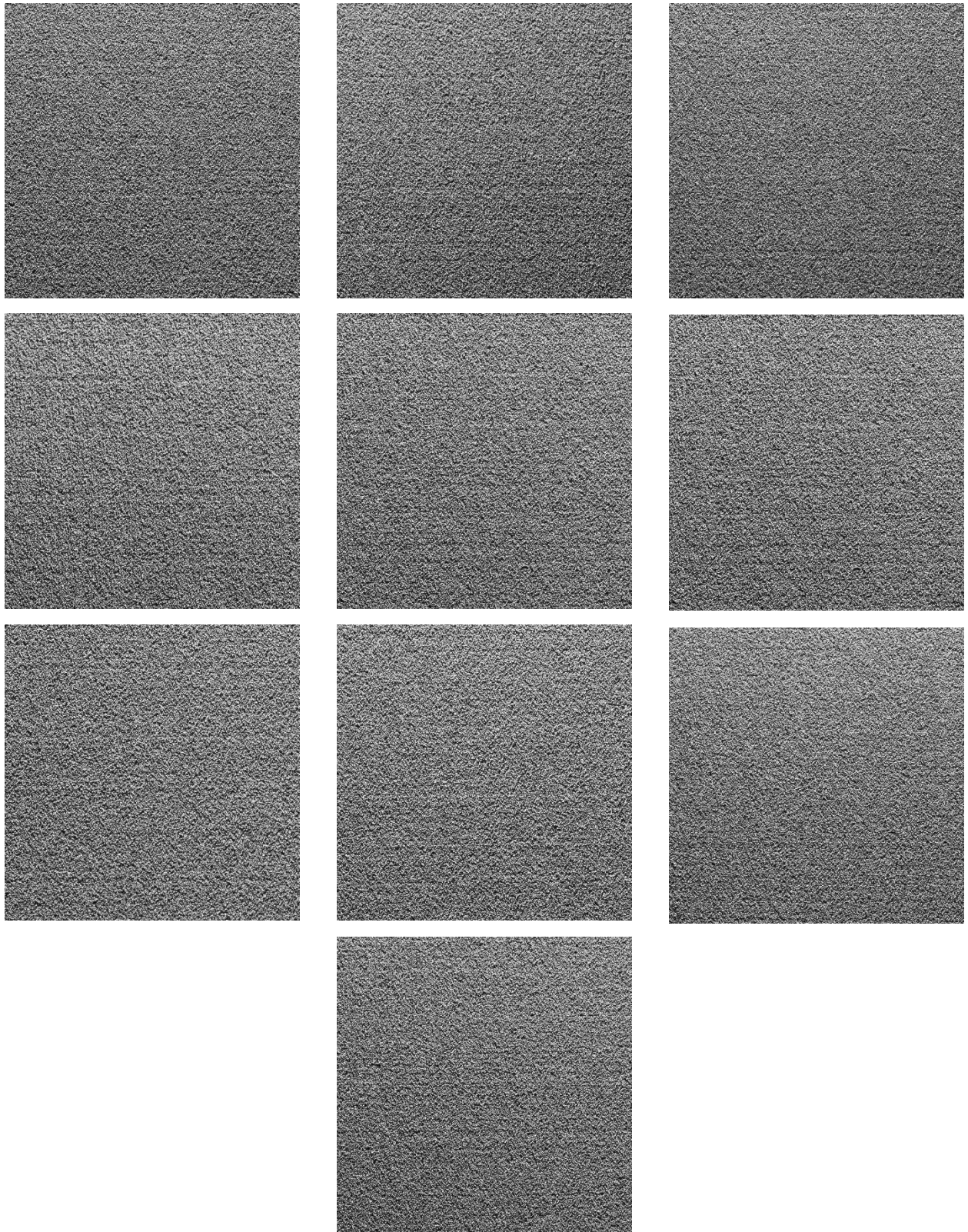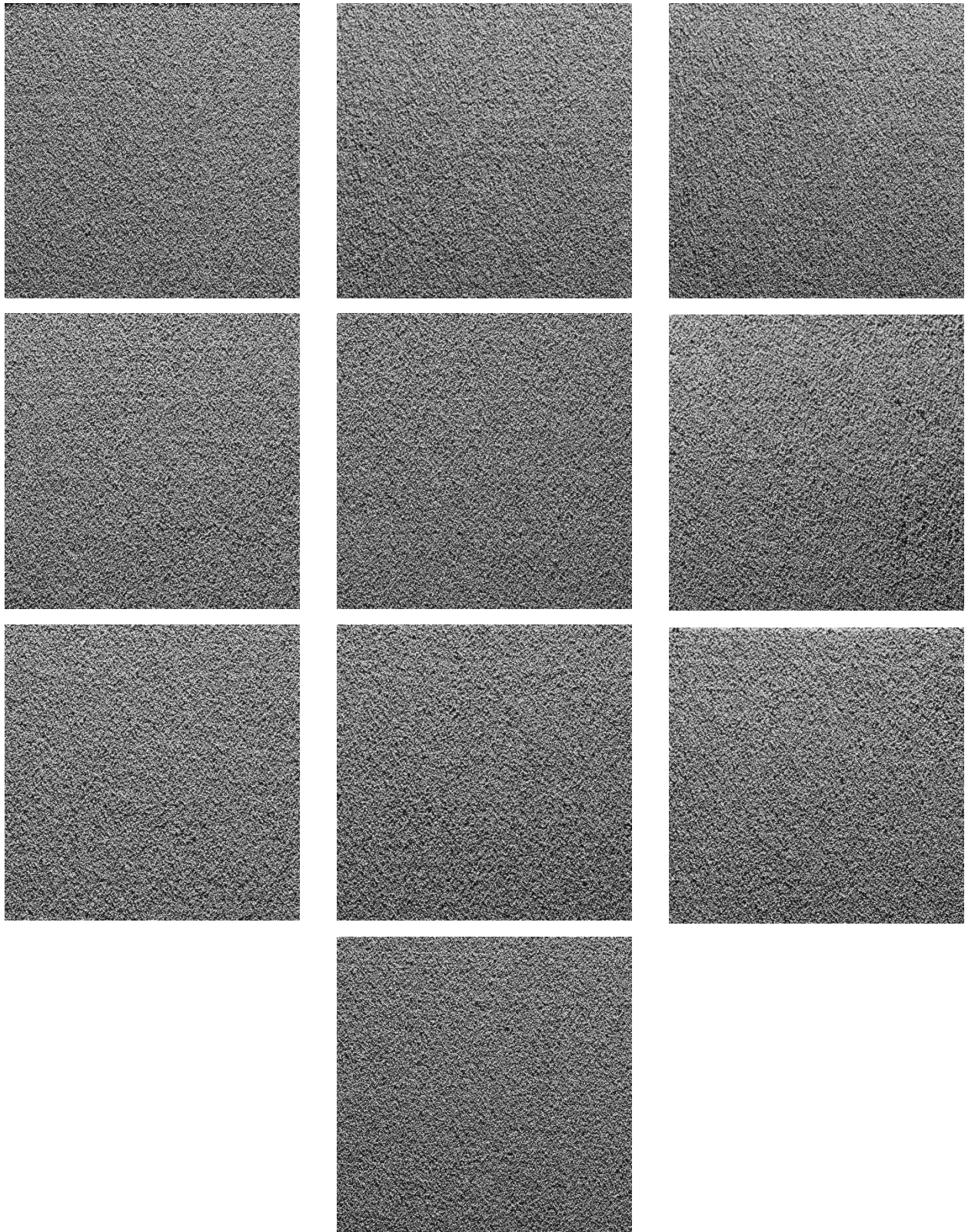**Figure D3.** Pictures of $t_{bg} = 80\mu m$ $V_r = 50mm/s$ trial.

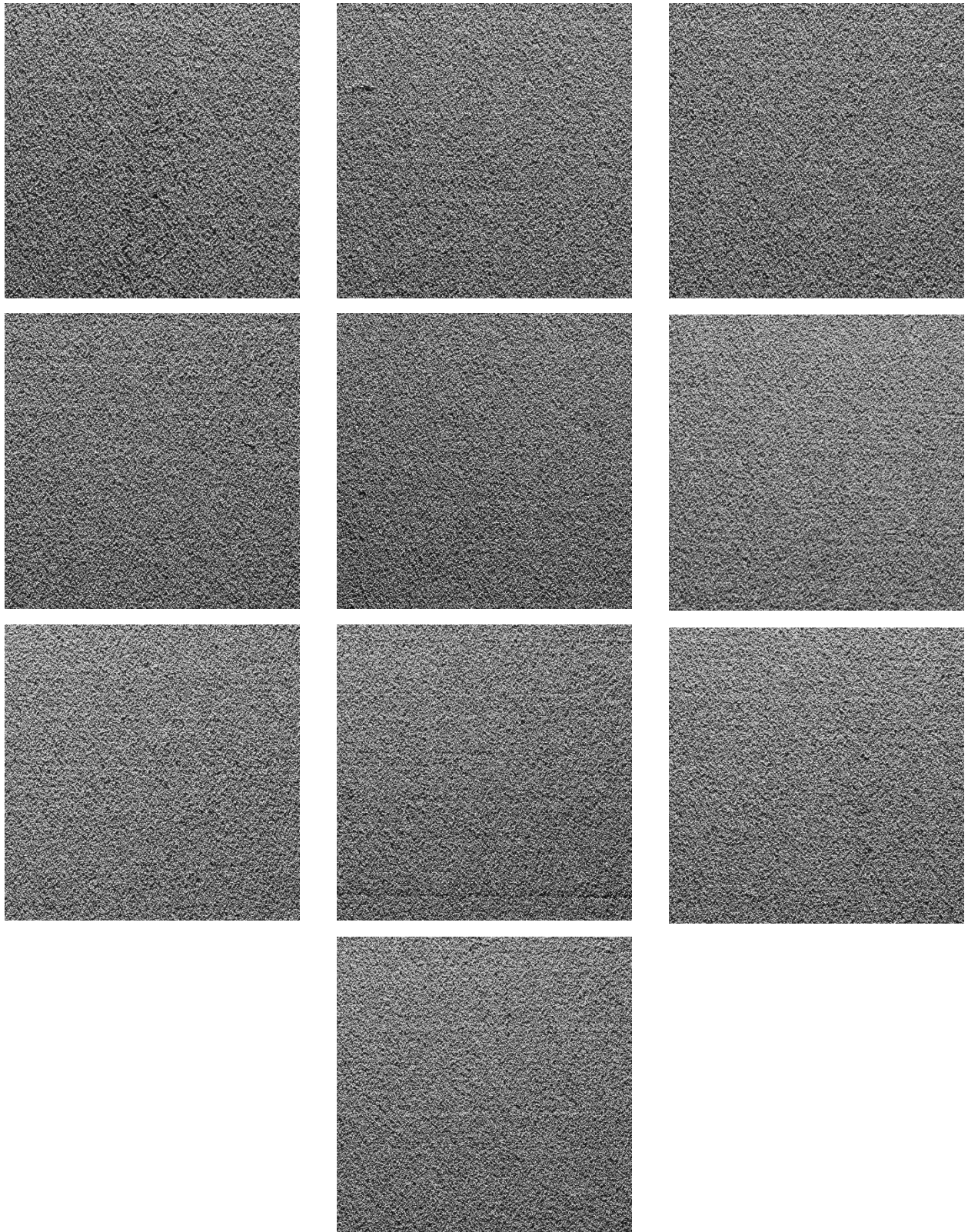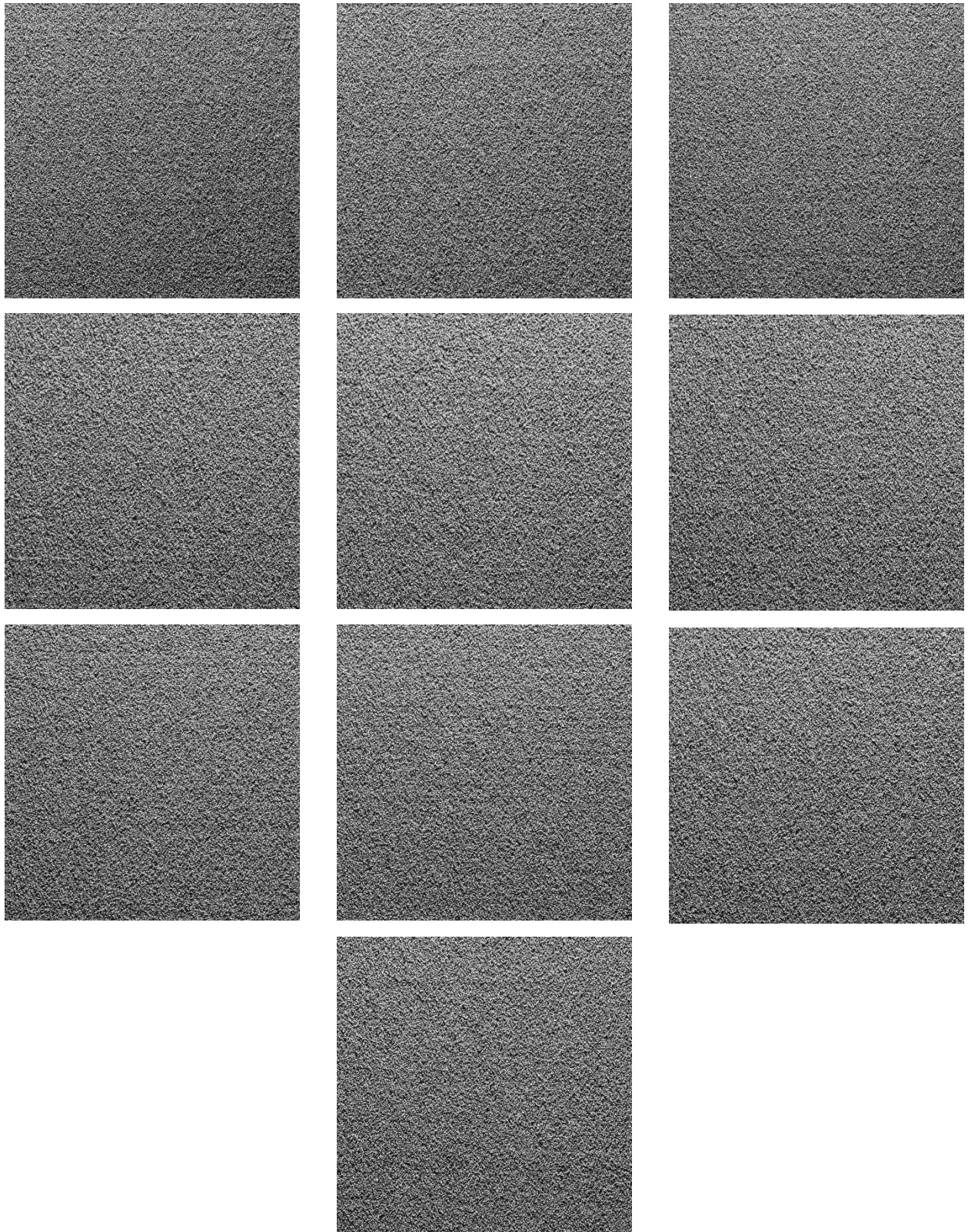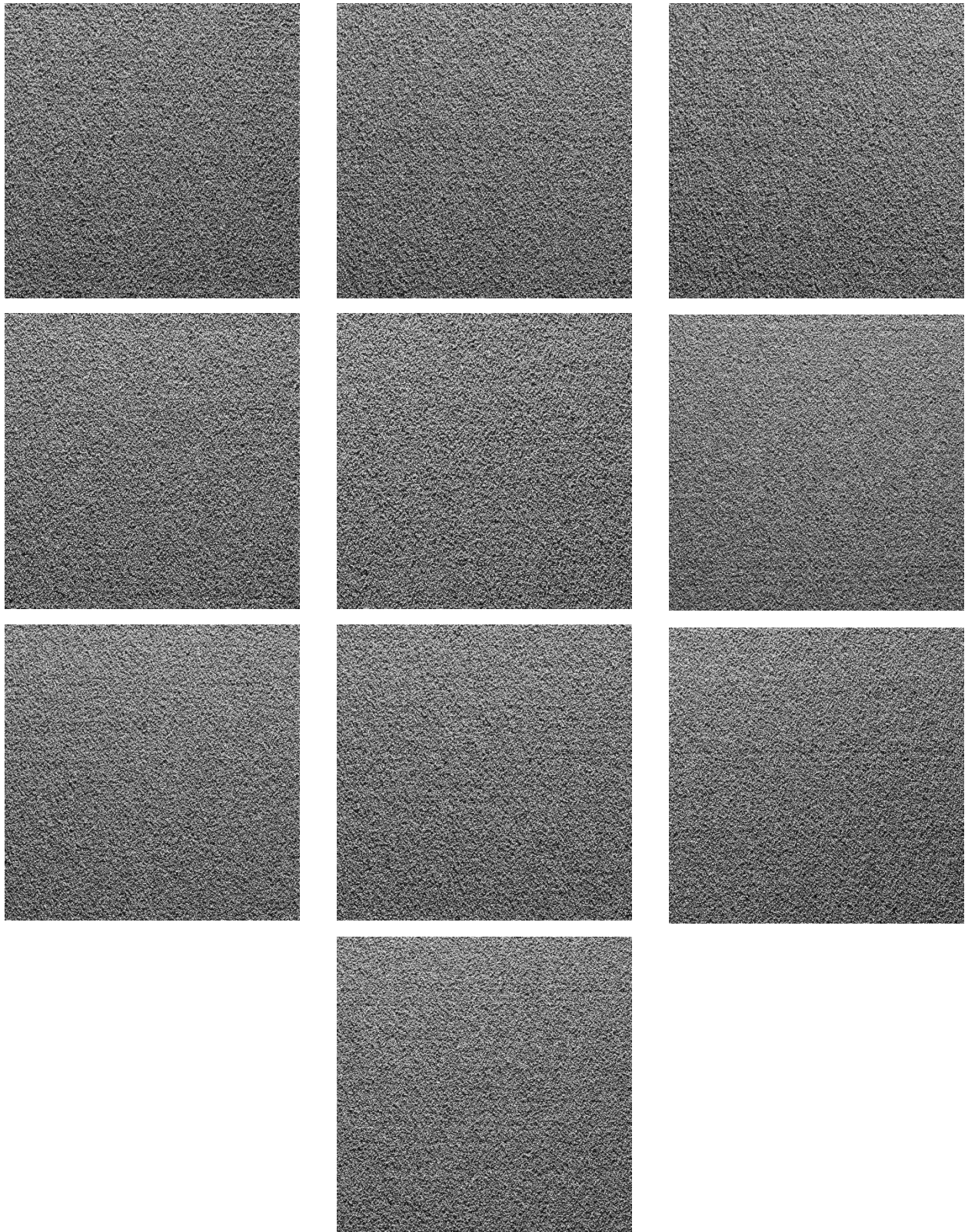**Figure D4.** Pictures of $t_{bg} = 80$µm $V_r = 100$mm/s trial.

**Figure D5.** Pictures of $t_{bg} = 80\mu m$ $V_r = 150$mm/s trial.

**Figure D6.** Pictures of $t_{bg} = 160\mu\text{m}$ $V_r = 10\text{mm/s}$ trial.

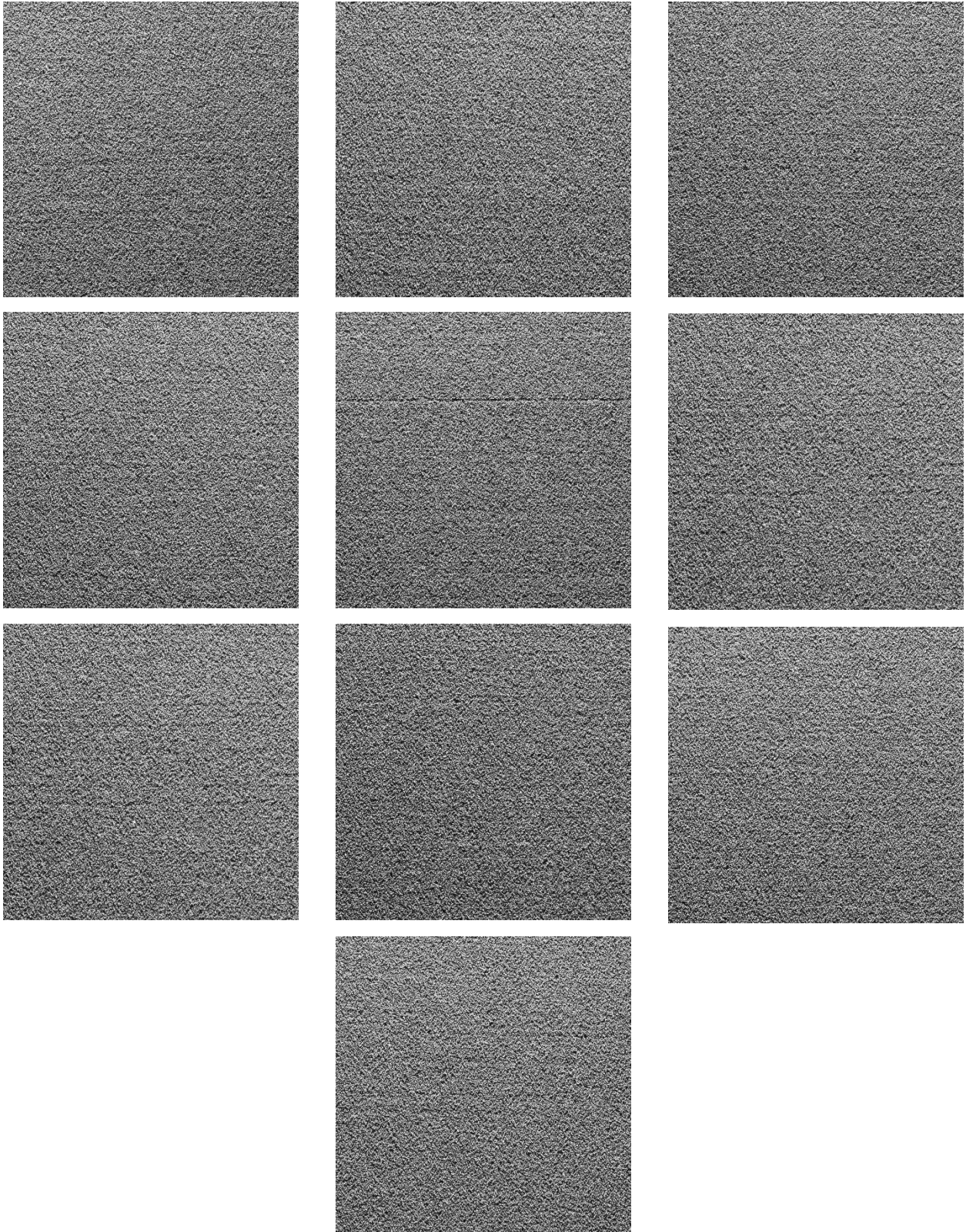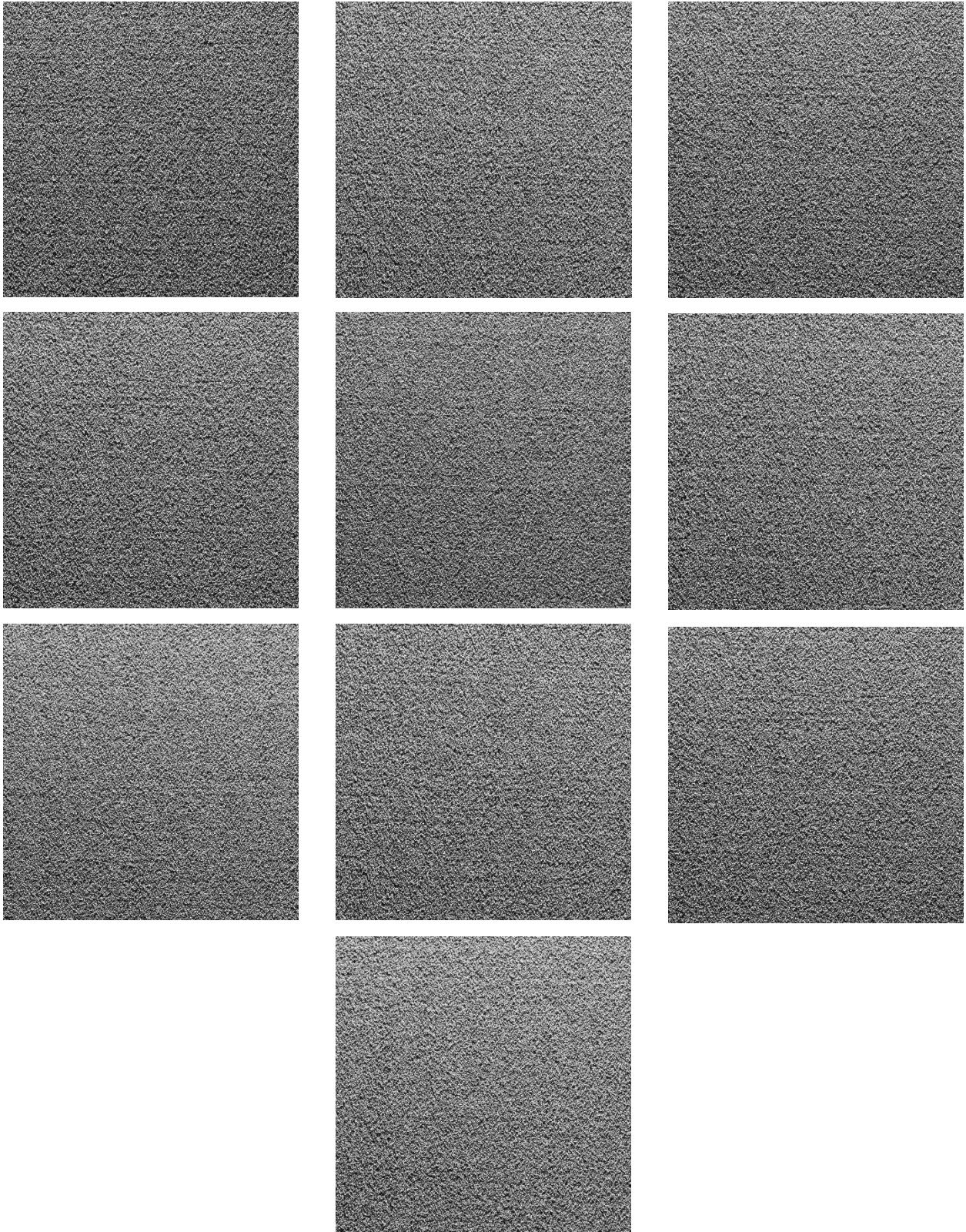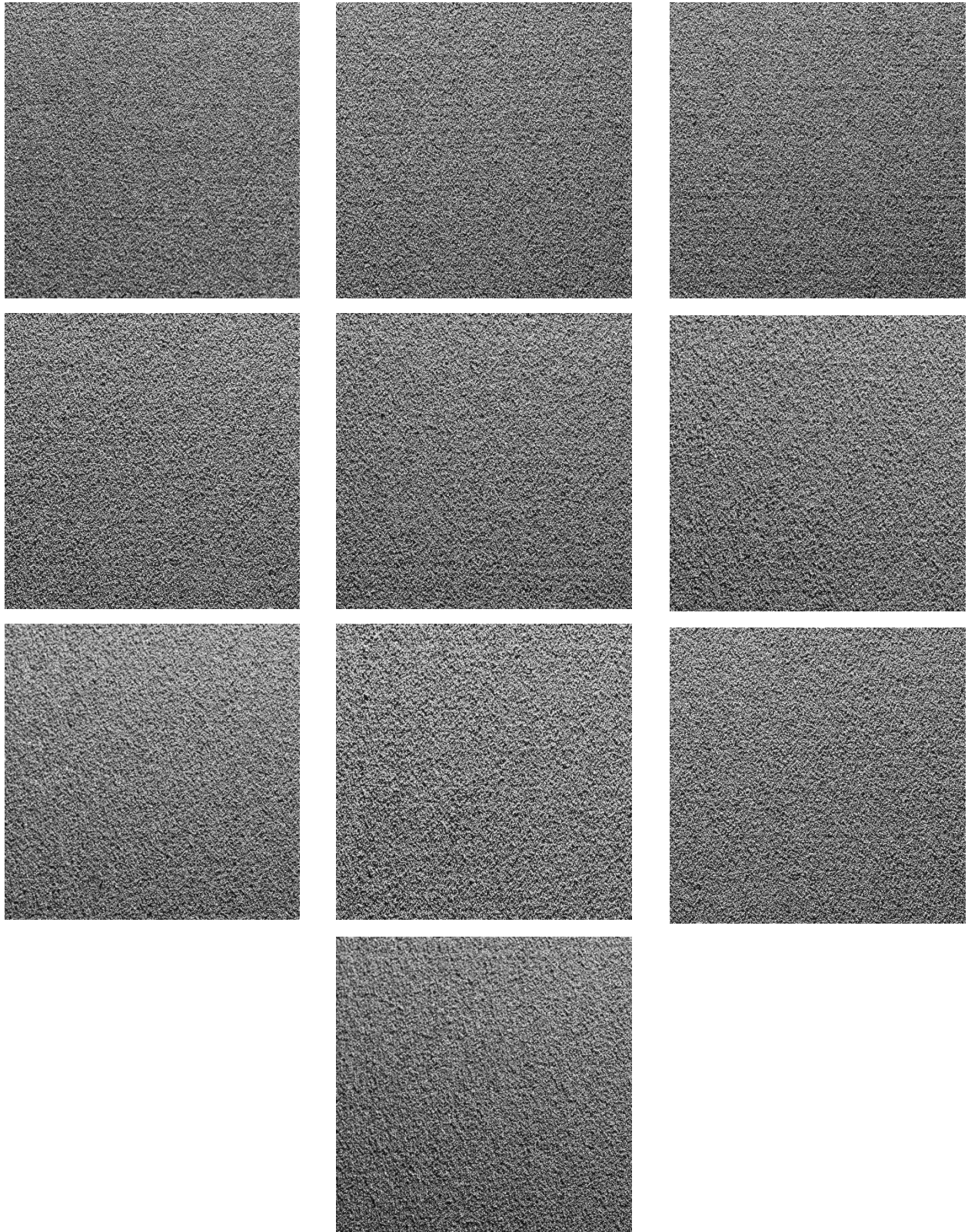**Figure D7.** Pictures of $t_{bg} = 160\mu\text{m}$ $V_r = 25\text{mm/s}$ trial.

**Figure D8.** Pictures of $t_{bg} = 160\mu m$ $V_r = 50mm/s$ trial.

**Figure D9.** Pictures of $t_{bg} = 160\mu m$ $V_r = 100mm/s$ trial.

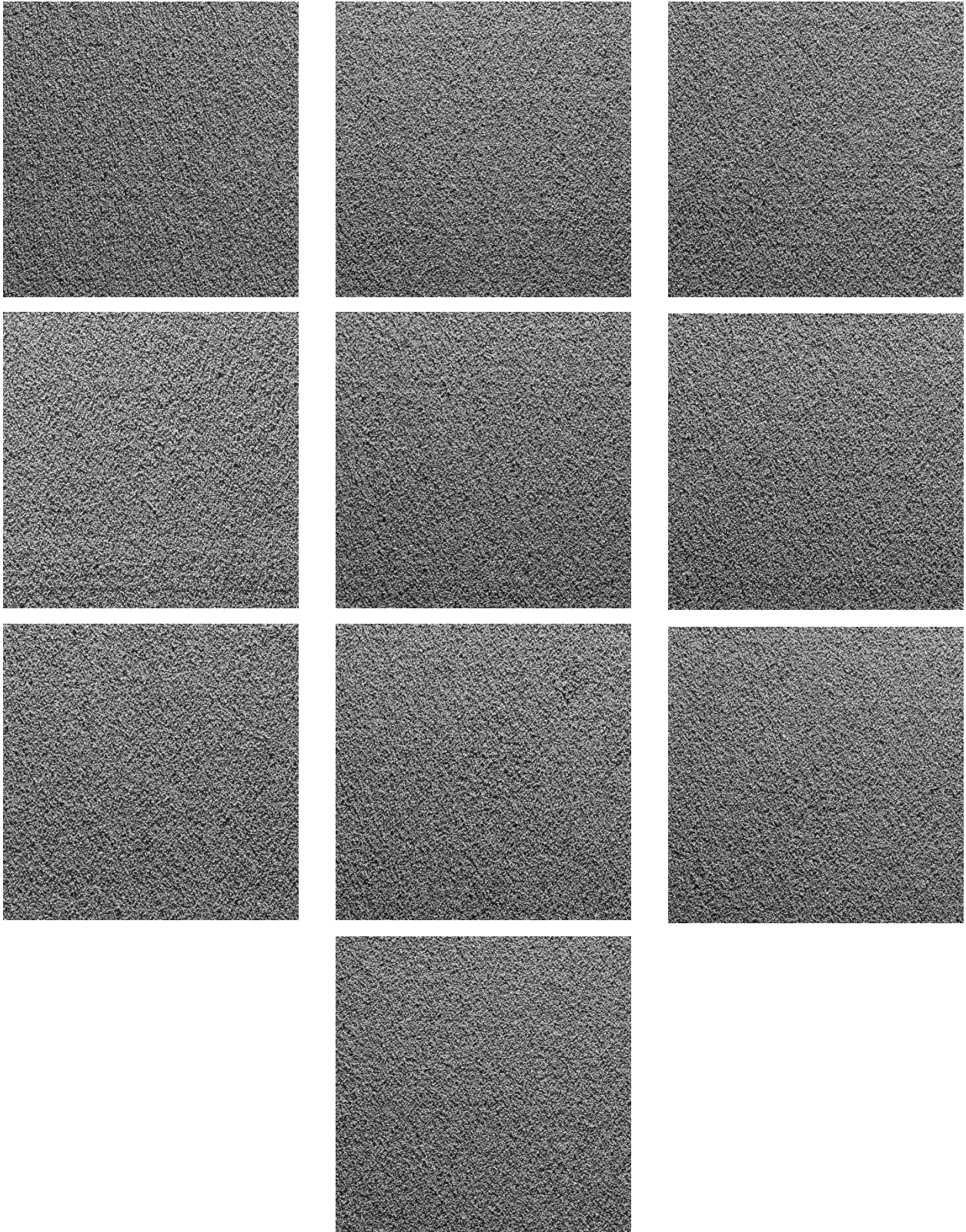**Figure D10.** Pictures of $t_{bg} = 160\mu m$ $V_r = 150$mm/s trial.

**Figure D11.** Pictures of $t_{bg} = 240$µm $V_r = 10$mm/s trial.

**Figure D12.** Pictures of $t_{bg} = 240\mu m$ $V_r = 25$mm/s trial.

**Figure D13.** Pictures of $t_{bg} = 240\mu m$ $V_r = 50mm/s$ trial.

**Figure D14.** Pictures of $t_{bg} = 240\mu m$ $V_r = 100$mm/s trial.

**Figure D15.** Pictures of $t_{bg} = 240\mu m$ $V_r = 150$mm/s trial.

**Figure D16.** Pictures of $t_{bg} = 320\mu m$ $V_r = 10mm/s$ trial.

**Figure D17.** Pictures of $t_{bg} = 320\mu m$ $V_r = 25mm/s$ trial.

**Figure D18.** Pictures of $t_{bg} = 320\mu$m $V_r = 50$mm/s trial.

**Figure D19.** Pictures of $t_{bg} = 320\mu\text{m}$ $V_r = 100\text{mm/s}$ trial.

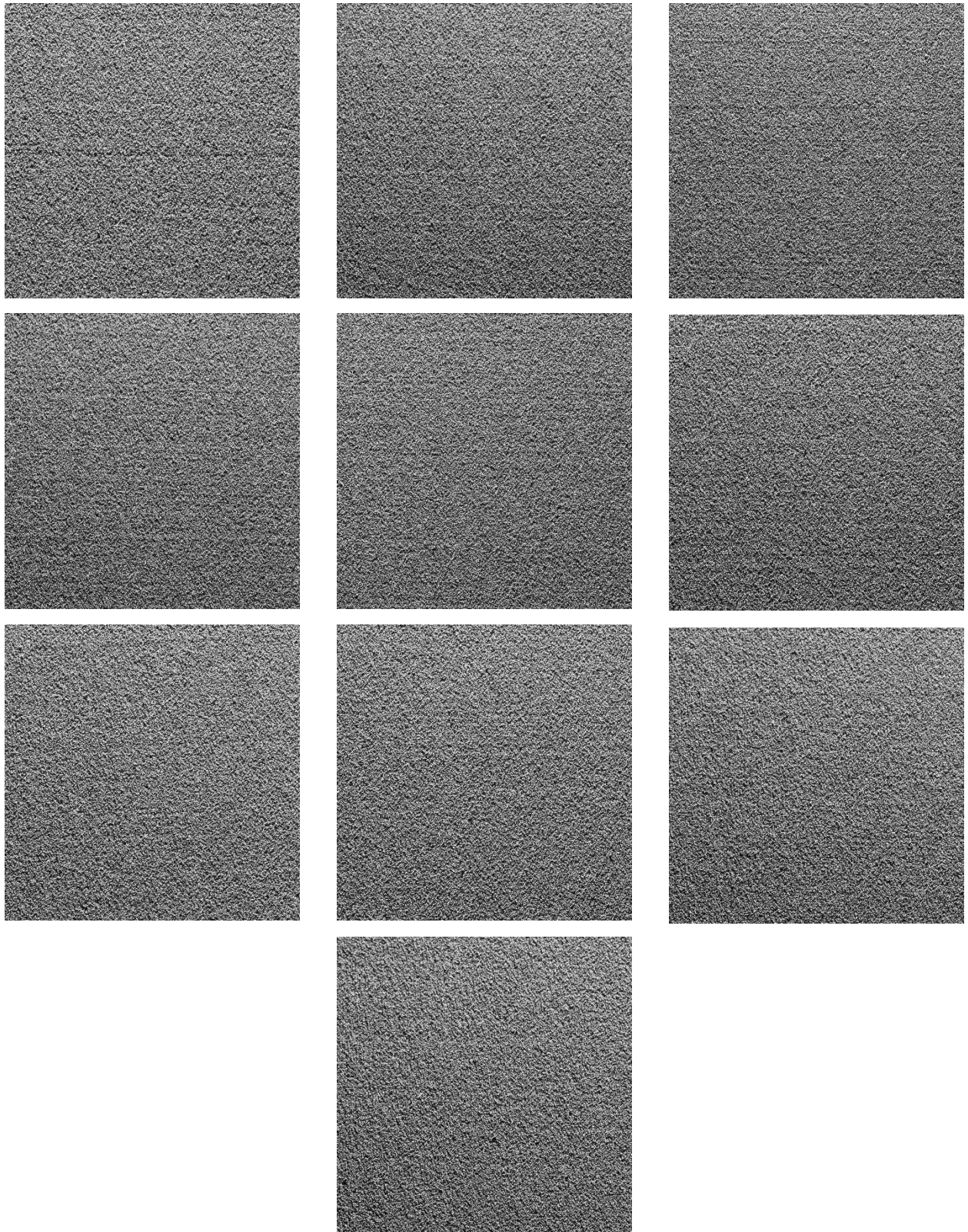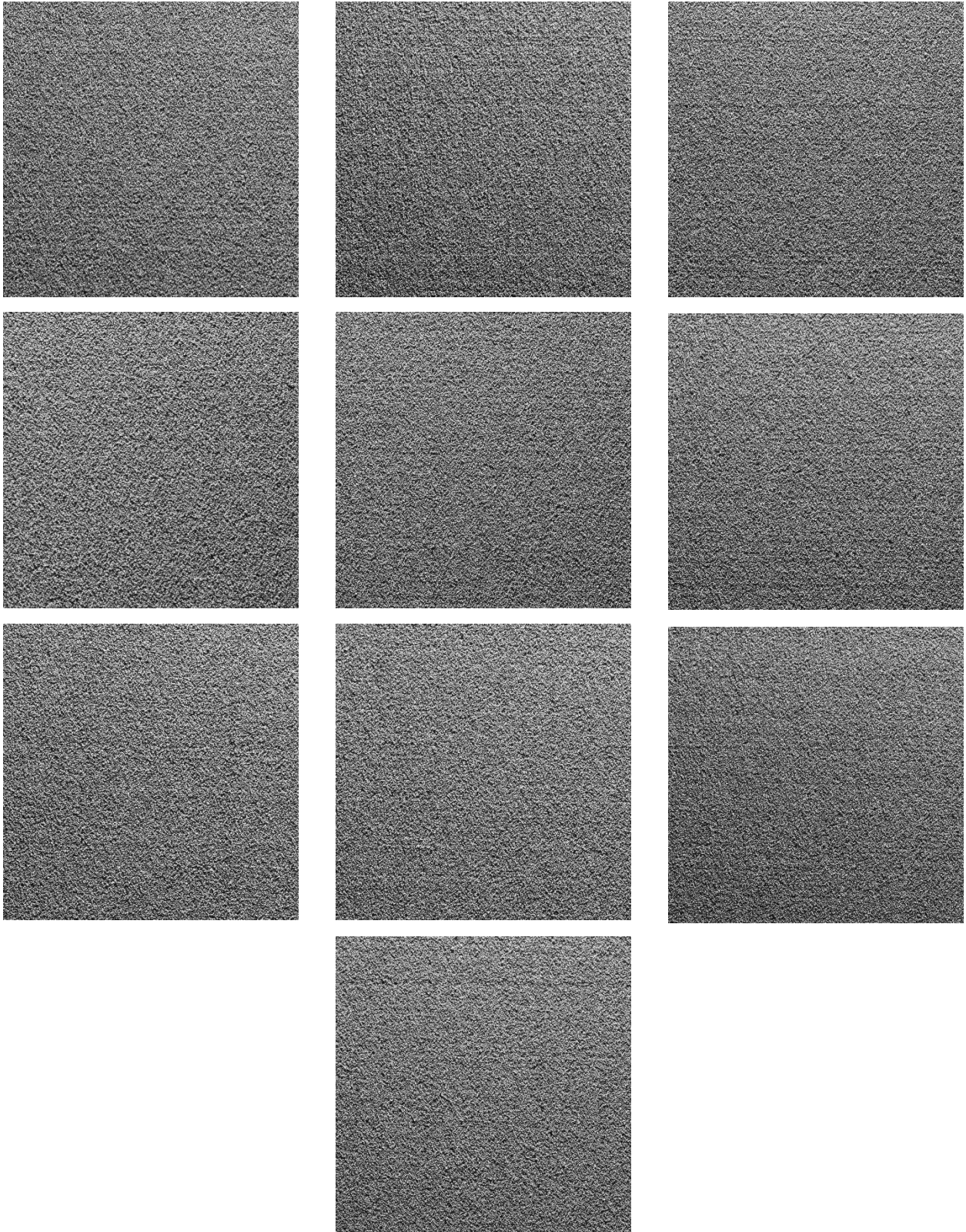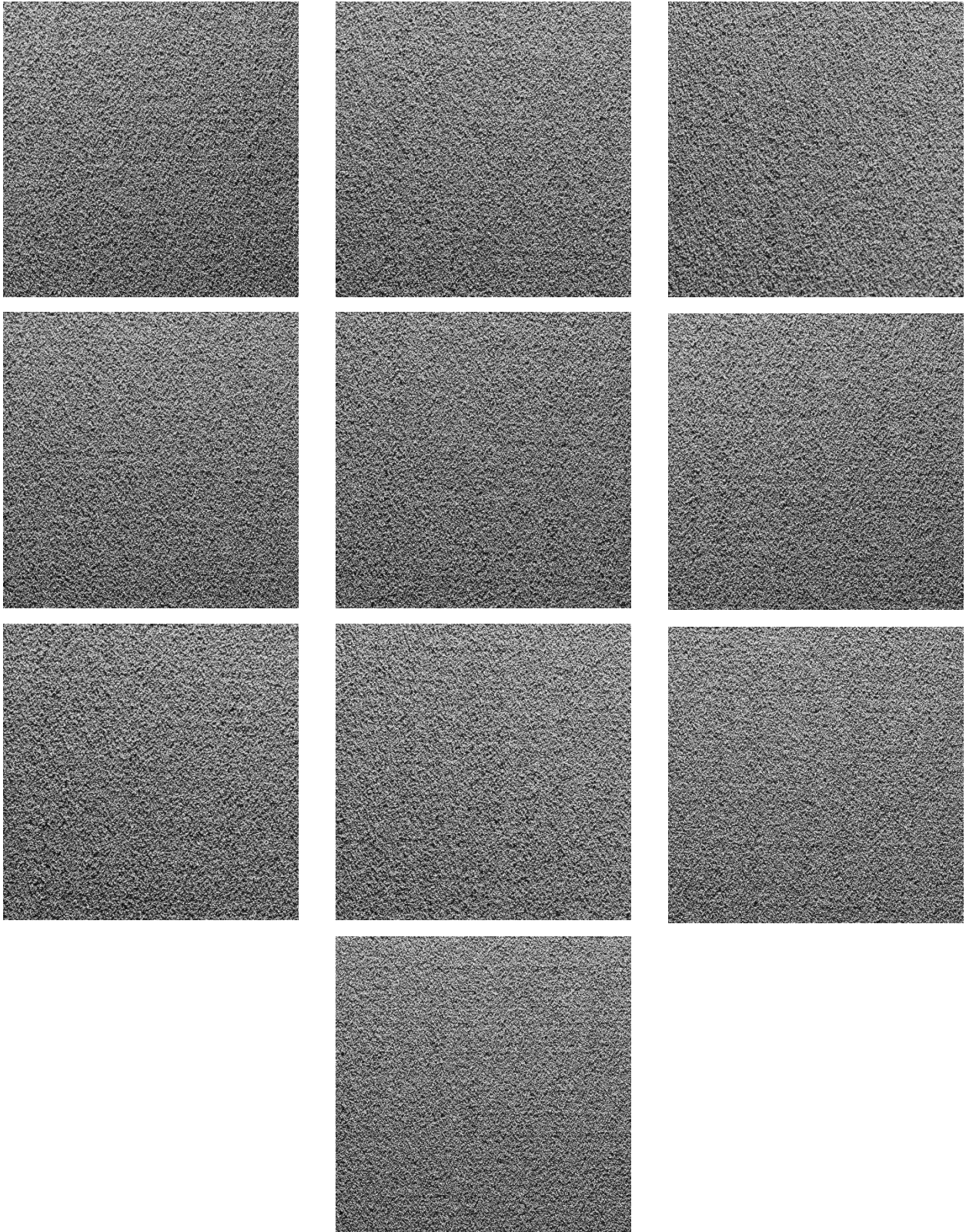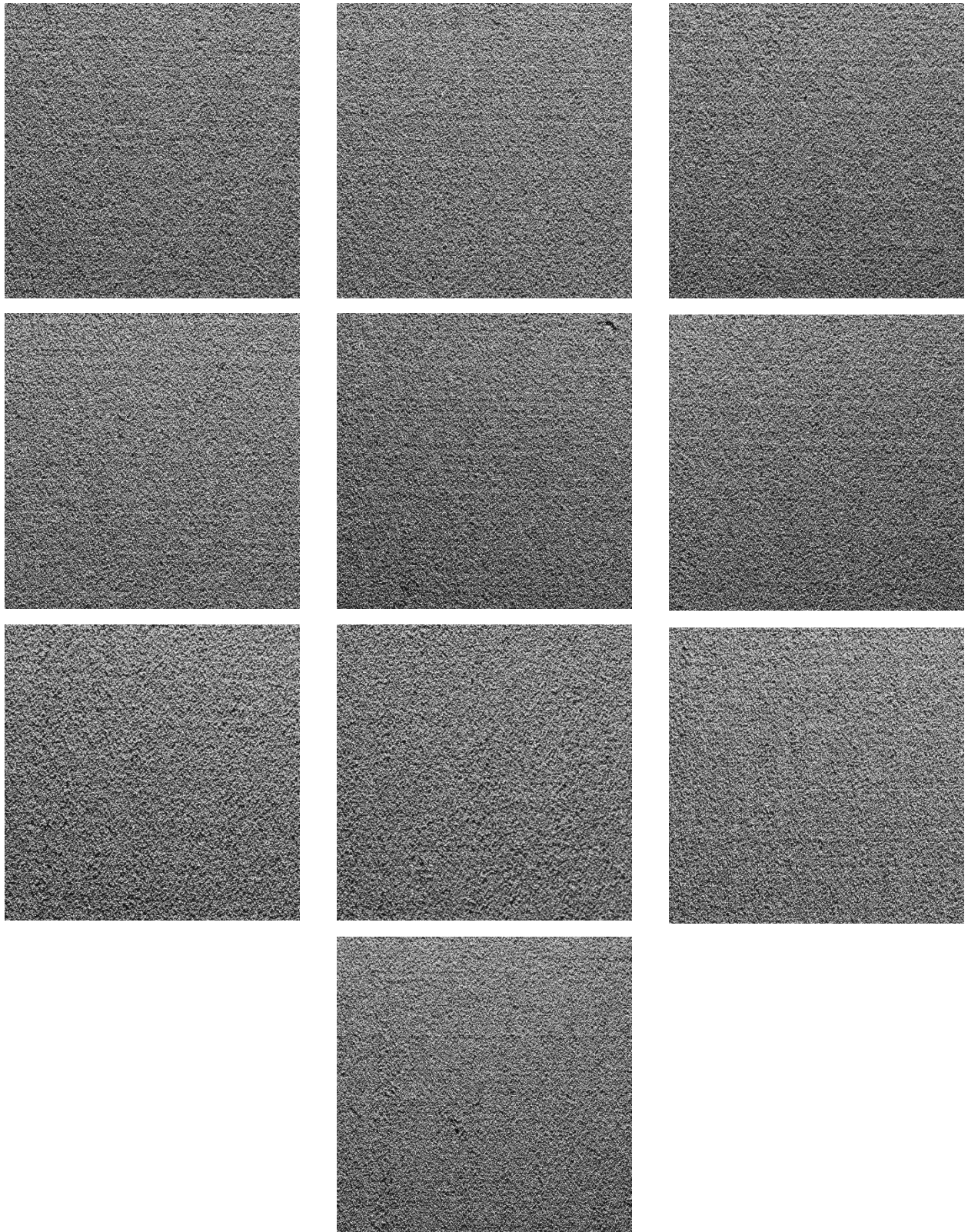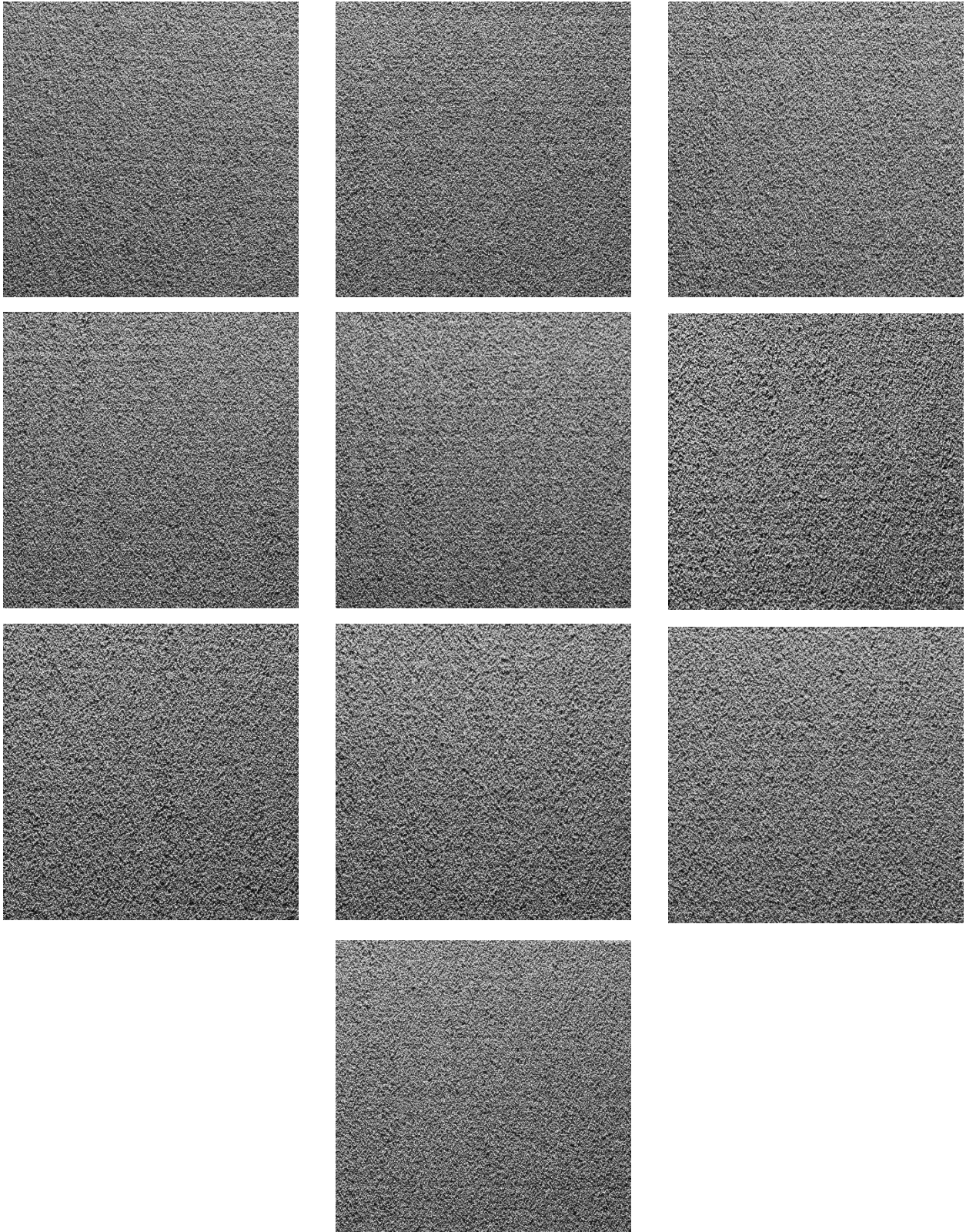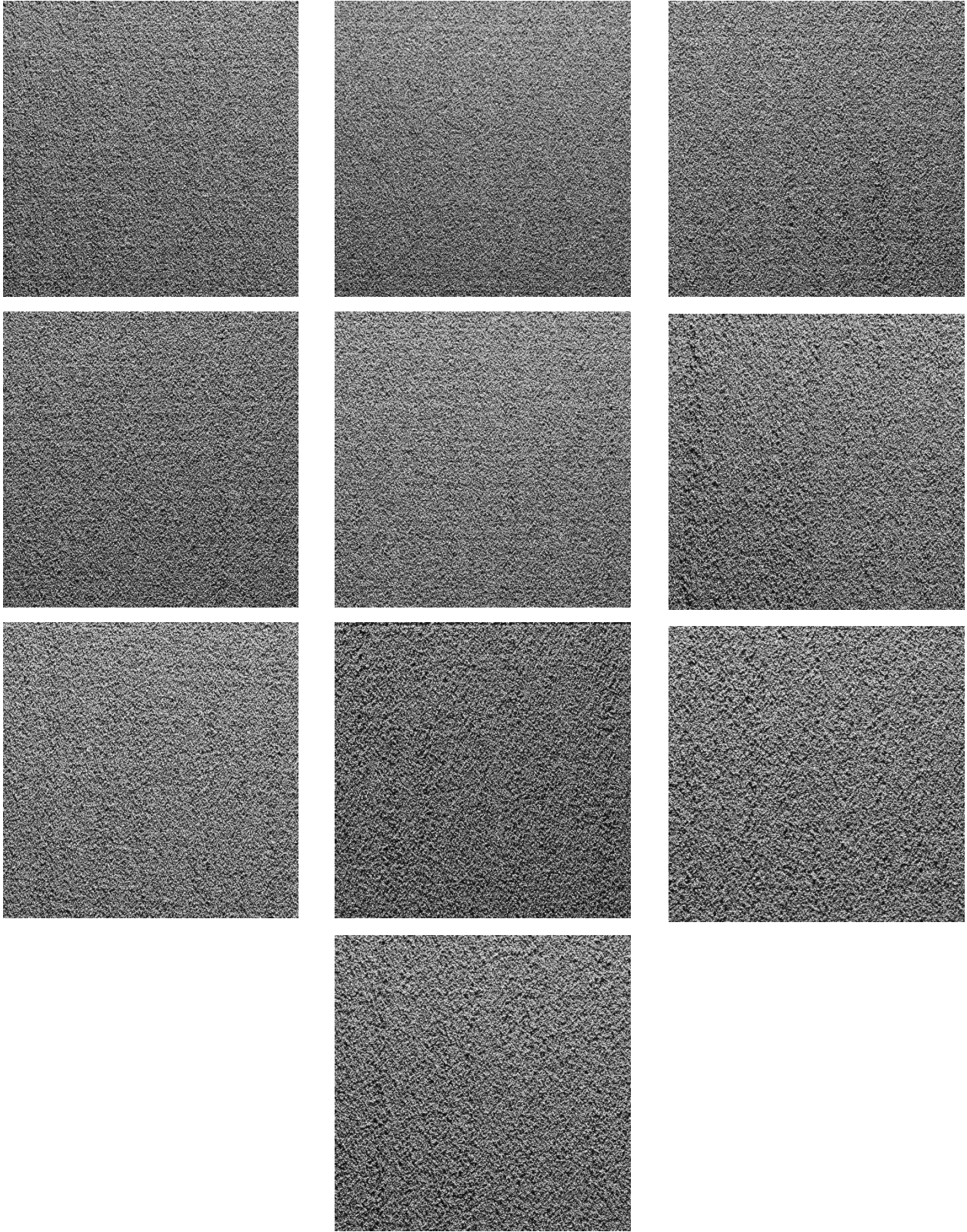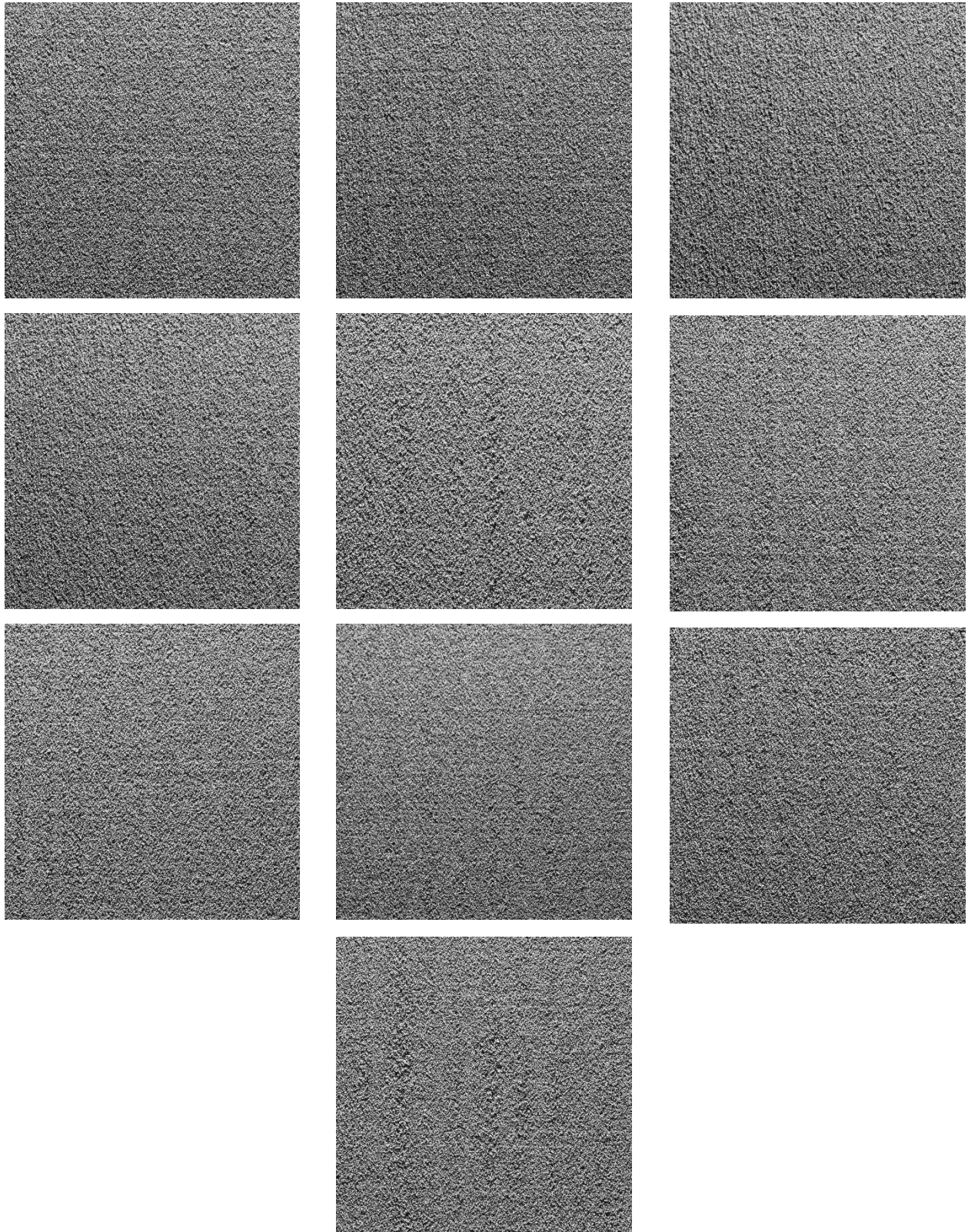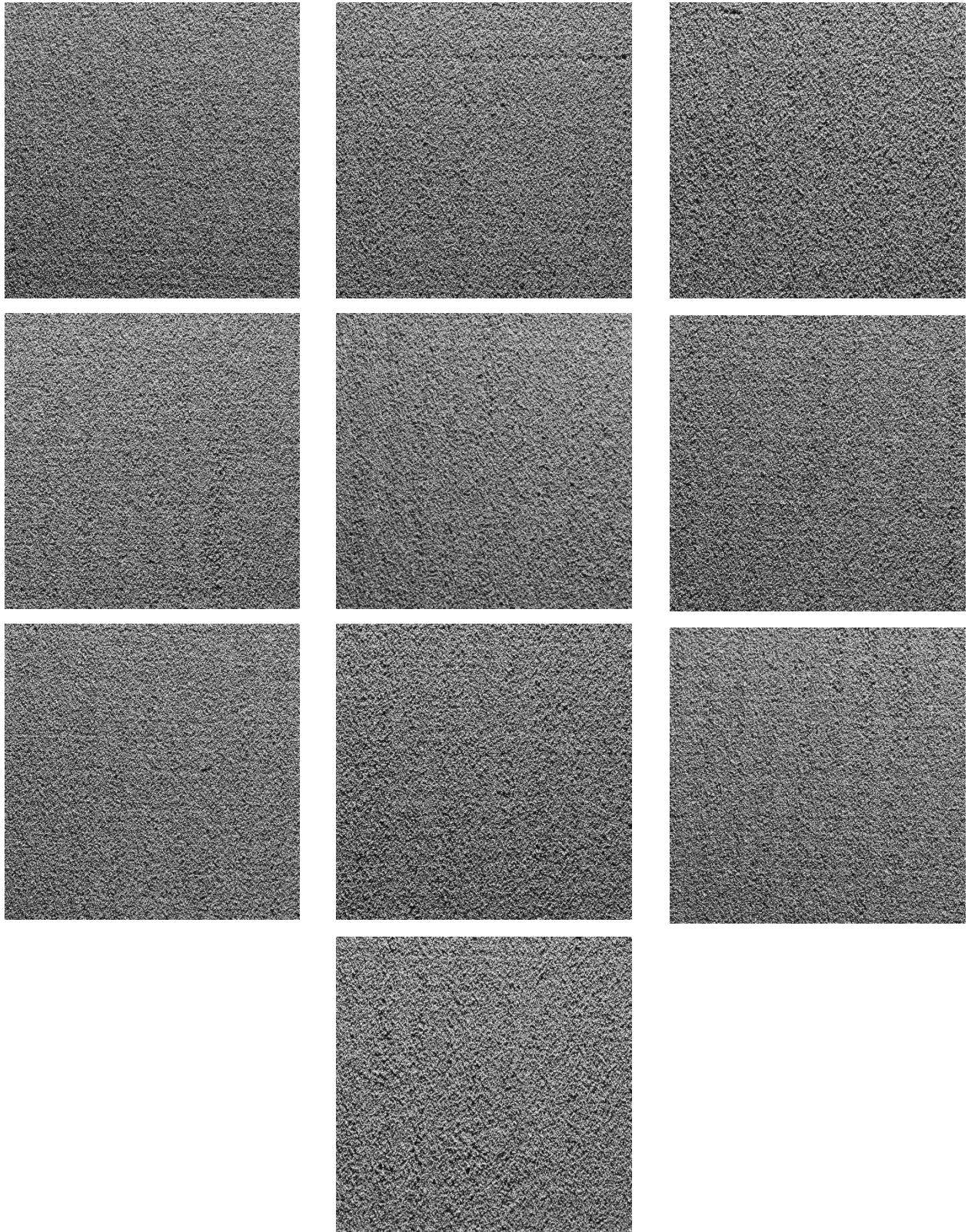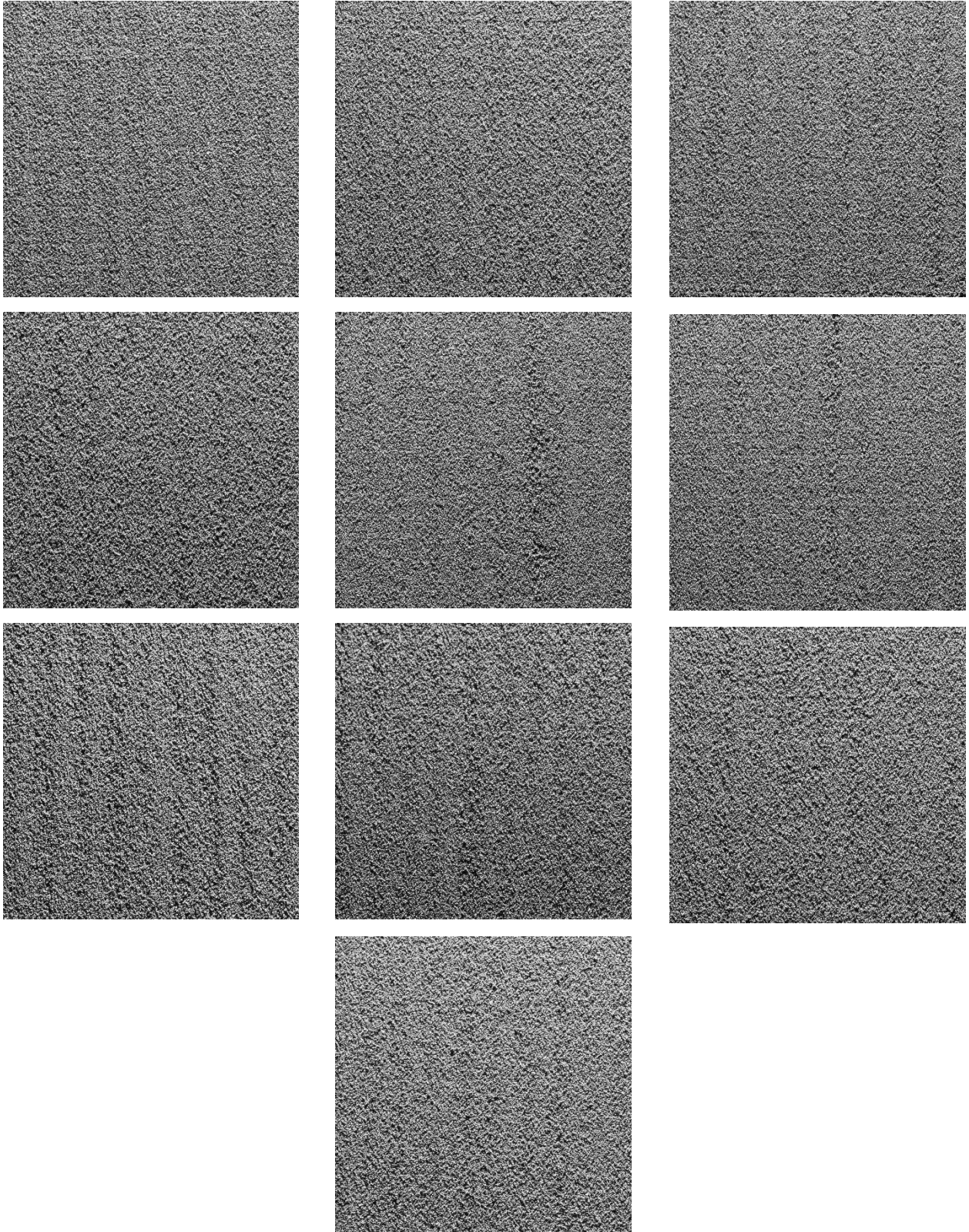**Figure D20.** Pictures of $t_{bg} = 320\mu m$ $V_r = 150$mm/s trial.

**Table E1.** ImageJ values of $t_{bg} = 80\mu m$ trials.

| $V_r$ | 1 | 2 | 3 | 4 | 5 | 6 | 7 | 8 | 9 | 10 | Average |
|---|---|---|---|---|---|---|---|---|---|---|---|
| 10 | 133.21 | 133.21 | 131.01 | 133.78 | 133.78 | 131.44 | 134.36 | 132.85 | 132.61 | 131.10 | 132.74 |
| 25 | 134.12 | 132.15 | 135.67 | 135.85 | 134.32 | 135.57 | 133.18 | 132.27 | 133.32 | 135.07 | 134.15 |
| 50 | 136.14 | 134.55 | 136.42 | 134.92 | 136.18 | 138.75 | 136.59 | 132.30 | 133.57 | 136.24 | 135.57 |
| 100 | 134.55 | 138.28 | 137.08 | 138.48 | 137.68 | 135.43 | 138.12 | 137.22 | 137.44 | 137.60 | 137.19 |
| 150 | 137.24 | 136.89 | 137.73 | 137.82 | 139.69 | 137.92 | 139.26 | 137.16 | 137.31 | 139.32 | 138.04 |

**Table E2.** ImageJ values of $t_{bg} = 160\mu m$ trials.

| $V_r$ | 1 | 2 | 3 | 4 | 5 | 6 | 7 | 8 | 9 | 10 | Average |
|---|---|---|---|---|---|---|---|---|---|---|---|
| 10 | 131.13 | 131.24 | 129.60 | 129.18 | 131.35 | 132.44 | 130.61 | 129.23 | 129.31 | 131.35 | 130.54 |
| 25 | 129.73 | 133.99 | 132.65 | 130.65 | 131.96 | 129.49 | 132.61 | 133.58 | 130.71 | 132.29 | 131.77 |
| 50 | 132.79 | 133.56 | 132.95 | 131.75 | 133.28 | 131.98 | 133.88 | 134.37 | 131.56 | 133.00 | 132.91 |
| 100 | 132.59 | 133.95 | 135.09 | 135.86 | 136.71 | 134.39 | 132.52 | 134.45 | 136.87 | 135.76 | 134.82 |
| 150 | 137.39 | 136.74 | 134.93 | 134.70 | 135.00 | 134.04 | 136.69 | 134.98 | 137.88 | 135.05 | 135.74 |

**Table E3.** ImageJ values of $t_{bg} = 240\mu m$ trials.

| $V_r$ | 1 | 2 | 3 | 4 | 5 | 6 | 7 | 8 | 9 | 10 | Average |
|---|---|---|---|---|---|---|---|---|---|---|---|
| 10 | 126.37 | 128.76 | 129.25 | 127.24 | 131.06 | 127.02 | 127.14 | 128.62 | 131.15 | 128.37 | 128.50 |
| 25 | 128.14 | 127.70 | 127.72 | 128.76 | 131.91 | 132.67 | 133.56 | 128.73 | 126.27 | 131.04 | 129.65 |
| 50 | 127.77 | 132.32 | 132.95 | 131.04 | 133.36 | 135.59 | 132.56 | 126.77 | 127.11 | 132.25 | 131.17 |
| 100 | 132.21 | 133.38 | 130.61 | 134.32 | 132.58 | 135.45 | 131.39 | 129.15 | 134.23 | 134.58 | 132.79 |
| 150 | 131.84 | 133.32 | 135.44 | 132.64 | 134.92 | 131.60 | 136.35 | 135.88 | 136.28 | 133.38 | 134.16 |

**Table E4.** ImageJ values of $t_{bg} = 320\mu m$ trials.

| $V_r$ | 1 | 2 | 3 | 4 | 5 | 6 | 7 | 8 | 9 | 10 | Average |
|---|---|---|---|---|---|---|---|---|---|---|---|
| 10 | 126.37 | 128.76 | 129.25 | 127.24 | 131.06 | 127.02 | 126.14 | 128.62 | 131.15 | 128.37 | 128.40 |
| 25 | 128.14 | 127.70 | 127.72 | 128.76 | 131.91 | 132.67 | 133.56 | 128.73 | 126.27 | 131.04 | 129.65 |
| 50 | 127.77 | 132.32 | 132.95 | 131.04 | 133.36 | 135.59 | 132.56 | 126.77 | 127.11 | 132.25 | 131.17 |
| 100 | 132.21 | 133.38 | 130.61 | 134.32 | 132.58 | 135.45 | 131.39 | 129.15 | 134.23 | 134.58 | 132.79 |
| 150 | 131.84 | 133.32 | 135.44 | 132.64 | 134.92 | 131.60 | 136.35 | 135.88 | 136.28 | 133.38 | 134.16 |

Appendix F: Linear Regression Analysis Values

**Table F1.** Packing density linear regression analysis values.

| Packing Density | Blade Gap Thickness (µm) | Recoater Velocity (mm/s) |
|---|---|---|
| 55.65% | 80 | 10 |
| 53.46% | 80 | 25 |
| 51.14% | 80 | 50 |
| 49.89% | 80 | 100 |
| 49.51% | 80 | 150 |
| 57.36% | 160 | 10 |
| 56.91% | 160 | 25 |
| 56.35% | 160 | 50 |
| 55.74% | 160 | 100 |
| 55.30% | 160 | 150 |
| 60.75% | 240 | 10 |
| 59.82% | 240 | 25 |
| 59.25% | 240 | 50 |
| 58.53% | 240 | 100 |
| 58.40% | 240 | 150 |
| 60.81% | 320 | 10 |
| 58.97% | 320 | 25 |
| 57.02% | 320 | 50 |
| 56.12% | 320 | 100 |
| 55.70% | 320 | 150 |

**Table F2.** Surface roughness linear regression analysis values.

| Surface Roughness | Blade Gap Thickness (µm) | Recoater Velocity (mm/s) |
| --- | --- | --- |
| 52.05% | 80 | 10 |
| 52.61% | 80 | 25 |
| 53.16% | 80 | 50 |
| 53.80% | 80 | 100 |
| 54.13% | 80 | 150 |
| 51.19% | 160 | 10 |
| 51.67% | 160 | 25 |
| 52.12% | 160 | 50 |
| 52.87% | 160 | 100 |
| 53.23% | 160 | 150 |
| 50.35% | 240 | 10 |
| 50.84% | 240 | 25 |
| 51.44% | 240 | 50 |
| 52.07% | 240 | 100 |
| 52.61% | 240 | 150 |
| 50.35% | 320 | 10 |
| 51.03% | 320 | 25 |
| 51.86% | 320 | 50 |
| 52.68% | 320 | 100 |
| 53.08% | 320 | 150 |

**Table F3.** PD/SR ratio linear regression analysis values.

| PD/SR Ratio | Blade Gap Thickness (μm) | Recoater Velocity (mm/s) |
|---|---|---|
| 1.07 | 80 | 10 |
| 1.02 | 80 | 25 |
| 0.96 | 80 | 50 |
| 0.93 | 80 | 100 |
| 0.91 | 80 | 150 |
| 1.12 | 160 | 10 |
| 1.10 | 160 | 25 |
| 1.08 | 160 | 50 |
| 1.05 | 160 | 100 |
| 1.04 | 160 | 150 |
| 1.21 | 240 | 10 |
| 1.18 | 240 | 25 |
| 1.15 | 240 | 50 |
| 1.12 | 240 | 100 |
| 1.11 | 240 | 150 |
| 1.21 | 320 | 10 |
| 1.16 | 320 | 25 |
| 1.10 | 320 | 50 |
| 1.07 | 320 | 100 |
| 1.05 | 320 | 150 |